POLITECNICO DI MILANO
DEPARTMENT OF ELECTRONICS INFORMATION AND BIOENGINEERING
DOCTORAL PROGRAMME IN INFORMATION TECHNOLOGY

ACOUSTIC PIPELINE MONITORING: THEORY AND TECHNOLOGY

Doctoral Dissertation of:
Silvio Del Giudice

Supervisor:
Prof. Giancarlo Bernasconi
Assistant Supervisor:
Dr. Giuseppe Giunta

Tutor:
Prof. Andrea Monti Guarnieri

The Chair of the Doctoral Program:
Prof. Carlo Fiorini

Year 2014– Cycle XXVI

A mia madre Gabriella

Acknowledgements

Since all the content and the results of this thesis have grown within research projects promoted and supported by eni spa, I certainly wish to thank the company and in particular Dr. Giuseppe Giunta, the project manager of Dionisio research project.
I wish to thank also Aresys s.r.l. which contributed to the project with the software production and Solgeo s.r.l. with instrumentation and services.
I also thank Dr. Diego Rovetta who introduced me to the Matrix Method.

Abstract

This thesis deals with monitoring of pipelines through acoustic measurements. Acoustic monitoring is a technique that exploits the fact that any disturbance occurring in the pipe infrastructure or in the conveyed fluid produces or influences acoustic transients which propagate as waves within the fluid at distances of many kilometers, carrying information on the originating event and on the propagation channel.

I first analyze the theory of elastic wave propagation in pipelines and present a suitable matrix method to compute propagation parameters in fluid-filled pipelines possibly buried or submerged, taking into account several propagation effects among which fluid thermo-viscosity, pipe elasticity, external load and radiation.

The propagation parameters can be found at any frequency and for any axisymmetric propagation mode.

The theoretical study was functional to the design and development of a registered technology (e-vpms®) for pipeline monitoring which I contributed to.

This system in fact employs a discrete network of vibro-acoustic monitoring stations mounted along gas or liquid pipelines which measure synchronized physical signals.

Thanks to measurements performed on a buried in-service oil pipeline, I have experimentally validated the propagation method presented in the whole range of frequency of interest.

Propagation parameters of acoustic waves were also measured in many in-service gas pipelines and found in agreement with theory.

An important application of the monitoring system is the leak detection system that was tuned and validated on an in–service oil pipeline.

In gas pipelines instead I describe some methods of pig (pipeline inspection gauge) tracking and a successful application of acoustic reflectometry on a pipeline to find and characterize anomalous pipe sections.

Moreover I propose, through real examples, further advanced processing to measured and stored data such as the long term monitoring which allows to identify the standard operational conditions in a pipeline and therefore detect possible anomalous situations.

A last type of application concerns the use of theoretical models of wave propagation and of fluid properties to interpret the measurements and obtain further information on the conveyed fluid and the flow regime.

Sommario

Questa tesi riguarda il monitoraggio di linee di trasporto per mezzo di misure acustiche. Il monitoraggio acustico è una tecnica che sfrutta il fatto che qualsiasi disturbo che si verifica nell'infrastruttura di trasporto o nel fluido trasportato produce o influenza transienti acustici che si propagano come onde nel fluido a distanze anche di molti chilometri, traportando informazioni sull'evento originario e sul canale di propagazione.
Inizialmente analizzo la teoria della propagazione di onde elastiche e presento un metodo matriciale apposito, per calcolare i parametri di propagazione in condotte contenenti fluidi eventualmente sommerse o interrate, prendendo in considerazione diversi effetti di propagazione tra i quali termo-viscosità dei fluidi, elasticità del tubo, carico e radiazione esterni.
E' possibile poi ottenere i parametri di propagazione a qualsiasi frequenza e per qualsiasi modo di propagazione assi-simmetrico.
Lo studio teorico è stato propedeutico alla progettazione e sviluppo di una tecnologia registrata (e-vpms®) per il monitoraggio di linee di trasporto a cui ho contribuito.
Questo sistema infatti impiega una rete discreta di stazioni di monitoraggio montate su linee per gas o liquidi che misurano segnali fisici sincronizzati.
Grazie alle misure eseguite su una linea ad olio interrata e in funzione, ho validato sperimentalmente il metodo di propagazione presentato nell'intero intervallo di frequenze di interesse.
I parametri di propagazione delle onde acustiche sono stati misurati anche su diverse linee a gas in servizio e risultati in accordo con la teoria.
Un'importante applicazione del sistema di monitoraggio è il sistema di rilevazione di fuoriuscite che è stato messo a punto e validato su una linea ad olio in funzione.
Per linee a gas invece descrivo alcuni metodi di tracciamento di PIG (sonde di ispezione per linee di trasporto) e un'applicazione di successo di riflettometria acustica su una condotta per trovare e caratterizzare sezioni di tubo anomale.
Propongo inoltre, attraverso esempi concreti, ulteriori elaborazioni avanzate di dati misurati e immagazzinati come il monitoraggio a lungo termine che permette di identificare le condizioni operative standard di una condotta e dunque rilevare eventuali situazioni anomale.
Un ultimo tipo di applicazione prevede l'uso di modelli teorici di propagazione delle onde e delle proprietà dei fluidi per interpretare le misure e ottenere ulteriori informazioni sul fluido trasportato e il regime di flusso.

Contents

List of figures

List of tables

List of symbols

Latins

a	External pipe radius
$A_{1,2}$	unknown coefficients for P-waves in the pipe shell
b	Internal pipe radius
B	Bulk modulus
$B_{1,2}$	unknown coefficients for S-waves in the pipe shell
c	Acoustic wave speed
$C_{1,2}$	unknown coefficients for P-wave and S-wave in the internal layer
$D_{1,2}$	unknown coefficients for P-wave and S-wave in the external layer
E	Elastic modulus
h	Pipe wall thickness
$H_y^{(x)}$	Hankel function of x^{th} type, of order y
j	Imaginary unit
J_y	Bessel function of 1st type, of order y
k	Wavenumber
L	Solution matrix for modal wavenumber
M_{rad}	Radiation mass
P	Pressure
Pr	Prandtl number
R_{rad}	Radiation resistance
r	Pipe radial coordinate
t	time
T	Temperature
Y_y	Bessel function of 2nd type, of order y
z	Impedance Pipe axis coordinate

Greeks

α	Attenuation (per unit length) Pressure waves radial wavenumber
β	Shear waves radial wavenumber
γ	Ratio of specific heats
ε	Linear strain Wavespeed correction factor
ζ	Dynamic second (or bulk) viscosity
η	Dynamic shear viscosity

θ	Pipe azimuthal coordinate
λ	First Lamé parameter
μ	Second Lamé parameter
ν	Poisson ratio
ξ	Modal wavenumber
ρ	Density
τ	Stress
χ	Pipe loss factor
ω	Angular frequency

Subscripts

$_f$	free-medium
	fluid
$_n$	Mode number
$_m$	External medium
$_p$	Pipe
	Pressure wave
$_{ph}$	Phase
$_s$	Shear wave

Superscripts

^{E}	External layer
^{I}	Internal layer
^{r}	Radial
^{S}	Shell (layer)

Framework and rationale

Nowadays pipelines are a widespread, efficient and cheap mean of transportation for many fluids, in particular hydrocarbons.
Possible failures or damages to such structures might cause serious economic, environmental and health consequences, that's why it's of paramount importance to monitor the working condition of pipelines.
In particular as regards to oil and gas pipelines, in many country the law compels fairly to install systems that detect leaks of a certain amount within a certain delay.
Since conduits are often buried or laid on the sea-bottom it's difficult to perform direct monitoring and there arose the need to think out techniques of indirect monitoring, often called non-invasive or non-destructive. Among these I can cite mass balance, Computational Pipeline Monitoring (CPM), even satellite surveillance.
The technique dealt with in this thesis is acoustic monitoring which exploits the fact that many events to be monitored in the pipeline produce or influence acoustic transients and these propagate as waves within the transported fluid at distances of many kilometers, carrying information on the originating event and on the propagation channel.
During my PhD I contributed to the development of a vibro-acoustic monitoring system (e-vpms® registered technology) which employs sensors to measure acoustic and other signals to monitor pipelines.
The design and development of this technology have required the study of the theory of wave propagation in pipelines.
In the case of gas-filled pipelines, the pipe can usually be considered a rigid medium and the simple wide-tube approximation which describes the fluid-borne wave propagation (Blackstock [1]) is sufficient for most practical application, as claimed by Stecki & Davis [2]; in the case of liquids, the compressibility of the fluid is comparable to the compressibility of the pipe material and therefore the properties of the shell are important and possibly even the properties of the external medium.
To this end, an interesting model is proposed by Pinnington and Briscoe [3] and extended by Muggleton [4], which accounts for pipe elasticity, and surrounding solid medium effects, but neglects fluid viscosity. In particular these authors show the large contribution to wave attenuation due to the outward radiation of both pressure and shear waves. The advantage of these models is their analytic form but their validity falls in proximity of the ring frequency.
In fact, in order to obtain solutions for all frequencies and all propagation modes, a more complex matrix method is needed, which was well described in Gazis [5].
More recently the matrix method was employed among others by Rama Rao and Vandiver [6] for propagation in boreholes, Sinha et al. [7] and Plona at al. [8] for fluid loaded pipes filled with inviscid fluid.
This approach has been generalized to any sequence of cylindrical elastic layers as the Global Matrix Method (Lowe [9]) and implemented in the Disperse software by Imperial College (Pavlakovic [10]); fluid layers are then treated as equivalent elastic

solid layers introducing the fluid viscosity by means of a fictitious shear wave (Aristegui et al. [11], Long et al. [12], Vogt at al. [13], Ma et al. [14]).
Elvira-Segura [15] also used a matrix method to couple an internal viscous fluid with an external solid layer surrounded by vacuum, this model was recently used and extended to viscous shells by Baik [16].
In Chapter 3 of this thesis, the formulation of Sinha et al. [7], which in turn borrows the formulation of Gazis [5], is used to model 3 cylindrical layers, where the core medium, is implemented as a solid but turned into thermo-viscous fluid by proper re-definition of Lamé parameters similarly to the Disperse software and Baik [16].
The method described, in general, allows to consider a waveguide made of 3 co-axial cylindrical layers each of which can be either solid or fluid. In case of solid it has an elastic behavior, described by elastic parameters such as Lamé's, which could be even complex, like in [16]. In case of fluid medium, both thermal and viscous effects are considered, and for each of them, both the following types: bulk and boundary layer.
The switching from solid to fluid is easily performed by replacing Lamé parameters with proper functions of fluid's viscous and thermal parameters.
In this way a unique model can be used for both gas- and liquid-filled pipelines, which can support technologies such as e-vpms®, for monitoring of pipelines in different ways like for example real-time remote detection of third-party interference or long-term monitoring of transportation efficiency or detection of malfunctioning, failures and anomalies along pipeline.

Part I: Theory of acoustic propagation in pipelines

Introduction

I analyze here the theory of acoustic wave propagation as far as it is useful to describe propagation of waves that can be exploited for pipeline monitoring, considering both liquid and gas as filling fluids.
In the first chapter I qualitatively describe the wave propagation in pipes with particular care to the different phenomena of absorption and dispersion, mathematically modeled as propagation parameters, that take place in different scenarios of pipelines.
In Chapter 2 I report a selection of propagation models according to the phenomena they take into account, most of the models were selected for their relative simplicity, being analytic or semi-analytic. For each model the computation method is presented.
Then I choose a common scenario of particular interest to hydrocarbon transportation, that is a buried oil-filled pipeline, in order to compute and compare the results of the models presented.
The comparison shows that none of the methods presented can accurately compute the propagation parameters in the whole range of frequency of practical interest, at least from unit Hz up to hundred Hz, but a more general matrix method is needed.
This general matrix method is called AXSYM-3L and is described in Chapter 3, it simulates a waveguide of 3 cylindrical layers where each layer can be set to solid or fluid; fluids are thermo-viscous.
In Chapter 4 I show some of the results of the model, limited to fluid-filled pipes, buried or submerged and to the fundamental fluid-borne propagation mode.
In particular I perform some tests to verify the effect of the surrounding media, and others to verify the effect of the thermal boundary layer.
Results of AXSYM-3L are shown in the scenario of Chapter 2 together with the other models, and AXSYM-3L looks suited to provide accurate results in a wider frequency range than other models.
Finally AXSYM-3L as a matrix method is used to compute and display also the profiles of field variables and these will be shown in physical units for the usual scenario at the typical frequency of 50 Hz.

1. Acoustic propagation in pipelines

Acoustic wave propagation in fluid filled pipes can be conveniently described by the dispersion curve, i.e. the dependence of the wave phase velocity on frequency and by the attenuation curve, i.e. the decay of the signal amplitude with propagation distance.
Dispersion and attenuation are complicated phenomena associated with

1. Fluid bulk viscosity and thermal conduction.
2. Fluid viscous and thermal interaction with the pipe wall.
3. Fluid relaxation.
4. Pipe visco-elasticity.
5. Pipe external load and radiation.

I give here a brief description and explanation of each of these effects.

1.1. Fluid bulk viscosity and thermal conduction

Bulk viscosity and bulk thermal conduction affect the propagation of any wave travelling in a fluid, both in guided propagation (e.g. within a pipe) and in free propagation.
The viscosity of the fluid resists to motion because of friction among fluid particles: this causes attenuation, because mechanical energy is converted to heat, and also velocity dispersion.
On the other side, during wave propagation, the particles of the medium are continuously compressed and expanded. Compressed particles get warmer than the expanded ones, and this temperature gradient gives rise to a heat flux from the hotter regions to the colder ones (Figure 1.1). The energy associated to the thermal flux is subtracted from the propagating wave energy, determining attenuation.

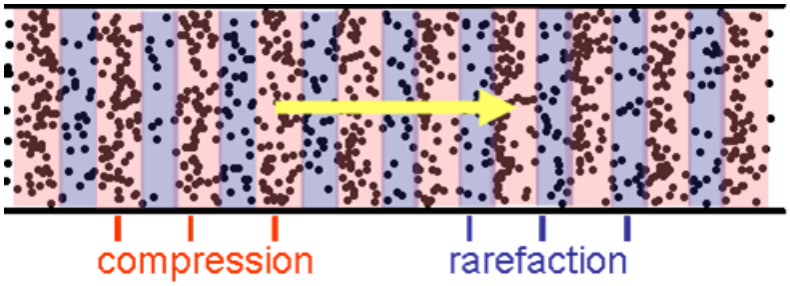

Figure 1.1. Compression and rarefaction due to a travelling wave

1.2. Fluid viscous and thermal interaction with the pipe wall

The pipe wall affects pressure wave propagation mainly in two ways: it causes additional shear stresses, and it exchanges heat with the fluid.
As regards to the first effect, the fluid particles adjacent to the pipe wall must be at rest (no-slip condition), whereas those near the pipe axis can move freely (Figure 1.2). A complex velocity profile establishes along the section: axial viscous shear stresses act on the fluid, determining absorption and dispersion.
Regarding the thermal effect, the pipe behaves as an infinite heat source at constant temperature. The motion close to the wall is isothermal, whereas the motion near the pipe axis is not isothermal. This produces again a complex temperature profile along the pipe section, a heat flux between particles, and therefore absorption and dispersion of the wave.

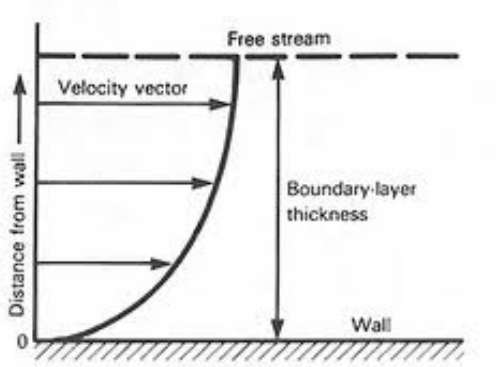

Figure 1.2. Velocity profile along inner radius

1.3. Fluid relaxation

Relaxation occurs in a chemically reactive fluid made up of more than one substance, or in a fluid made up of molecules whose internal energy is associated to different modes of molecules motion (translational, rotational and vibrational). When the equilibrium is modified by the passage of the wave, the different modes require different time periods to reset to the equilibrium values.
This circumstance produces wave attenuation.

1.4. Pipe visco-elasticity

If the pipe is not perfectly rigid, it tends to follow the disturbance propagating in the fluid by expanding and compressing. For a perfectly elastic pipe (including any external medium), no energy dissipation takes place, that is no wave absorption, but the wave velocity is reduced and dispersed.
On the other side, if the pipe is viscous, also absorption occurs, due to dissipation of energy during pipe deformation.

1.5. Pipe external load and radiation

If the pipe is surrounded by a medium different from vacuum, the properties of this medium can affect the wave traveling in the fluid (Figure 1.3).
First, in the same way as the pipe elasticity can reduce the wave-speed, the external medium contributes by changing the elasticity of the whole "waveguide system".
Second, the contact between the pipe and the external medium, which is assumed of infinite extent, allows the leakage of energy outwards, producing wave attenuation.

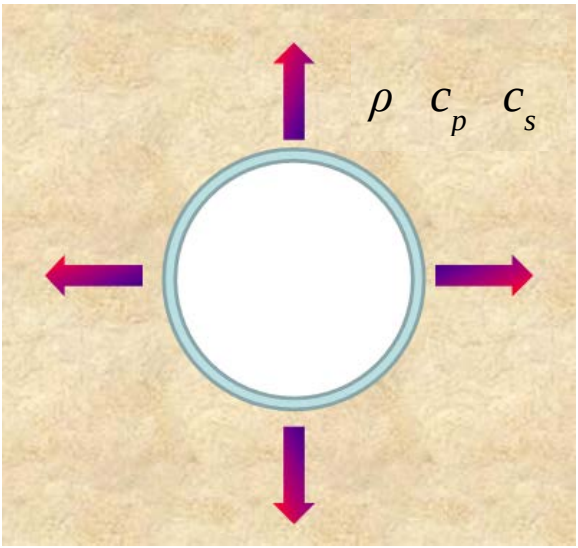

Figure 1.3. Pipe external load and radiation.

1.6. Discussion

For points 1 and 2, thermal and viscous effects are of the same order of magnitude only for gases, whereas in liquids thermal effects are negligible.
The bulk viscosity and bulk thermal effects are important only at ultrasonic frequencies or for very wide tubes, otherwise they are small compared to those due to the interaction with the pipe walls.
Relaxation can be important, for instance, in air and in sea water, but it is practically absent in fresh water. In air, the effect on absorption can be higher than the bulk thermo-viscous effects, but of the same order of magnitude, so that also relaxation is usually neglected in fluid-filled pipelines.
The pipe can be considered perfectly rigid when its Young modulus is much greater than the fluid bulk modulus, and/or when the pipe thickness is far greater than the radius: this is usually valid for gases, not for liquids.

The pipe viscous effect can be neglected for elastic materials, typically metals, while it is not negligible for other materials such as plastics, which are strongly viscoelastic.
Finally, the effect of the external medium is important only if it has a density comparable with the pipe's density, and the pipe itself is not perfectly rigid. Therefore it becomes negligible when the external medium is gas, but it has to be considered for liquid filled elastic pipe surrounded by liquids or solids.

2. Literature review

Here I report the description of a selection of propagation models in fluid filled cylindrical pipelines. This review is not intended as an exhaustive state of the art, instead a set of representative models was chosen according to their scope and propagation effects accounted for with the purpose of analyzing separately the phenomena described in the previous section. The models will be presented approximately in increasing order of complexity and accuracy and their results will be shown and compared in a common scenario.

2.1. Literature models description

2.1.1. Model 1: water hammer

Reference: Liu [17] (pages 66-67)
Framework

This model considers the celerity (speed) of water-hammer pressure waves in pipelines, from a hydraulic point of view. The water hammer generated by a sudden valve closure produces a high pressure variation and a significant expansion of the pipe wall, resulting in a reduction of wavespeed.
Assumptions

- (Implicitly) Axisymmetric wave motion.
- Low frequency, no dispersion nor attenuation is considered.
- Inviscid fluid.

Computation procedure

The pressure wave speed c in the internal fluid is provided as a function of the free medium wavespeed $c_f = \sqrt{B_f / \rho_f}$ and the physical and geometric parameters of the fluid and the pipe.

$$c = \frac{\sqrt{B_f / \rho_f}}{\sqrt{1 + (B_f / E)(2b/h)\varepsilon}} \tag{2.1}$$

B_f : fluid bulk modulus

ρ_f : fluid density

E : pipe Young modulus

b : internal pipe radius

h : pipe thickness

ε is a dimensionless factor equal to 1.0 when the pipe wall is thin (i.e., when $2b/h>25$) while for thick-walled pipes ($2b/h<25$), the factor ε differs for different conditions, as follows:

Case 1. Pipeline anchored upstream

$$\varepsilon = \frac{h}{b}(1+\nu) + \frac{2b}{2b+h}\left(1-\frac{\nu}{2}\right) \tag{2.2}$$

Case 2. Pipeline anchored against longitudinal movement

$$\varepsilon = \frac{h}{b}(1+\nu) + \frac{2b}{2b+h}\left(1-\frac{\nu^2}{2}\right) \tag{2.3}$$

Case 3. Pipeline with expansion joints throughout its length

$$\varepsilon = \frac{h}{b}(1+\nu) + \frac{2b}{2b+h} \tag{2.4}$$

where ν is the Poisson ratio of the pipe shell.
Notice that c is always less than c_f, so the elasticity of the pipe walls has the effect of reducing the wave speed.

2.1.2. Model 2: wide tube approximation

Reference: Blackstock [1] (pages 322-325) reporting results originally due to Kirchhoff.

Framework

The model considers propagation of pressure waves in viscous fluids within rigid pipes. The model is applicable when the pipe rigidity is much higher than the fluid rigidity, like gases in metallic pipes.

Assumptions

- Axisymmetric wave motion.
- Rigid pipe (also elastic with suited addition).
- Small amplitude pressure waves.
- Absorption is related only to interaction with the wall pipe, and it takes place in a narrow (with respect to the pipe radius) boundary layer. This condition is expressed as a double inequality for frequency, i.e. the model is valid for a limited frequency range (see [1] and [18])

Computation procedure

The absorption coefficient α and the phase velocity c_{ph} are provided as functions of the angular frequency ω, the pipe radius b, and the fluid physical properties (density ρ_f, speed of sound c_f, dynamic viscosity η, specific heats ratio γ and Prandtl number Pr).

$$\alpha = \frac{1}{b}\sqrt{\frac{\omega\eta}{2\rho_f c_f^2}}\left(1+\frac{\gamma-1}{\sqrt{\Pr}}\right) \tag{2.5}$$

$$c_{ph} = \frac{c_f}{1+\alpha c_f/\omega} = \frac{c_f}{1+\frac{1}{b}\sqrt{\frac{\eta}{2\rho_f\omega}}\left(1+\frac{\gamma-1}{\sqrt{\Pr}}\right)} \tag{2.6}$$

The absorption coefficient is proportional to the square root of frequency and to the inverse of the radius.
The phase velocity increases from 0 (at frequency 0) up to the free medium velocity (for infinite frequency).
The case of elastic pipe can be approximately considered by correcting, in both previous formulas, the free fluid velocity c_f, with the water hammer formula (2.1) (this is claimed by Stecki & Davis [2]).

2.1.3. Model 3: viscous incompressible fluid in elastic pipe

Reference: Morgan & Kiely [19].
Framework

The model focuses on propagation of pressure waves through liquid-filled flexible tubes. The fluid is considered viscous but incompressible, phase velocity and damping factor are functions of the viscosity of the liquid and of the internal damping in the tube wall.
Assumptions

- Thin walls.
- Small amplitude pressure waves.
- Pressure wavelength far greater than pipe radius.
- Speed of pressure wave in the fluid far less than compressional speed in pipe shell.
- Axisymmetric wave motion.
- Incompressible viscous fluid.

Computation procedure

The authors provide two different approximate solutions depending on the value of the parameter $b\sqrt{\frac{\omega\rho_f}{\eta}}$

where
ρ_f: fluid density
η: fluid dynamic viscosity
b: pipe radius

Case 1. Small viscosity: $b\sqrt{\frac{\omega\rho_f}{\eta}} >> 1$

$$c_{ph} = \sqrt{\frac{Eh}{2\rho_f b}}\left[1-\left(1-\nu+\frac{\nu^2}{4}\right)\frac{1}{b}\sqrt{\frac{\eta}{2\rho_f\omega}}\right]$$
$$\alpha = \omega\sqrt{\frac{2\rho_f b}{Eh}}\left[\frac{1}{b}\sqrt{\frac{\eta}{2\rho_f\omega}}\left(1-\nu+\frac{\nu^2}{4}\right)+\frac{\omega E'}{2E}\right] \quad (2.7)$$

Case 2. Large viscosity: $b\sqrt{\frac{\omega\rho_f}{\eta}} << 1$

$$c_{ph} = \sqrt{\frac{Eh}{2\rho_f b}}b\sqrt{\frac{\rho_f\omega}{\eta}}\frac{1}{\sqrt{5-4\nu}}\left(1+\frac{\omega E'}{2E}+\frac{2\omega\nu'}{5-4\nu}\right)$$
$$\alpha = \omega\sqrt{\frac{2\rho_f b}{Eh}}\frac{1}{b}\sqrt{\frac{\eta}{\rho_f\omega}}\sqrt{5-4\nu}\left(1+\frac{\omega E'}{2E}+\frac{2\omega\nu'}{5-4\nu}\right) \quad (2.8)$$

ν : Poisson ratio.
h: pipe thickness
E' and ν' appear in case of pipe viscosity, that is when the elastic constants E^* and ν^* are complex because the stresses depend also on the strain rates. The following relations hold:

$$E^* = E - j\omega E'$$
$$\nu^* = \nu - j\omega\nu' \quad (2.9)$$

This model of pipe viscosity (Kelvin-Voigt) is actually not used for metals, therefore no values of E' or ν' are available for steel.
Please note that, by neglecting the pipe internal damping (or at low frequency), in both cases, the absorption coefficient has the same dependence on frequency as Model 2 (Blackstock [1]), while, for increasing ω, α gets a quadratic dependence on frequency.
Moreover, in the small viscosity solution, the phase velocity, not affected by internal damping, has a similar dependence on frequency as Model 2.

2.1.4. Model 4: inviscid fluid in elastic pipe surrounded by vacuum

Reference: Pinnington & Briscoe [3]

Framework

The model considers the wave motion in a fluid-filled pipe in order to compare the analytical solution with measurements recorded on the pipe shell and in the fluid. Attenuation and dispersion curves are provided for the two axisymmetric wave modes associated with the longitudinal shell motion and the internal pressure wave. Here only the latter is reported.

Assumptions

- Frequency far less than ring frequency
- Inviscid fluid
- Thin wall shell, pipe thickness far less than pipe radius
- Fluid wavespeed far less than shell compressional wavespeed
- Axisymmetric wave motion
- Pipe in vacuum

Computation procedure

The propagation characteristic is defined through the wavenumber $k_1 = \omega / c_{ph} - i\alpha$ as a function of the free medium wavenumber $k_f = \omega / c_f$.

$$k_1^2 = k_f^2 \left(1 + \frac{2B_f / b}{Eh / b^2 - \omega^2 \rho_p h} \right) \tag{2.10}$$

ρ_p: pipe density.

Since the wavenumber is real, no attenuation is accounted for, whereas the phase velocity coincides with Model 1, for low frequency (exactly at $\omega = 0$), then it slowly decreases.

2.1.5. Model 5: inviscid fluid in elastic, buried pipe

Reference: Muggleton et al. [4].

Framework

Authors consider the wave motion in a fluid-filled pipe, surrounded by an infinite elastic medium which can support both longitudinal and shear waves. The attenuation and dispersion curves are derived for two wave types (*n=1,2*), which correspond to a fluid dominated wave, and an axial shell wave. Here only the former is reported.

Assumptions

- Frequency far less than ring frequency
- Inviscid fluid
- Thin wall shell, pipe thickness far less than pipe radius
- Fluid wavespeed far less than shell compressional wavespeed
- Axisymmetric wave motion

Computation procedure

The propagation characteristic is defined through the wavenumber $k_1 = \omega / c_{ph} - j\alpha$ as a function of the free medium wavenumber $k_f = \omega / c_f$.

$$k_1^2 = k_f^2 \left(1 + \frac{2B_f / b}{Eh/b^2 - \omega^2(\rho_p h + M_{rad}) + j(\omega R_{rad} + \chi Eh/b^2)} \right)$$
$$k_f = \frac{\omega}{c_f} \tag{2.11}$$

With respect to the previous model 4, two additional phenomena are accounted for: the effect of the surrounding medium, and the internal pipe absorption. They appear in the wavenumber equation as three new terms

χ : the loss factor

M_{rad} : radiation mass

R_{rad} : radiation resistance

with

$$R_{rad} = \mathrm{Re}(z_{pn} + z_{sn})$$
$$M_{rad} = \mathrm{Im}(z_{pn} + z_{sn}) / \omega \tag{2.12}$$

z_{pn} and z_{sn} are the impedances of the longitudinal and shear waves in the external medium, for the two modes *n=1,2*. Here I deal just with *n=1* (fluid-borne wave). Impedances are functions of the surrounding medium density ρ_m, and seismic wave velocities c_p and c_s (respectively P- and S-waves)

$$z_{(p,s)n} = \frac{-j\rho_m c_{(p,s)} k_{(p,s)n}}{k^r_{(p,s)n}} \frac{H_0^{(2)}(k^r_{(p,s)n} b)}{H_0'^{(2)}(k^r_{(p,s)n} b)} \tag{2.13}$$

$H_0^{(2)}$ is the zero order Hankel function of the second kind (for outgoing waves). The prime sign denotes differentiation with respect to the argument. $k^r_{(p,s)n}$ are the radial components of the longitudinal and shear wavenumbers in the external medium, defined as

$$\left(k^r_{(p,s)n}\right)^2 = k^2_{(p,s)} - k_n^2$$

where $k_{(p,s)}$ are the longitudinal and shear wavenumbers in the external medium

$$k_{(p,s)n} = \frac{\omega}{c_{(p,s)n}}$$

Since the impedances in the external medium depend on k_1, which is the unknown solution, it must be found iteratively.

2.1.6. Model 6: viscous compressible fluid in elastic pipe

***Reference*:** Elvira-Segura [15].

Framework

The method computes the velocity and the attenuation of an acoustic wave propagating inside a cylindrical elastic tube filled with a viscous liquid by means of a matrix technique. This allows to find exact solutions for any frequency and propagation mode, through a root-finding technique.

Assumptions

- Viscous fluid
- Elastic pipe
- Pipe in vacuum
- Axisymmetric wave motion

Computation procedure

This model does not provide an analytic solution. It is a Matrix Method (MM) that has to be solved numerically.

The solutions for the complex wavenumber or complex frequency can be found by setting the determinant of the solution matrix to zero.

As a first step, the wave equations for the solid and the fluid are studied separately and the solutions for displacements as function of unknown coefficients are found. The solution matrix is built by imposing 3 boundary conditions to both pipe interfaces, resulting in a 6-by-6 matrix. For details see *Reference*.

The solution for the 1st fluid-borne mode can be found using the Wide-tube approximation as first guess and then searching in its neighborhoods.

2.2. Literature models example results

2.2.1. Scenario

I consider an oil filled steel pipeline, buried in an elastic medium. Model parameters are reported in Table 2.1.

Physical and geometrical parameters			
Symbol	Value	Unit	Description
Pipe geometry			
b	0.2	m	Pipe internal radius
h	0.0111	m	Pipe thickness
Internal fluid - Oil			
ρ_f	900	kg/m^3	Oil density

c_f	1400	m/s	Speed of sound in free medium
B_f	1.8×10^9	Pa	Bulk modulus (function of ρ_f and c_f)
η	1×10^{-2}	Pas	Dynamic viscosity
γ	1	-	Specific heats ratio
Pr	Not used	-	Prandtl number
Shell material – Steel			
ρ_p	7800	kg/m^3	Density
E	2×10^{11}	Pa	Young modulus
χ	0	-	Loss factor
E'	0	Pa	Viscous term. See Eq. (2.9)
ν	0.3	-	Poisson ratio
Surrounding medium			
ρ_m	2000	kg/m^3	Density
c_p	1500	m/s	P-wave speed
c_s	900	m/s	S-wave speed

Table 2.1. Example scenario parameters

2.2.2. Model 1: water hammer

This model predicts a reduction of speed from 1400 to about 1220 m/s.

2.2.3. Model 2: elastic wide tube

Kirchhoff's wide-tube approximation is modified to account for pipe elasticity, by correcting the free medium wave velocity with Model 1, Eq. (2.1). The resulting model will be referred to as "Elastic wide-tube". Figure 2.1 shows phase velocity and attenuation computed with Model 2.

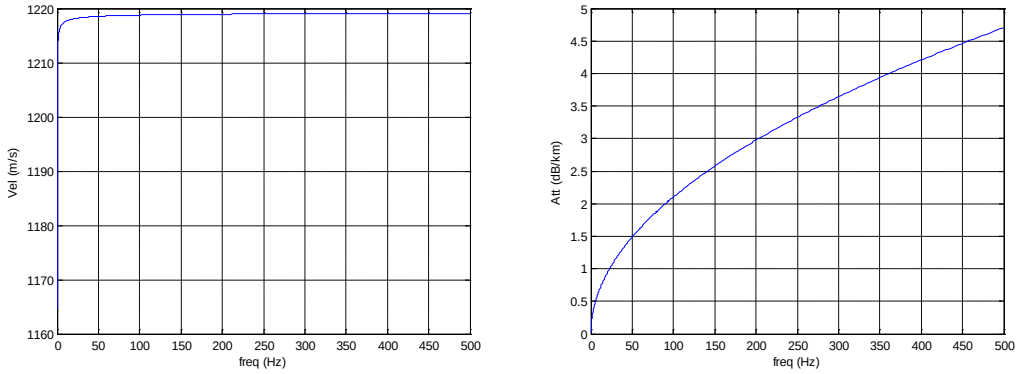

Figure 2.1. Phase velocity and attenuation computed with Model 2

2.2.4. Model 3: viscous incompressible fluid in elastic pipe

I use the solution for "Small viscosity", as it appears to be satisfied in the whole frequency range. Figure 2.2 shows phase velocity and attenuation computed with Model 3.

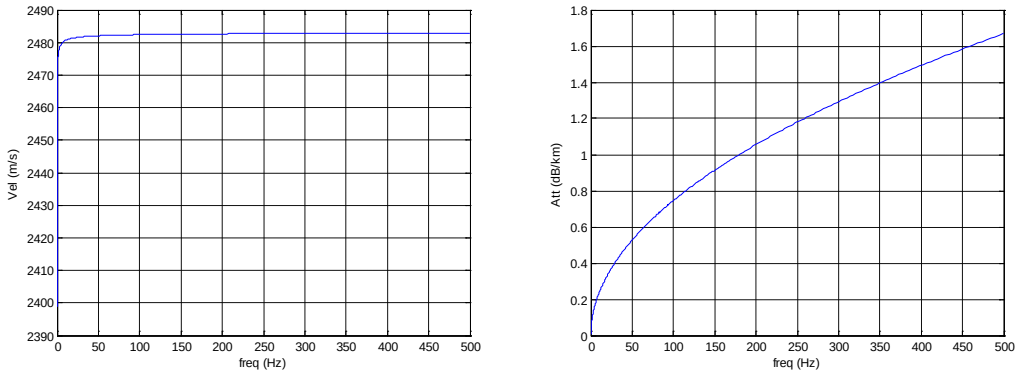

Figure 2.2. Phase velocity and attenuation computed with Model 3

2.2.5. Model 4: inviscid fluid in elastic pipe surrounded by vacuum

Figure 2.3 shows phase velocity and attenuation computed with Model 4.

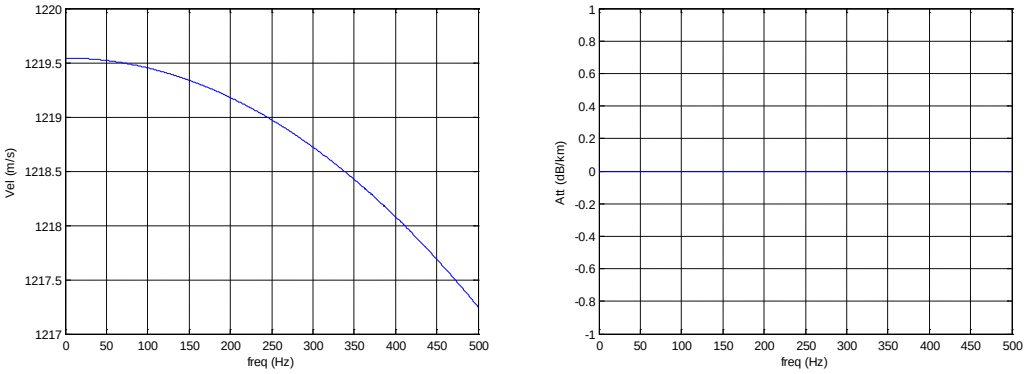

Figure 2.3. Phase velocity and attenuation computed with Model 4

2.2.6. Model 5: inviscid fluid in elastic, buried pipe

Figure 2.4 shows phase velocity and attenuation computed with Model 5.

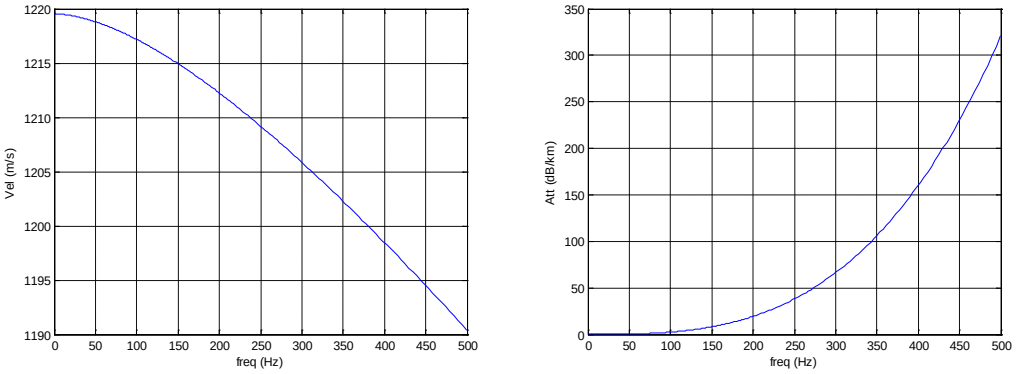

Figure 2.4. Phase velocity and attenuation computed with Model 5

2.2.7. Model 6: viscous compressible fluid in elastic pipe

Figure 2.5 shows phase velocity and attenuation computed with Model 6.

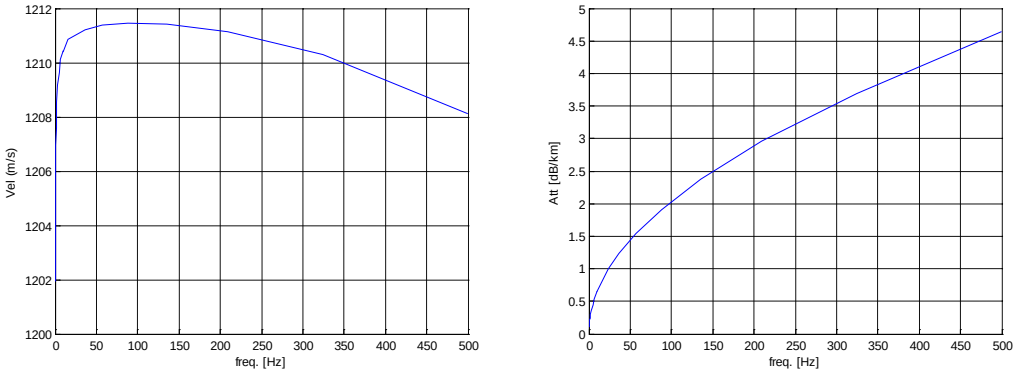

Figure 2.5. Phase velocity and attenuation computed with Model 6

2.2.8. Model comparison

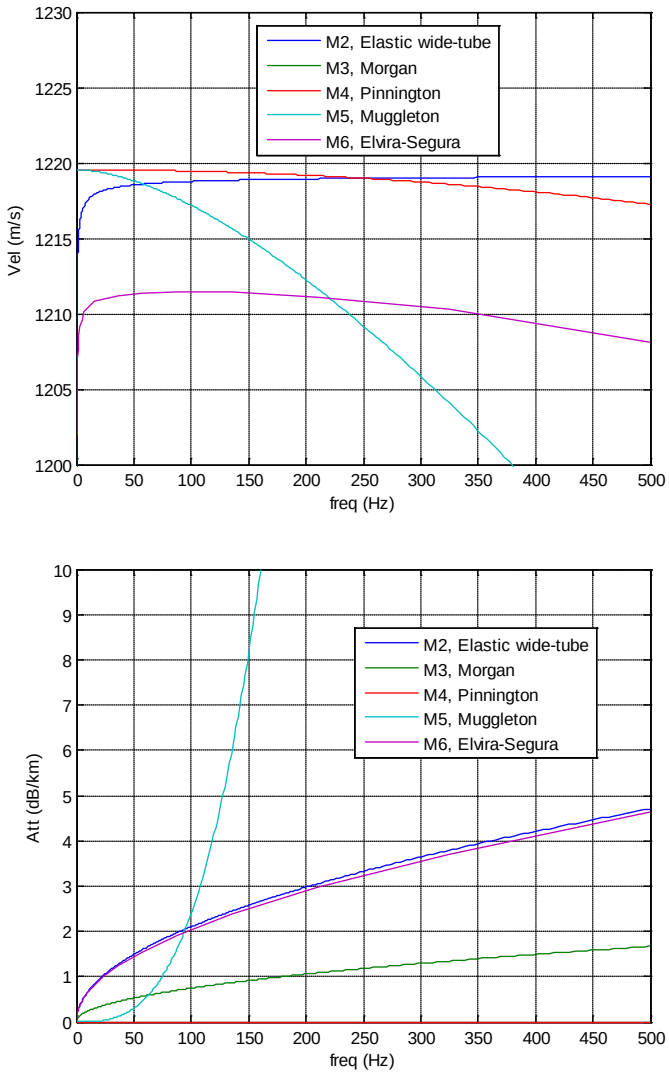

Figure 2.6. Phase velocity and attenuation computed with all models.

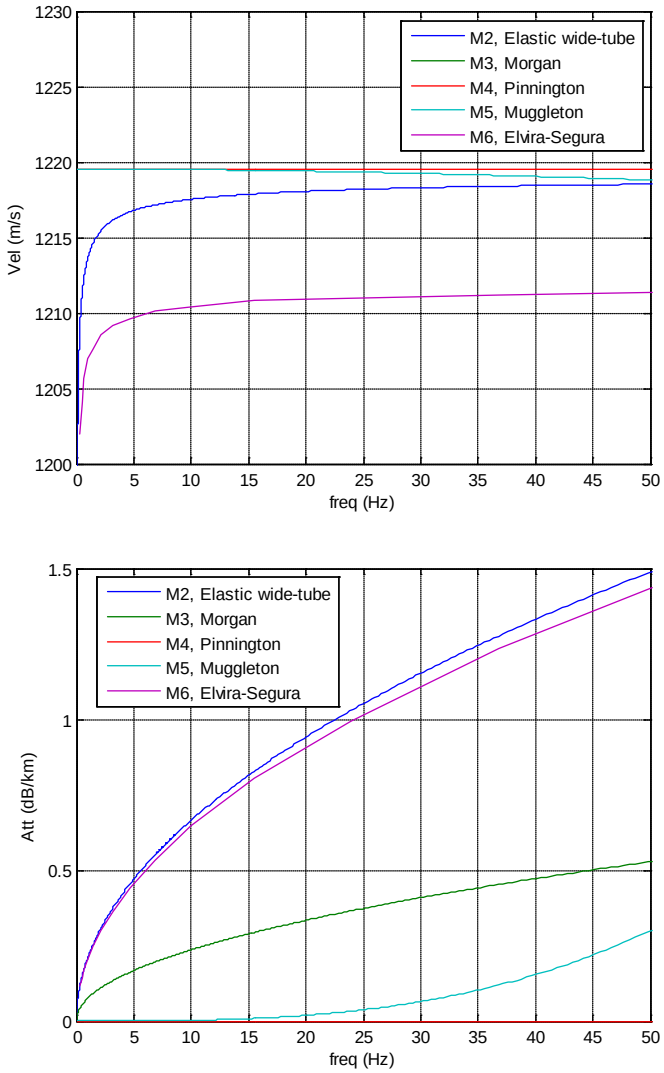

Figure 2.7: Phase velocity (top) and attenuation (bottom) computed with all models, zoom at low frequencies.

2.3. Discussion

Figure 2.6 and Figure 2.7 show different attenuation and dispersion curves for the same scenario. This can be explained by the different assumptions in the various models, summarized in Table 2.2. Model 1 doesn't appear in the table because of its simplicity, but plays a role in Model 2.

	Fluid compressibility	Fluid viscosity	Pipe elasticity	Surrounding medium
Model 2	yes	yes	yes	no
Model 3	no	yes	yes	no
Model 4	yes	no	yes	no
Model 5	yes	no	yes	yes
Model 6	yes	yes	yes	no

Table 2.2. Physical propagation phenomena considered by the models

Model 5 [4] is the only that takes into account the effect of the surrounding medium, which causes the attenuation to increase at high frequency.
Except for this phenomenon, the most general model is nr. 6 (Elvira-Segura [15]). Model 2 is similar to the latter, at least at low frequency, provided to replace the value of the free wave-speed with the velocity computed with water hammer model, Eq. (2.1), in both formulas for phase-velocity and attenuation.
At higher frequency the decreasing trend of the wave speed, due to the pipe elasticity, is the same in Model 6 and Model 4: the small scale difference should be due to the fact that Model 4 uses the water hammer approximation for null frequency, whereas model 6 should be more accurate.
Finally, since Model 3 considers the fluid to be incompressible, it clearly overestimates the velocity (which in fact falls outside the plot). This is reflected also in a lower attenuation, even if its trend resembles those of the other models at low frequency.

3. AXSYM-3L model description

None of the models described in the previous section takes into account simultaneously all the propagation phenomena that are really relevant in fluid-filled pipelines.
Another model would be “Disperse” by Imperial College, available as a commercial software, which includes all the phenomena listed in Chapter 1 except for the thermal effects which are important mainly in gas-filled pipelines. The method of Disperse is much more general than the models presented so far and therefore it is also more complicated.
Hence I have built a new model, simpler than Disperse though it can simulate also thermal effects, which for convenience is here called AXSYM-3L.
The new model is a matrix method as well and starts from the formulation (and the notation) of Sinha at al. [7], in particular it considers 3 cylindrical layers, the most external extends infinitely in the radial direction (Figure 3.1), and restricts to axisymmetric waves. These are the two reasons for the given name.

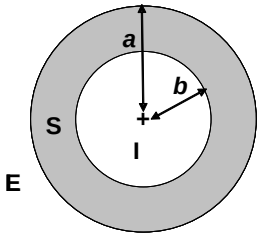

Figure 3.1. Cross-section of the waveguide constituted by 3 layers: Internal, Shell and External.

Unlike [7], all 3 layers are mathematically treated as (visco)-elastic solids and the solution is obtained, any solid layer can then be turned into a thermo-viscous fluid by redefining properly the Lamé parameters.
In the context of pipelines, the internal layer is typically a fluid, gas or liquid, the shell is always solid and the external layer might be solid, soil for instance, or fluid, water, air or even mud.
This model, as a matrix method, allows to compute the axisymmetric propagation modes of any order at any frequency, even if in this thesis only the fundamental fluid-borne mode is analyzed.
The main assumptions are:

- Longitudinally infinite and homogeneous waveguide
- Homogeneous isotropic media
- No constraints outside the pipe, except for the presence of an external medium.
- Axisymmetric propagation.

The following sections contain the complete derivation of the general model. As a first step, the mechanical wave equations are studied, and the solutions for displacements are found as a function of unknown coefficients. The solution matrix is built up by imposing four boundary conditions to both pipe interfaces, resulting in an 8-by-8 matrix. The solutions for the complex wavenumber can then be found by setting the determinant of the solution matrix to zero. This solution, which provides the propagation parameters, must be reached with numerical methods.

3.1. Wave equations

The wave equations in elastic materials can be drawn by solving a differential system where the following equations appear [7]:

- Equations of motion, Newton's second law.
- Constitutive equations (linking stress and strain).
- Strain-displacement relations.

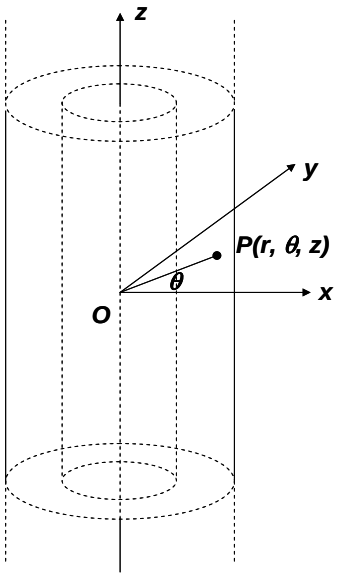

Figure 3.2. Cylindrical coordinates.

The equations of motion in cylindrical coordinates (Figure 3.2), are given by:

$$\begin{cases} \rho \dfrac{\partial^2 u_r}{\partial t^2} = \dfrac{\partial \tau_{rr}}{\partial r} + \dfrac{1}{r}\dfrac{\partial \tau_{r\theta}}{\partial \theta} + \dfrac{\partial \tau_{rz}}{\partial z} + \dfrac{\tau_{rr} - \tau_{\theta\theta}}{r} \\ \rho \dfrac{\partial^2 u_\theta}{\partial t^2} = \dfrac{1}{r}\dfrac{\partial \tau_{\theta\theta}}{\partial \theta} + \dfrac{\partial \tau_{z\theta}}{\partial z} + \dfrac{\partial \tau_{r\theta}}{\partial r} + 2\dfrac{\tau_{r\theta}}{r} \\ \rho \dfrac{\partial^2 u_z}{\partial t^2} = \dfrac{\partial \tau_{rz}}{\partial r} + \dfrac{1}{r}\dfrac{\partial \tau_{z\theta}}{\partial \theta} + \dfrac{\partial \tau_{zz}}{\partial z} + \dfrac{\tau_{rz}}{r} \end{cases} \tag{3.1}$$

where τ_{rr}, τ_{zz}, $\tau_{\theta\theta}$, $\tau_{r\theta}$, $\tau_{z\theta}$, τ_{rz} are the stress components, u_r, u_θ and u_z are the displacement components and ρ is the mass density.

For a homogeneous, elastic and isotropic medium the constitutive equations are given by:

$$\begin{aligned} \tau_{rr} &= \lambda\Delta + 2\mu\varepsilon_{rr} \\ \tau_{zz} &= \lambda\Delta + 2\mu\varepsilon_{zz} \\ \tau_{\theta\theta} &= \lambda\Delta + 2\mu\varepsilon_{\theta\theta} \\ \tau_{r\theta} &= 2\mu\varepsilon_{r\theta} \\ \tau_{z\theta} &= 2\mu\varepsilon_{z\theta} \\ \tau_{rz} &= 2\mu\varepsilon_{rz} \\ \Delta &= \frac{\partial u_r}{\partial r} + \frac{u_r}{r} + \frac{1}{r}\frac{\partial u_\theta}{\partial \theta} + \frac{\partial u_z}{\partial z} \end{aligned} \tag{3.2}$$

where ε_{rr}, ε_{zz}, $\varepsilon_{\theta\theta}$, $\varepsilon_{r\theta}$, $\varepsilon_{z\theta}$, ε_{rz} are the strain components, λ and μ are the Lamé constants.

The strain-displacement relations in cylindrical coordinates are given by:

$$\begin{aligned} \varepsilon_{rr} &= \frac{\partial u_r}{\partial r} \\ \varepsilon_{\theta\theta} &= \frac{1}{r}\frac{\partial u_\theta}{\partial \theta} + \frac{u_r}{r} \\ \varepsilon_{zz} &= \frac{\partial u_z}{\partial z} \\ \varepsilon_{r\theta} &= \frac{1}{2}\left(\frac{1}{r}\frac{\partial u_r}{\partial \theta} + \frac{\partial u_\theta}{\partial r} - \frac{u_\theta}{r}\right) \\ \varepsilon_{z\theta} &= \frac{1}{2}\left(\frac{1}{r}\frac{\partial u_z}{\partial \theta} + \frac{\partial u_\theta}{\partial z}\right) \\ \varepsilon_{rz} &= \frac{1}{2}\left(\frac{\partial u_z}{\partial r} + \frac{\partial u_r}{\partial z}\right) \end{aligned} \tag{3.3}$$

The substitution of Eqs. (3.3) and (3.2) into Eqs. (3.1) gives the equations of motion with displacements as dependent variables.
If I consider the axisymmetric case only, the equations of motion are:

$$\begin{cases} \rho \dfrac{\partial^2 u_r}{\partial t^2} = (\lambda + 2\mu)\left(\dfrac{\partial^2 u_r}{\partial r^2} + \dfrac{1}{r}\dfrac{\partial u_r}{\partial r} - \dfrac{u_r}{r^2} \right) + (\lambda + \mu)\dfrac{\partial^2 u_z}{\partial r \partial z} + \mu \dfrac{\partial^2 u_r}{\partial z^2} \\ \rho \dfrac{\partial^2 u_z}{\partial t^2} = (\lambda + \mu)\left(\dfrac{1}{r}\dfrac{\partial u_r}{\partial z} + \dfrac{\partial^2 u_r}{\partial r \partial z} \right) + (\lambda + 2\mu)\dfrac{\partial^2 u_z}{\partial z^2} + \mu\left(\dfrac{\partial^2 u_z}{\partial r^2} + \dfrac{1}{r}\dfrac{\partial u_z}{\partial r} \right) \end{cases} \tag{3.4}$$

3.2. Wave equations solution

The displacement components for axisymmetric waves in the shell layer *S* are derived by solving Eq. (3.4) [7]:

$$\begin{cases} u_r^S = \{ -\alpha [J_1(\alpha r)A_1 + Y_1(\alpha r)A_2] + j\xi [J_1(\beta r)B_1 + Y_1(\beta r)B_2] \} e^{j(\omega t + \xi z)} \\ u_z^S = \{ j\xi [J_0(\alpha r)A_1 + Y_0(\alpha r)A_2] - \beta [J_0(\beta r)B_1 + Y_0(\beta r)B_2] \} e^{j(\omega t + \xi z)} \end{cases} \tag{3.5}$$

with

$$\begin{aligned} \alpha^2 &= \frac{\omega^2}{c_p^2} - \xi^2 \\ \beta^2 &= \frac{\omega^2}{c_s^2} - \xi^2 \end{aligned} \tag{3.6}$$

where c_p and c_s are the compressional and shear velocities in the pipe shell, ω is the angular frequency, ξ is the mode wavenumber, A_i, B_i are unknown coefficients, $J_n(x)$ and $Y_n(x)$ are the Bessel functions of the first and second kind, respectively, of order *n*.
The displacement components in the internal layer *I* are derived from the same equations, but discarding those solutions that give an infinite value for $r = 0$ (Bessel functions of second kind). I can write:

$$\begin{cases} u_r^I = \{ -\alpha_I J_1(\alpha_I r)C_1 + j\xi J_1(\beta_I r)C_2 \} e^{j(\omega t + \xi z)} \\ u_z^I = \{ j\xi J_0(\alpha_I r)C_1 - \beta J_0(\beta_I r)C_2 \} e^{j(\omega t + \xi z)} \end{cases} \tag{3.7}$$

Similar reasoning holds for the external layer *E*, except that, since the layer is infinite radially, Bessel functions of second kind are not discarded but merged with Bessel function of first kind by means of Hankel functions

$$\begin{cases} u_r^E = \left\{ -\alpha_E H_1^{(2)}(\alpha_E r) D_1 + j\xi H_1^{(2)}(\beta_E r) D_2 \right\} e^{j(\omega t + \xi z)} \\ u_z^E = \left\{ j\xi H_0^{(2)}(\alpha_E r) D_1 - \beta_E H_0^{(2)}(\beta_E r) D_2 \right\} e^{j(\omega t + \xi z)} \end{cases} \tag{3.8}$$

where C_i, D_i are other unknown coefficients, $H_n^{(2)}$ are the Hankel functions of the second kind and of order *n*.

$$\begin{aligned} \alpha_{(I,E)}^2 &= \frac{\omega^2}{c_{p(I,E)}^2} - \xi^2 \\ \beta_{(I,E)}^2 &= \frac{\omega^2}{c_{s(I,E)}^2} - \xi^2 \end{aligned} \tag{3.9}$$

Caution must be taken to the selection of the correct root for α_E and β_E.
In fact the sign of these wavenumbers determines whether the wave mode radiates (is leaky) to the external medium or not; Muggleton et al. [4] among other authors (Junger, [20], Rama Rao & Vandiver [6], Long et al. [12]) claim that the guided wave may or may not radiate into the external medium depending on its wavespeed relative to the wavespeed in the surrounding medium.
The choice of the proper root will be treated in Section 3.6.

3.3. Boundary conditions

In order to find the solution of the propagation problem (displacements and stresses) in the waveguide constituted by the shell *S*, the internal core *I* and the external layer *E*, I need to find the constants of the motion present in Eqs. (3.5), (3.7) and (3.8) for *S*, *I* and *E*, respectively. The constants are obtained by imposing the boundary conditions to the pipe structure, whose section is depicted in Figure 3.1.
The boundary conditions are the same for both internal and external shell interfaces, but clearly apply to different media and positions:

$$\begin{aligned} &\text{Condition 1.} \quad \tau_{rr}^S\big|_{(b,a)} = \tau_{rr}^{(I,E)}\big|_{(b,a)} \\ &\text{Condition 2.} \quad \tau_{rz}^S\big|_{(b,a)} = \tau_{rz}^{(I,E)}\big|_{(b,a)} \\ &\text{Condition 3.} \quad u_r^S\big|_{(b,a)} = u_r^{(I,E)}\big|_{(b,a)} \\ &\text{Condition 4.} \quad u_z^S\big|_{(b,a)} = u_z^{(I,E)}\big|_{(b,a)} \end{aligned} \tag{3.10}$$

The previous equations describe the continuity of the radial stress τ_{rr}, of the shear stress τ_{rz}, and of the radial and tangential displacements, u_r and u_z, at the interfaces of radial coordinate equal to *b* and *a*.

Boundary condition 1

Condition 1. $\tau_{rr}^{S}\big|_{(b,a)} = \tau_{rr}^{(I,E)}\big|_{(b,a)}$

The radial stress τ_{rr}, is given by:

$$\tau_{rr} = \lambda\left(\frac{\partial u_r}{\partial r} + \frac{u_r}{r} + \frac{\partial u_z}{\partial z}\right) + 2\mu\frac{\partial u_r}{\partial r} = (\lambda + 2\mu)\frac{\partial u_r}{\partial r} + \lambda\left(\frac{u_r}{r} + \frac{\partial u_z}{\partial z}\right) \tag{3.11}$$

The derivatives $\frac{\partial u_r}{\partial r}$ and $\frac{\partial u_z}{\partial z}$, are obtained by Eqs. (3.5) (3.7) and (3.8), respectively:

$$\frac{\partial u_r^S}{\partial r} = \left\{-\alpha^2\left[J_1'(\alpha r)A_1 + Y_1'(\alpha r)A_2\right] + j\xi\beta\left[J_1'(\beta r)B_1 + Y_1'(\beta r)B_2\right]\right\}e^{j(\omega t+\xi z)} \tag{3.12}$$

$$\frac{\partial u_z^S}{\partial z} = \left\{-\xi^2\left[J_0(\alpha r)A_1 + Y_0(\alpha r)A_2\right] - j\xi\beta\left[J_0(\beta r)B_1 + Y_0(\beta r)B_2\right]\right\}e^{j(\omega t+\xi z)} \tag{3.13}$$

$$\frac{\partial u_r^I}{\partial r} = \left[-\alpha_I^2 J_1'(\alpha_I r)C_1 + j\xi\beta_I J_1'(\beta_I r)C_2\right]e^{j(\omega t+\xi z)} \tag{3.14}$$

$$\frac{\partial u_z^I}{\partial z} = \left[-\xi^2 J_0(\alpha_I r)C_1 - j\xi\beta_I J_0(\beta_I r)C_2\right]e^{j(\omega t+\xi z)} \tag{3.15}$$

$$\frac{\partial u_r^E}{\partial r} = \left[-\alpha_E^2 H_1'^{(2)}(\alpha_E r)D_1 + j\xi\beta_E H_1'^{(2)}(\beta_E r)D_2\right]e^{j(\omega t+\xi z)} \tag{3.16}$$

$$\frac{\partial u_z^E}{\partial z} = \left[-\xi^2 H_0^{(2)}(\alpha_E r)D_1 - j\xi\beta_E H_0^{(2)}(\beta_E r)D_2\right]e^{j(\omega t+\xi z)} \tag{3.17}$$

Substituting the Eqs. (3.12)-(3.15) into the Eq. (3.11), for the shell and the internal medium, and imposing the Eq. (3.10.1) at the internal interface ($r = b$), I obtain the following expression:

$$
\begin{aligned}
&(\lambda+2\mu)\left\{-\alpha^2\left[J_1'(\alpha b)A_1+Y_1'(\alpha b)A_2\right]+j\xi\beta\left[J_1'(\beta b)B_1+Y_1'(\beta b)B_2\right]\right\}+\\
&+\frac{\lambda}{b}\left\{-\alpha\left[J_1(\alpha b)A_1+Y_1(\alpha b)A_2\right]+j\xi\left[J_1(\beta b)B_1+Y_1(\beta b)B_2\right]\right\}+\\
&+\lambda\left\{-\xi^2\left[J_0(\alpha b)A_1+Y_0(\alpha b)A_2\right]-j\xi\beta\left[J_0(\beta b)B_1+Y_0(\beta b)B_2\right]\right\}+\\
&-(\lambda_I+2\mu_I)\left[-\alpha_I^2 J_1'(\alpha_I b)C_1+j\xi\beta_I J_1'(\beta_I b)C_2\right]+\\
&-\frac{\lambda_I}{b}\left[-\alpha_I J_1(\alpha_I b)C_1+j\xi J_1(\beta_I b)C_2\right]+\\
&-\lambda_I\left[-\xi^2 J_0(\alpha_I b)C_1-j\xi\beta_I J_0(\beta_I b)C_2\right]=0
\end{aligned}
\tag{3.18}
$$

Similarly, substituting the Eqs. (3.12), (3.13), (3.16), (3.17) into the Eq. (3.11), for the pipe shell and for the external layer, and imposing the Eq. (3.10.1) at the external interface ($r=a$), I obtain the following expression:

$$
\begin{aligned}
&(\lambda+2\mu)\left\{-\alpha^2\left[J_1'(\alpha a)A_1+Y_1'(\alpha a)A_2\right]+j\xi\beta\left[J_1'(\beta a)B_1+Y_1'(\beta a)B_2\right]\right\}+\\
&+\frac{\lambda}{a}\left\{-\alpha\left[J_1(\alpha a)A_1+Y_1(\alpha a)A_2\right]+j\xi\left[J_1(\beta a)B_1+Y_1(\beta a)B_2\right]\right\}+\\
&+\lambda\left\{-\xi^2\left[J_0(\alpha a)A_1+Y_0(\alpha a)A_2\right]-j\xi\beta\left[J_0(\beta a)B_1+Y_0(\beta a)B_2\right]\right\}+\\
&-(\lambda_E+2\mu_E)\left[-\alpha_E^2 J_1'(\alpha_E a)D_1+j\xi\beta_E J_1'(\beta_E a)D_2\right]+\\
&-\frac{\lambda_E}{a}\left[-\alpha_E J_1(\alpha_E a)D_1+j\xi J_1(\beta_E a)D_2\right]+\\
&-\lambda_E\left[-\xi^2 J_0(\alpha_E a)D_1-j\xi\beta_E J_0(\beta_E a)D_2\right]=0
\end{aligned}
\tag{3.19}
$$

Boundary condition 2

Condition 2. $\tau_{rz}^{S}\big|_{(b,a)}=\tau_{rz}^{(I,E)}\big|_{(b,a)}$

The shear stress τ_{rz}, is given by:

$$
\tau_{rz}=\mu\left(\frac{\partial u_z}{\partial r}+\frac{\partial u_r}{\partial z}\right) \tag{3.20}
$$

The derivatives $\frac{\partial u_z}{\partial r}$ and $\frac{\partial u_r}{\partial z}$, for the shell, are obtained from Eq. (3.5):

$$
\frac{\partial u_z^S}{\partial r}=\left\{j\alpha\xi\left[J_0'(\alpha r)A_1+Y_0'(\alpha r)A_2\right]-\beta^2\left[J_0'(\beta r)B_1+Y_0'(\beta r)B_2\right]\right\}e^{j(\omega t+\xi z)} \tag{3.21}
$$

$$\frac{\partial u_r^S}{\partial z} = \left\{ - j\alpha\xi\left[J_1(\alpha r)A_1 + Y_1(\alpha r)A_2\right] - \xi^2\left[J_1(\beta r)B_1 + Y_1(\beta r)B_2\right]\right\} e^{j(\omega t+\xi z)} \tag{3.22}$$

The derivatives $\frac{\partial u_z}{\partial r}$ and $\frac{\partial u_r}{\partial z}$ for internal and external layers are obtained from Eqs. (3.7) and (3.8)

$$\frac{\partial u_z^I}{\partial r} = \left\{ j\alpha_I \xi J_0'(\alpha_I r)C_1 - \beta_I^2 J_0'(\beta_I r)C_2 \right\} e^{j(\omega t+\xi z)} \tag{3.23}$$

$$\frac{\partial u_r^I}{\partial z} = \left\{ - j\alpha_I \xi J_1(\alpha_I r)C_1 - \xi_I^2 J_1(\beta_I r)C_2 \right\} e^{j(\omega t+\xi z)} \tag{3.24}$$

$$\frac{\partial u_z^E}{\partial r} = \left\{ j\alpha_E \xi H_0'(\alpha_E r)D_1 - \beta_E^2 H_0'(\beta_E r)D_2 \right\} e^{j(\omega t+\xi z)} \tag{3.25}$$

$$\frac{\partial u_r^E}{\partial z} = \left\{ - j\alpha_E \xi J_1(\alpha_E r)D_1 - \xi_E^2 J_1(\beta_E r)D_2 \right\} e^{j(\omega t+\xi z)} \tag{3.26}$$

Substituting the Eqs. (3.21)-(3.24) (3.26) into the Eq.(3.20) and imposing the Eq. (3.10.2) at the internal interface I obtain the following expression:

$$\begin{aligned} &\mu\left\{ \begin{array}{l} j\alpha\xi\left[J'_0(\alpha b)A_1 + Y'_0(\alpha b)A_2\right] - \beta^2\left[J'_0(\beta b)B_1 + Y'_0(\beta b)B_2\right] + \\ - j\alpha\xi\left[J_1(\alpha b)A_1 + Y_1(\alpha b)A_2\right] - \xi^2\left[J_1(\beta b)B_1 + Y_1(\beta b)B_2\right] \end{array} \right\} + \\ &- \mu_I \left\{ \begin{array}{l} j\alpha_I \xi J'_0(\alpha_I b)C_1 - \beta_I^2 J'_0(\beta_I b)C_2 + \\ - j\alpha_I \xi J_1(\alpha_I b)C_1 - \xi^2 J_1(\beta_I b)C_2 \end{array} \right\} = 0 \end{aligned} \tag{3.27}$$

Substituting the Eqs. (3.21),(3.22), (3.25), (3.26) into the Eq.(3.20) and imposing the Eq. (3.10.2) at the external interface:

$$\begin{aligned} &\mu\left\{ \begin{array}{l} j\alpha\xi\left[J'_0(\alpha a)A_1 + Y'_0(\alpha a)A_2\right] - \beta^2\left[J'_0(\beta a)B_1 + Y'_0(\beta a)B_2\right] + \\ - j\alpha\xi\left[J_1(\alpha a)A_1 + Y_1(\alpha a)A_2\right] - \xi^2\left[J_1(\beta a)B_1 + Y_1(\beta a)B_2\right] \end{array} \right\} + \\ &- \mu_E \left\{ \begin{array}{l} j\alpha_E \xi J'_0(\alpha_E a)D_1 - \beta_E^2 J'_0(\beta_E a)D_2 + \\ - j\alpha_E \xi J_1(\alpha_E a)D_1 - \xi^2 J_1(\beta_E a)D_2 \end{array} \right\} = 0 \end{aligned} \tag{3.28}$$

Boundary condition 3

Condition 3. $u_r^S\big|_{(b,a)} = u_r^{(I,E)}\big|_{(b,a)}$

By substituting the radial displacements at the internal interface, for the shell and the internal core, given by the Eqs. (3.5) and (3.7), in the Eq. (3.10.3), I derive:

$$\begin{aligned}&-\alpha\left[J_1(\alpha b)A_1+Y_1(\alpha b)A_2\right]+j\xi\left[J_1(\beta b)B_1+Y_1(\beta b)B_2\right]+\\&-\left[-\alpha_I J_1(\alpha_I b)C_1+j\xi J_1(\beta_I b)C_2\right]=0\end{aligned} \tag{3.29}$$

The same for the external interface:

$$\begin{aligned}&-\alpha\left[J_1(\alpha a)A_1+Y_1(\alpha a)A_2\right]+j\xi\left[J_1(\beta a)B_1+Y_1(\beta a)B_2\right]+\\&-\left[-\alpha_E H_1^{(2)}(\alpha_E a)D_1+j\xi H_1^{(2)}(\beta_E a)D_2\right]=0\end{aligned} \tag{3.30}$$

Boundary condition 4

Condition 4. $u_z^S\big|_{(b,a)}=u_z^{(I,E)}\big|_{(b,a)}$

By substituting the tangential displacements at the internal interface, for the shell and for the internal core, given by Eqs. (3.5) and (3.7), in Eq. (3.10.4), I derive:

$$\begin{aligned}&j\xi\left[J_0(\alpha b)A_1+Y_0(\alpha b)A_2\right]-\beta\left[J_0(\beta b)B_1+Y_0(\beta b)B_2\right]+\\&-\left[j\xi J_0(\alpha_I b)C_1-\beta_I J_0(\beta_I b)C_2\right]=0\end{aligned} \tag{3.31}$$

The same for the external interface:

$$\begin{aligned}&j\xi\left[J_0(\alpha a)A_1+Y_0(\alpha a)A_2\right]-\beta\left[J_0(\beta a)B_1+Y_0(\beta a)B_2\right]+\\&-\left[j\xi H_0^{(2)}(\alpha_E a)D_1-\beta_E H_0^{(2)}(\beta_E a)D_2\right]=0\end{aligned} \tag{3.32}$$

3.4. Boundary equations system

In the previous section I have derived four equations for each of the two interfaces, obtaining 8 equations in 8 unknowns A_1, A_2, B_1, B_2, C_1, C_2, D_1, D_2.
In order to calculate such coefficients, I have to solve a system of eight linear homogeneous algebraic equations, which can be written in matrix form

$$\begin{bmatrix} L_{11} & L_{12} & L_{13} & L_{14} & L_{15} & L_{16} & L_{17} & L_{18} \\ L_{21} & L_{22} & L_{23} & L_{24} & L_{25} & L_{26} & L_{27} & L_{28} \\ L_{31} & L_{32} & L_{33} & L_{34} & L_{35} & L_{36} & L_{37} & L_{38} \\ L_{41} & L_{42} & L_{43} & L_{44} & L_{45} & L_{46} & L_{47} & L_{48} \\ L_{51} & L_{52} & L_{53} & L_{54} & L_{55} & L_{56} & L_{57} & L_{58} \\ L_{61} & L_{62} & L_{63} & L_{64} & L_{65} & L_{66} & L_{67} & L_{68} \\ L_{71} & L_{72} & L_{73} & L_{74} & L_{75} & L_{76} & L_{77} & L_{78} \\ L_{81} & L_{82} & L_{83} & L_{84} & L_{85} & L_{86} & L_{87} & L_{88} \end{bmatrix} \begin{bmatrix} A_1 \\ A_2 \\ B_1 \\ B_2 \\ C_1 \\ C_2 \\ D_1 \\ D_2 \end{bmatrix} = 0 \tag{3.33}$$

This system yields nontrivial solutions when the determinant of L vanishes.
The elements of the matrix L are found by comparing the equations of this system with the boundary conditions:
Row 1 with Eq. (3.18)
Row 2 with Eq. (3.27)
Row 3 with Eq. (3.29)
Row 4 with Eq. (3.31)
Row 5 with Eq. (3.19)
Row 6 with Eq. (3.28)
Row 7 with Eq. (3.30)
Row 8 with Eq. (3.32)

3.5. Solution matrix elements

I report here the 64 elements of matrix L

$$L_{11} = -\left[\lambda\left(\alpha^2 + \xi^2\right) + 2\mu\alpha^2\right] J_0(\alpha b) + \frac{2\mu\alpha}{b} J_1(\alpha b) \tag{3.34}$$

$$L_{12} = -\left[\lambda\left(\alpha^2 + \xi^2\right) + 2\mu\alpha^2\right] Y_0(\alpha b) + \frac{2\mu\alpha}{b} Y_1(\alpha b) \tag{3.35}$$

$$L_{13} = j2\mu\xi\beta\left[J_0(\beta b) - \frac{1}{\beta b} J_1(\beta b)\right] \tag{3.36}$$

$$L_{14} = j2\mu\xi\beta\left[Y_0(\beta b) - \frac{1}{\beta b} Y_1(\beta b)\right] \tag{3.37}$$

$$L_{15} = \left[\lambda_I\left(\alpha_I^2 + \xi^2\right) + 2\mu_I\alpha_I^2\right] J_0(\alpha_I b) - \frac{2\mu_I\alpha_I}{b} J_1(\alpha_I b) \tag{3.38}$$

$$L_{16} = -j2\mu_I\xi\beta_I\left[J_0(\beta_I b) - \frac{1}{\beta_I b} J_1(\beta_I b)\right] \tag{3.39}$$

$$L_{17} = 0 \tag{3.40}$$

$$L_{18} = 0 \tag{3.41}$$

$$L_{21} = -j2\mu\xi\alpha J_1(\alpha b) \tag{3.42}$$

$$L_{22} = -j2\mu\xi\alpha Y_1(\alpha b) \tag{3.43}$$

$$L_{23} = \mu(\beta^2 - \xi^2)J_1(\beta b) \tag{3.44}$$

$$L_{24} = \mu(\beta^2 - \xi^2)Y_1(\beta b) \tag{3.45}$$

$$L_{25} = j2\mu_I\xi\alpha_I J_1(\alpha_I b) \tag{3.46}$$

$$L_{26} = -\mu_I(\beta_I^2 - \xi^2)J_1(\beta_I b) \tag{3.47}$$

$$L_{27} = 0 \tag{3.48}$$

$$L_{28} = 0 \tag{3.49}$$

$$L_{31} = -\alpha J_1(\alpha b) \tag{3.50}$$

$$L_{32} = -\alpha Y_1(\alpha b) \tag{3.51}$$

$$L_{33} = j\xi J_1(\beta b) \tag{3.52}$$

$$L_{34} = j\xi Y_1(\beta b) \tag{3.53}$$

$$L_{35} = \alpha_I J_1(\alpha_I b) \tag{3.54}$$

$$L_{36} = -j\xi J_1(\beta_I b) \tag{3.55}$$

$$L_{37} = 0 \tag{3.56}$$

$$L_{38} = 0 \tag{3.57}$$

$$L_{41} = j\xi J_0(\alpha b) \tag{3.58}$$

$$L_{42} = j\xi Y_0(\alpha b) \tag{3.59}$$

$$L_{43} = -\beta J_0(\beta b) \tag{3.60}$$

$$L_{44} = -\beta Y_0(\beta b) \tag{3.61}$$

$$L_{45} = -j\xi J_0(\alpha_I b) \tag{3.62}$$

$$L_{46} = \beta J_0(\beta_I b) \tag{3.63}$$

$$L_{47} = 0 \tag{3.64}$$

$$L_{48} = 0 \tag{3.65}$$

$$L_{51} = -\left[\lambda\left(\alpha^2 + \xi^2\right) + 2\mu\alpha^2\right] J_0(\alpha a) + \frac{2\mu\alpha}{a} J_1(\alpha a) \tag{3.66}$$

$$L_{52} = -\left[\lambda\left(\alpha^2 + \xi^2\right) + 2\mu\alpha^2\right] Y_0(\alpha a) + \frac{2\mu\alpha}{a} Y_1(\alpha a) \tag{3.67}$$

$$L_{53} = j2\mu\xi\beta\left[J_0(\beta a) - \frac{1}{\beta a} J_1(\beta a)\right] \tag{3.68}$$

$$L_{54} = j2\mu\xi\beta\left[Y_0(\beta a) - \frac{1}{\beta a} Y_1(\beta a)\right] \tag{3.69}$$

$$L_{55} = 0 \tag{3.70}$$

$$L_{56} = 0 \tag{3.71}$$

$$L_{57} = \left[\lambda_E\left(\alpha_E^2 + \xi^2\right) + 2\mu_E\alpha^2\right] H_0(\alpha_E a) - \frac{2\mu_E\alpha_E}{a} H_1(\alpha_E a) \tag{3.72}$$

$$L_{58} = -j2\mu_E\xi\beta_E\left[H_0^{(2)}(\beta_E a) - \frac{1}{\beta_E a} H_1^{(2)}(\beta_E a)\right] \tag{3.73}$$

$$L_{61} = -j2\mu\xi\alpha J_1(\alpha a) \tag{3.74}$$

$$L_{62} = -j2\mu\xi\alpha Y_1(\alpha a) \tag{3.75}$$

$$L_{63} = \mu\left(\beta^2 - \xi^2\right) J_1(\beta a) \tag{3.76}$$

$$L_{64} = \mu\left(\beta^2 - \xi^2\right) Y_1(\beta a) \tag{3.77}$$

$$L_{65} = 0 \tag{3.78}$$

$$L_{66} = 0 \tag{3.79}$$

$$L_{67} = j2\mu_E\xi\alpha_E H_1^{(2)}(\alpha_E a) \tag{3.80}$$

$$L_{68} = -\mu_E\left(\beta_E^2 - \xi^2\right) H_1^{(2)}(\beta_E a) \tag{3.81}$$

$$L_{71} = -\alpha J_1(\alpha a) \tag{3.82}$$

$$L_{72} = -\alpha Y_1(\alpha a) \tag{3.83}$$

$$L_{73} = j\xi J_1(\beta a) \tag{3.84}$$

$$L_{74} = j\xi Y_1(\beta a) \tag{3.85}$$

$$L_{75} = 0 \tag{3.86}$$

$$L_{76} = 0 \tag{3.87}$$

$$L_{77} = \alpha_E H_1^{(2)}(\alpha_E a) \tag{3.88}$$

$$L_{78} = -j\xi H_1^{(2)}(\beta_E a) \tag{3.89}$$

$$L_{81} = j\xi J_0(\alpha a) \tag{3.90}$$

$$L_{82} = j\xi Y_0(\alpha a) \tag{3.91}$$

$$L_{83} = -\beta J_0(\beta a) \tag{3.92}$$

$$L_{84} = -\beta Y_0(\beta a) \tag{3.93}$$

$$L_{85} = 0 \tag{3.94}$$

$$L_{86} = 0 \tag{3.95}$$

$$L_{87} = -j\xi H_0^{(2)}(\alpha_E a) \tag{3.96}$$

$$L_{88} = \beta_E H_0^{(2)}(\beta_E a) \tag{3.97}$$

3.6. Choice of wavenumbers

The radial wavenumbers to be input in the solution matrix elements (α_I, β_I, α, β, α_E, β_E) must be computed through a square root operation and this open the possibility to the choice between 2 roots which differ from their sign. For all internal layers both roots give the same results whereas for the external layer it is important to choose the correct root. This section discusses and proves these aspects.

Internal layers

The sign of wavenumbers in internal layers, core and shells, is not important. The proof is here given for elastic media, the fluid case is equivalent (see Section 3.10).

The general expressions for displacements in the shell layers, of which the core case is a special case when $A_2 = B_2 = 0$, as function of either possible root for both (P-wave and S-wave) wavenumbers (α, β), are

$$\begin{aligned} u_r(\alpha,\beta) &= \{-\alpha[J_1(\alpha r)A_1 + Y_1(\alpha r)A_2] + j\xi[J_1(\beta r)B_1 + Y_1(\beta r)B_2]\}e^{j(\omega t+\xi z)} \\ u_z(\alpha,\beta) &= \{j\xi[J_0(\alpha r)A_1 + Y_0(\alpha r)A_2] - \beta[J_0(\beta r)B_1 + Y_0(\beta r)B_2]\}e^{j(\omega t+\xi z)} \end{aligned} \tag{3.98}$$

Let's consider the following relations between Bessel functions that hold for any $z \in C$, obtainable from Abramowitz and Stegun [21], Eq. 9.1.35 and 9.1.36).

$$\begin{aligned} J_0(-z) &= J_0(z) \\ J_1(-z) &= -J_1(z) \\ Y_0(-z) &= Y_0(z) \\ Y_1(-z) &= -Y_1(z) \end{aligned} \tag{3.99}$$

Displacements can be therefore expressed as function of the other roots (of opposite sign) of both wavenumbers:

$$\begin{aligned} u_r(-\alpha,-\beta) &= \{-\alpha[J_1(\alpha r)A_1 + Y_1(\alpha r)A_2] + j\xi[J_1(\beta r)\tilde{B}_1 + Y_1(\beta r)\tilde{B}_2]\}e^{j(\omega t+\xi z)} \\ u_z(-\alpha,-\beta) &= \{j\xi[J_0(\alpha r)A_1 + Y_0(\alpha r)A_2] - \beta[J_0(\beta r)\tilde{B}_1 + Y_0(\beta r)\tilde{B}_2]\}e^{j(\omega t+\xi z)} \end{aligned} \tag{3.100}$$

with $\tilde{B}_1 = -B_1$, $\tilde{B}_2 = -B_2$.
Therefore the sign of α is completely compensated, which means that coefficients A_1, A_2 remain the same for both signs of α and the sign change of β causes a sign change of coefficients B_1, B_2, which anyway are unknowns.
In conclusion whatever sign for radial wavenumbers (α and β) is chosen when dealing with internal layers, the solution doesn't change.
This is not true for the external layer.

External layers
In the external layer the solution completely changes according to the sign of radial wavenumber chosen. Again the proof is given for elastic media.
The general expressions for displacements in the external layer, as function of either possible root for both (P-wave and S-wave) wavenumbers, are

$$\begin{cases} u_r^E(\alpha_E,\beta_E) = [-\alpha_E H_1^{(2)}(\alpha_E r)D_1 + j\xi H_1^{(2)}(\beta_E r)D_2]e^{j(\omega t+\xi z)} \\ u_z^E(\alpha_E,\beta_E) = [j\xi H_0^{(2)}(\alpha_E r)D_1 - \beta_E H_0^{(2)}(\beta_E r)D_2]e^{j(\omega t+\xi z)} \end{cases} \tag{3.101}$$

Let's consider the following relations between Hankel functions that hold for any $z \in C$, obtainable from Abramowitz and Stegun [21], Eq. 9.1.39:

$$\begin{aligned} H_0^{(2)}(-z) &= -H_0^{(1)}(z) \\ H_1^{(2)}(-z) &= H_1^{(1)}(z) \end{aligned} \tag{3.102}$$

Again displacements can be expressed as function of the other roots (of opposite sign) of both wavenumbers

$$\begin{cases} u_r^E(-\alpha_E,-\beta_E) = \left[+\alpha_E H_1^{(1)}(\alpha_E r)D_1 + j\xi H_1^{(1)}(\beta_E r)D_2\right]e^{j(\omega t+\xi z)} \\ u_z^E(-\alpha_E,-\beta_E) = \left[-j\xi H_0^{(1)}(\alpha_E r)D_1 - \beta_E H_0^{(1)}(\beta_E r)D_2\right]e^{j(\omega t+\xi z)} \end{cases} \tag{3.103}$$

Therefore in addition to the change of sign of D_1, the important result is that, by changing the sign of the wavenumbers, the Hankel functions of 2nd kind turned into Hankel functions of 1st kind (when the same arguments is kept).
Therefore the solution will surely be different according to the choice of the wavenumber sign.
Now let's try to answer the question on which is the correct sign to be used, references are Muggleton [4], Pavlakovic [10] and Lowe [9].
The Hankel functions of the 2nd kind were originally chosen because, with $e^{j\omega t}$ time-dependence, they represent outgoing waves, but this is true only if the real part of the argument is positive, otherwise they are ingoing waves as Hankel functions of 1st kind as shown in previous equations.
Therefore it would seem that one has to choose always the root with positive real part; instead there are cases when one has to choose the other root so that the wave is actually coming in.
To understand this, as explained by Muggleton [4], let's think in terms of real wavenumbers, possibly with negligible attenuation: the wave radiates only if the wavenumber in the surrounding medium, say k is greater than the axial wavenumber ξ (Figure 3.3), therefore in case the medium wavespeed is lower than the phase velocity considered. In this case I choose the radial wavenumber, say α, with positive real part, which means outgoing wave.

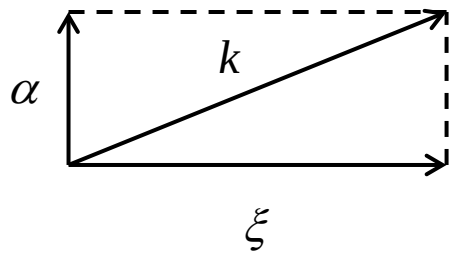

Figure 3.3. Vector composition of wavenumber.

If the wavenumber in the surrounding medium is lower than the axial wavenumber, the wave cannot radiate, therefore it will die exponentially in the radial direction. Analytically this corresponds to choose the root with negative imaginary part.
These concepts are well formalized in Pavlakovic [10] and are here adapted to the different time convention:
Let's consider a radial wavenumber in the external layer and let it be called α, even if it can represent any kind of partial wave (P- or S-wave), let c_{bulk} be the considered partial wave velocity

$$\alpha = \pm\sqrt{\left(\frac{\omega}{c_{bulk}}\right)^2 - \xi^2} \tag{3.104}$$

The sign of the radial wavenumber α is chosen according to this condition

$$\text{If } \operatorname{Re}\left[\left(\frac{\omega}{c_{bulk}}\right)^2\right] > \operatorname{Re}\left[\xi^2\right] \Rightarrow \qquad \operatorname{Re}[\alpha] > 0$$

$$\text{If } \operatorname{Re}\left[\left(\frac{\omega}{c_{bulk}}\right)^2\right] < \operatorname{Re}\left[\xi^2\right] \Rightarrow \qquad \operatorname{Im}[\alpha] < 0$$

3.7. Conditioning of solution matrix

Before dealing with the root-finding procedure there are some numerical problems to be solved.
In fact, the solution matrix, as it is written above, is ill-conditioned since some elements are much larger than others and this causes the numerical computation of the determinant to be inaccurate or even impossible.
This occurs mainly for two reasons:

- the presence of the Lamé parameters (very large numerical value) only in some rows of the matrix;
- the presence of Bessel and Hankel functions which diverge if their argument has large imaginary part.

The first problem is solved by dividing by μ the matrix rows containing the Lamé parameters (rows 1, 2, 5 and 6).
A similar approach is used to prevent Bessel and Hankel functions to diverge. This usually happens to Bessel and Hankel whose argument contains a wavenumber with high imaginary part. Such Bessel/Hankel functions can appear in columns 5, 6, 7 and 8 of the solution matrix (in case the core and/or the external layer are fluid).

Therefore, each of these columns has been divided by the corresponding Bessel or Hankel function:

- Column 5 is divided by $J_0(\alpha_I b)$
- Column 6 is divided by $J_0(\beta_I b)$
- Column 7 is divided by $H_0^{(2)}(\alpha_E a)$
- Column 8 is divided by $H_0^{(2)}(\beta_E a)$

There is also an overflow problem with very large imaginary arguments of the aforementioned Bessel/Hankel functions. With the above divisions, I obtain only ratios of 1st order to 0th order functions, which can be substituted with their asymptotical expression for very large arguments

$$\begin{aligned} \lim_{|\mathrm{Im}(z)|\to\infty} \frac{J_1(z)}{J_0(z)} &= j\cdot sign(\mathrm{Im}(z)) \\ \lim_{|\mathrm{Im}(z)|\to\infty} \frac{H_1(z)}{H_0(z)} &= j \end{aligned} \tag{3.105}$$

These approximations in the algorithm are performed when

$$\begin{aligned} &\left|\mathrm{Im}(z)\right| > 700 && z = \alpha_I b,\ \beta_I b \\ &\mathrm{Im}(z) < -15 \vee \mathrm{Im}(z) > 690 && z = \alpha_E a,\ \beta_E a \end{aligned}$$

The solution is now well conditioned and the determinant can be efficiently computed.
If unknown coefficients (A_1, A_2, B_1, B_2,…) are to be computed, the operations applied to the solution matrix coefficients must be taken into account to retrieve the correct values.
An important additional (or alternative) algorithmic device to improve the stability of the solution is to use the modified Bessel functions instead of the unmodified when the wavenumbers take specified values, this substitution implies other changes and is well explained by Pavlakovic [10].

3.8. Root-finding algorithm

The propagation parameters are obtained by finding the roots of the determinant of the matrix L.
Unfortunately the resulting equation cannot be solved analytically, therefore there's need for some numerical inversion procedure which is explained below.

Out of the many kinds of inversion algorithms, the choice so far has fallen on the exhaustive one: the determinant is computed for a given range of wavenumbers surrounding a first guess, and the solution is taken to be the first yielding a relative minimum. The functional to be minimized is the absolute value of the determinant of the solution matrix. The following list reports the inversion strategy:

- Choose a frequency for which the wavenumber is approximately known (elastic wide-tube model) and use it as first guess.
- Find the closest relative minimum of the functional and obtain the corresponding wavenumber solution.
- Use the solution as first guess for the next frequency.

A gradient method however is expected to be far more efficient and therefore is suggested in case of implementation.

3.9. Computation of field variable profiles

Once the root of the determinant of solution matrix are found, one can compute the values of unknowns $A_1, A_2, B_1, B_2, C_1, C_2, D_1, D_2$ and therefore also the profiles of field variables: stresses and displacements.
In principles the unknowns are simply equal to the null space of matrix *L*, but because of the scaling applied to the solution matrix (section 3.7), they must be properly (un)scaled.
The scaling applied to matrix rows doesn't matter at all because it equally acts on all coefficients, therefore it corresponds to the amplitude of the wave perturbation, whereas the scale factors applied to the matrix columns are important to retrieve the profiles because they are coefficients applied to the single unknown that must be a posteriori compensated. This is the case of columns 5, 6, 7, 8.
Therefore the null space of matrix L gives

$$\begin{bmatrix} A_1 & A_2 & B_1 & B_2 & \tilde{C}_1 & \tilde{C}_2 & \tilde{D}_1 & \tilde{D}_2 \end{bmatrix} = null(L) \tag{3.106}$$

where the tilde-signed variables are linked to the original unknowns through the same coefficients applied to the corresponding columns

$$\begin{aligned} \tilde{C}_1 &= C_1 J_0(\alpha_I b) \\ \tilde{C}_2 &= C_2 J_0(\beta_I b) \\ \tilde{D}_1 &= D_1 H_0^{(2)}(\alpha_E a) \\ \tilde{D}_2 &= D_2 H_0^{(2)}(\beta_E a) \end{aligned} \tag{3.107}$$

Therefore the displacements as function of radial coordinate in the internal layer are computed in this way

$$\begin{cases} u_r^I = -\alpha_I \dfrac{J_1(\alpha_I r)}{J_0(\alpha_I b)}\widetilde{C}_1 + j\xi \dfrac{J_1(\beta_I r)}{J_0(\alpha_I b)}\widetilde{C}_2 \\ u_z^I = j\xi \dfrac{J_0(\alpha_I r)}{J_0(\alpha_I b)}\widetilde{C}_1 - \beta \dfrac{J_0(\beta_I r)}{J_0(\alpha_I b)}\widetilde{C}_2 \end{cases} \tag{3.108}$$

Those in the external layer are obtained with obvious substitutions.
Stresses instead, according to equations (3.11) and (3.20) need also the values of $\frac{\partial u_r^I}{\partial r}$ and $\frac{\partial u_z^I}{\partial r}$, which are computed in this way

$$\begin{aligned} \frac{\partial u_r^I}{\partial r} &= -\alpha_I^2\left(\frac{J_0(\alpha_I r)}{J_0(\alpha_I b)} - \frac{1}{\alpha_I r}\frac{J_1(\alpha_I r)}{J_0(\alpha_I b)}\right)\widetilde{C}_1 + j\xi\beta_I\left(\frac{J_0(\beta_I r)}{J_0(\beta_I b)} - \frac{1}{\alpha_I r}\frac{J_1(\beta_I r)}{J_0(\beta_I b)}\right)\widetilde{C}_2 \\ \frac{\partial u_z^I}{\partial r} &= -j\alpha_I\xi\frac{J_1(\alpha_I r)}{J_0(\alpha_I b)}\widetilde{C}_1 + \beta_I^2\frac{J_1(\beta_I r)}{J_0(\beta_I b)}\widetilde{C}_2 \end{aligned} \tag{3.109}$$

and similarly $\frac{\partial u_r^E}{\partial r}$ and $\frac{\partial u_z^E}{\partial r}$.
As said before, there could be an overflow problem for large imaginary part of Bessel/Hankel arguments.
Therefore there's need for an approximation for the ratios of Bessel and Hankel functions whose arguments have large imaginary part. The ratio is between functions whose argument is not equal, so the approximation must be found as function of the ratio between arguments, that are therefore written in this way:

$$\frac{J_0(kz)}{J_0(z)}, \frac{J_1(kz)}{J_0(z)}, \frac{H_0^{(2)}(kz)}{H_0^{(2)}(z)}, \frac{H_1^{(2)}(kz)}{H_0^{(2)}(z)} \qquad \text{for} \qquad |\mathrm{Im}(z)| \to \infty,\ k \in \Re^+$$

In order to accomplish this, let's take the asymptotic expansions for large arguments in Abramowitz and Stegun [21] (p. 364, 9.2.1), in particular the expansions of the Hankel functions:

$$\begin{aligned} H_\nu^{(1)}(z) &\xrightarrow{|z|\to\infty} \sqrt{2/(\pi z)}e^{j(z-\nu\pi/2-\pi/4)} && -\pi < \arg(z) < 2\pi \\ H_\nu^{(2)}(z) &\xrightarrow{|z|\to\infty} \sqrt{2/(\pi z)}e^{-j(z-\nu\pi/2-\pi/4)} && -2\pi < \arg(z) < \pi \end{aligned} \tag{3.110}$$

where function *arg* takes the phase of the complex number.
Keeping in mind that $\arg(z) = \arg(kz) \quad \forall k \in \Re^+$, I can easily compute

$$\frac{H_0^{(2)}(kz)}{H_0^{(2)}(z)} = \frac{1}{\sqrt{k}} e^{-jz(k-1)}$$
$$\frac{H_1^{(2)}(kz)}{H_0^{(2)}(z)} = j\frac{1}{\sqrt{k}} e^{-jz(k-1)} \tag{3.111}$$

To obtain the ratio of Bessel functions I exploit the fact that the Bessel function is the average of the two Hankel functions

$$J_\nu(z) = \frac{H_\nu^{(1)}(z) + H_\nu^{(2)}(z)}{2} \xrightarrow{|z|\to\infty}$$
$$\xrightarrow{|z|\to\infty} \sqrt{1/(2\pi z)} e^{j(z-\nu\pi/2-\pi/4)} + \sqrt{1/(2\pi z)} e^{-j(z-\nu\pi/2-\pi/4)} \tag{3.112}$$

Then I distinguish two cases according to the sign of imaginary part and drop the complex exponential that tends to 0

$$\begin{aligned} J_\nu(z) &\xrightarrow{|z|\to\infty} \sqrt{1/(2\pi z)} e^{-j(z-\nu\pi/2-\pi/4)} && 0 < \arg(z) < \pi \\ J_\nu(z) &\xrightarrow{|z|\to\infty} \sqrt{1/(2\pi z)} e^{j(z-\nu\pi/2-\pi/4)} && -\pi < \arg(z) < 0 \end{aligned} \tag{3.113}$$

And finally get the ratios left:

$$\begin{aligned} \frac{J_0(kz)}{J_0(z)} &\xrightarrow{|z|\to\infty} \frac{1}{\sqrt{k}} e^{-jz(k-1)} && 0 < \arg(z) < \pi \\ \frac{J_0(kz)}{J_0(z)} &\xrightarrow{|z|\to\infty} \frac{1}{\sqrt{k}} e^{jz(k-1)} && -\pi < \arg(z) < 0 \end{aligned} \tag{3.114}$$

$$\begin{aligned} \frac{J_1(kz)}{J_0(z)} &\xrightarrow{|z|\to\infty} \frac{j}{\sqrt{k}} e^{-jz(k-1)} && 0 < \arg(z) < \pi \\ \frac{J_1(kz)}{J_0(z)} &\xrightarrow{|z|\to\infty} -\frac{j}{\sqrt{k}} e^{jz(k-1)} && -\pi < \arg(z) < 0 \end{aligned} \tag{3.115}$$

3.10. Adaptation to fluids

So far the formulation of the propagation model was referred to elastic solids, whose elastic parameters had to be specified: the first and second Lamé parameters.
This section explains and justifies how to turn any of the solid layers into a fluid where no shear waves exist but other phenomena are considered, viscosity and thermal conduction, including phenomena due to boundary layers.

The modification is accomplished solely in a replacement of Lamé parameters with a proper function of fluid parameters.
In a constructive procedure, first viscous only fluids are treated, then extension to thermo-viscous is accomplished.

Viscous fluid
The substitution to perform in order to consider viscous effects only, is reported by Baik et al. [16], who cites Nagy & Nayfeh [22]:

$$\begin{aligned} \lambda &\Leftarrow \rho c_f^2 \pm j\omega\left(\zeta - \frac{2}{3}\eta\right) \\ \mu &\Leftarrow \pm j\omega\eta \end{aligned} \tag{3.116}$$

Plus sign must be taken in case of $e^{j\omega t}$ time convention, present choice, minus sign in case of $e^{-j\omega t}$ time convention.
It is worth here to see some consequences of these substitutions:
The square of the P-wave velocity c_p

$$c_p^2 = \frac{\lambda + 2\mu}{\rho} = c_f^2 + \frac{j\omega}{\rho}\left(\zeta + \frac{4}{3}\eta\right) \tag{3.117}$$

has a real part which accounts for the pressure wave velocity and an imaginary part which accounts for bulk viscous friction.
The square of the S-wave velocity c_s

$$c_s^2 = \frac{\mu}{\rho} = \frac{j\omega\eta}{\rho} \tag{3.118}$$

is imaginary meaning that no shear wave exists anymore, but shear friction does.
The square of the radial wavenumbers α^2 and β^2

$$\alpha^2 = \frac{\omega^2}{c_p^2} - \xi^2 = \frac{\omega^2}{c_f^2 + \frac{j\omega}{\rho}\left(\zeta + \frac{4}{3}\eta\right)} - \xi^2 = \frac{1}{\frac{1}{k_f^2} + \frac{j}{\omega\rho}\left(\zeta + \frac{4}{3}\eta\right)} - \xi^2 \tag{3.119}$$

with $k_f^2 = \frac{\omega^2}{c_f^2}$

$$\beta^2 = \frac{\omega^2}{c_s^2} - \xi^2 = \frac{\omega\rho}{j\eta} - \xi^2 \tag{3.120}$$

are the same as in Elvira-Segura [15].
The normal τ_{rr} and tangential τ_{rz} stresses in case of fluids

$$\begin{aligned}
\tau_{rr} &= \lambda\left(\frac{\partial u_r}{\partial r}+\frac{u_r}{r}+\frac{\partial u_z}{\partial z}\right)+2\mu\frac{\partial u_r}{\partial r}= \\
&=\left[\rho c_f^2+j\omega\left(\zeta-\frac{2}{3}\eta\right)\right]\left(\frac{\partial u_r}{\partial r}+\frac{u_r}{r}+\frac{\partial u_z}{\partial z}\right)+2j\omega\eta\frac{\partial u_r}{\partial r} \\
\tau_{rz} &= \mu\left(\frac{\partial u_z}{\partial r}+\frac{\partial u_r}{\partial z}\right)= j\omega\eta\left(\frac{\partial u_z}{\partial r}+\frac{\partial u_r}{\partial z}\right)=\eta\left(\frac{\partial v_z}{\partial r}+\frac{\partial v_r}{\partial z}\right)
\end{aligned} \tag{3.121}$$

are the stresses of a Newtonian fluid (Newton stress tensor) in cylindrical coordinates in case of axisymmetry.

Thermo-viscous fluids
The addition of thermal effects is again reported by Baik et al. [16] citing Kinsler et al. [23] (pag. 210-218) as a modification of the P-wavenumber

$$c_p^2=\frac{\omega^2}{k^2}=c_f^2+\frac{j\omega}{\rho}\left(\zeta+\left(\frac{4}{3}+\frac{\gamma-1}{\mathrm{Pr}}\right)\eta\right) \tag{3.122}$$

But this modification concerns the bulk thermal effects, as one can verify by comparing it with the expression for the wavenumber k, computed for bulk thermo-viscous effects, given by Blackstock [1] (pages 305 ff.), and reported here with the present notation.

$$k=\pm\frac{\omega/c_f}{\sqrt{1+j\dfrac{\omega}{\rho c_f^2}\left(\zeta+\left(\dfrac{4}{3}+\dfrac{\gamma-1}{\mathrm{Pr}}\right)\eta\right)}} \tag{3.123}$$

In pipes such bulk effects at low frequency are negligible compared to the boundary effects, therefore like for viscous effects, boundary thermal phenomena must be inserted in the (pseudo) shear wave velocity c_s.
The expression is here derived following the reasoning of Blackstock [1] (pages 519-525):

The velocity profile in the viscous boundary layer depends on a "transversal wave" whose wavenumber is $k_s = \sqrt{\frac{\omega\rho}{2\eta}} + j\sqrt{\frac{\omega\rho}{2\eta}}$, which explains the presence of the "shear wave" whose square velocity is $c_s^2 = \frac{j\omega\eta}{\rho}$.

Therefore the shear wave accounts for the viscous boundary layer effect.

Then Blackstock gives the dispersion equation accounting for the viscous boundary layer which contains the parameter kinematic viscosity η/ρ, and states that in order to include the thermal boundary layer effect, it suffices to replace $\sqrt{\eta/\rho}$ with $\sqrt{\eta/\rho}\left(1+\frac{\gamma-1}{\sqrt{\mathrm{Pr}}}\right)$ in the dispersion equation (page 525), like it is reported also by Kinsler et al. [23] (pages 230-234);

Therefore one can deduce that, to include the thermal boundary layer effect, in the matrix method it suffices to apply the same replacement in the definition of c_s^2:

$$c_s^2 = \frac{j\omega\eta}{\rho}\left(1+\frac{\gamma-1}{\sqrt{\mathrm{Pr}}}\right)^2 \tag{3.124}$$

Such expression is clearly linked to the expression for attenuation according to the wide-tube approximation, Eq. (2.5), and therefore in this way the model adds the effect of thermal boundary layer analogously to the effect of the viscous boundary layer, in agreement with the wide-tube hypothesis.

Since $\lambda = \rho c_p^2 - 2\mu$, the substitutions for switching to a thermo-viscous fluid are finally

$$\lambda = \rho c_f^2 + j\omega\left\{\zeta + \eta\left[\frac{4}{3}+\frac{\gamma-1}{\mathrm{Pr}}-2\left(1+\frac{\gamma-1}{\sqrt{\mathrm{Pr}}}\right)^2\right]\right\} \tag{3.125a}$$

$$\mu = j\omega\eta\left(1+\frac{\gamma-1}{\sqrt{\mathrm{Pr}}}\right)^2 \tag{3.125b}$$

which are the substitutions implemented in the algorithm in case of fluid.

Density is here considered constant, an hypothesis certainly acceptable in case of liquids, whereas in case of gases it corresponds to the acoustic approximation, that is small variations of density (and pressure) compared to the equilibrium values.

These substitutions perhaps represent the most original (to the author's knowledge) contribution of the AXSYM-3L model which completes Baik's work [16].

In fact the boundary thermal effect in pipes is usually much more relevant than the bulk thermal effect at least at low frequency and the former is included in the model only through equation (3.125b).

In conclusion the AXSYM-3L model provides an automatic algorithm to compute propagation parameters curves (as well as field variables profiles) for three-layers cylindrical media, each layer can be either solid or liquid and in the latter case both boundary viscous and boundary thermal effects are included.
The major novelty of the AXSYM-3L model compared to the much more general Disperse, lies in the inclusion of boundary thermal effects.

4. AXSYM-3L model results

Previous chapter describes the algorithm AXSYM-3L for the computation of the propagation parameters of acoustic waves in cylindrical structures in all its aspects and makes possible to implement it, this chapter is meant to show and analyze some of the results about fluid-filled pipelines. I restrict to the fundamental fluid-borne propagation mode, which travels the most in pipelines.
In the first section some features of AXSYM-3L are tested by comparing its results with other literature models.
The following two sections are devoted to show the propagation parameters computed by the algorithm in an oil-filled pipe surrounded by different media, solid, liquid or gas.
The subsequent section compares the AXSYM-3L model with literature models described in Chapter 2 for the scenario of a buried oil-filled pipe.
The last section shows the profiles of the field variables, displacements and stresses for this same scenario at a typical frequency of 50 Hz.

4.1. Test of AXSYM-3L model

This section presents 4 tests of the AXSYM-3L algorithm for computing attenuation and dispersion curves of the first fluid-borne mode, each test concerns different scenarios and propagation phenomena.
The first two are meant to verify the effect of the external medium and therefore take as reference published results computed by the Disperse software (Long et al. [12]) at frequencies of the order of kHz.
The third has the aim to verify the addition of the boundary thermal effects in the propagation model (Section 3.10, Eq. (3.125)) and therefore takes as reference the wide-tube analytic approximation and is performed at low frequency.
The last test takes the results for attenuation of a thermo-viscous fluid-filled pipe published by Baik et al. [16] and compares them with those obtained by AXSYM-3L model.

4.1.1. Water-Steel-Water

This test intends to verify AXSYM-3L model as regards the external loading effect for a liquid-filled elastic pipe immersed in water on the dispersion curve of the first fluid-borne propagation mode.
Long et al. [12] (figure 6 in their paper) show dispersion curves computed with Disperse algorithm for some axisymmetric modes in a water-filled 10 in cast-iron pipe (16 mm wall thickness) immersed in water. The first fluid-borne mode is there labeled α1.
Figure 4.1 reports that figure with superimposed in red the results of AXISYM-3L for the same scenario and so-labeled mode α1, the fitting obtained between the

dispersion curves is very good with a minimum phase velocity at about 5 kHz whereas the attenuation is null because here Long et al. [12] neglects water viscosity and no external radiation takes place.

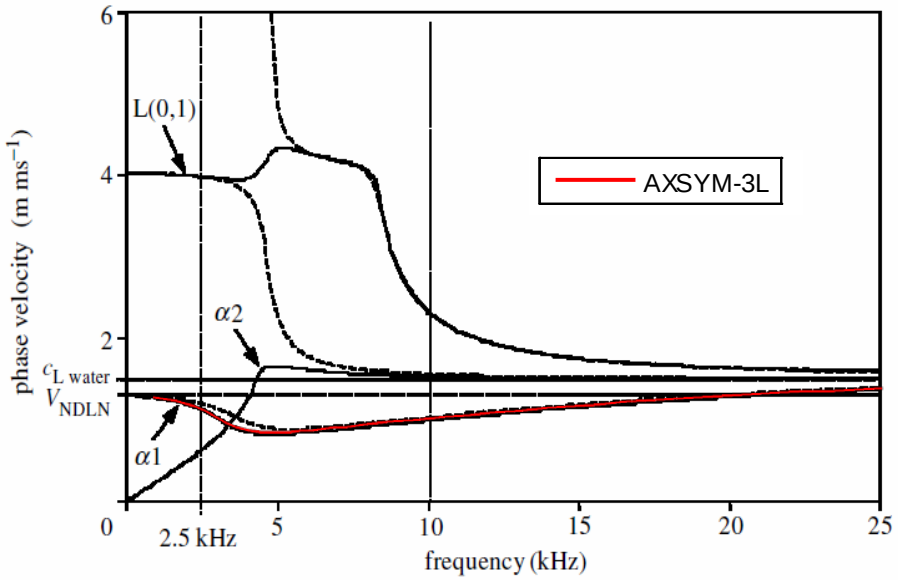

Figure 6. Phase velocity dispersion curves for axisymmetric modes in 10 in bore, cast-iron pipe (wall thickness 16 mm): w–p–v (dashed lines) and w–p–w (solid lines). Material properties are given in table 1. For clarity, higher-order modes are not shown.

Figure 4.1. Dispersion curves taken from Long et al. [12], with superimposed dispersion curve computed by AXISYM-3L for a water-filled pipe immersed in water.

4.1.2. Water-Steel-Soil

This test intends to verify AXSYM-3L model as regards the effect of the soil that surrounds a fluid-filled elastic pipe on the first fluid-borne propagation mode.
Long et al. [12] (figure 15 of their paper) show attenuation and dispersion curves computed with Disperse algorithm for the first fluid-borne mode α1 in a similar scenario as previous test, a water-filled 10 in cast-iron pipe (16 mm wall thickness), except that the pipe is buried in soil with variable P-wave velocity c_p (labeled c_L in the source notation), S-wave velocity is kept constant at 80 m/s.
Figure 4.2 reports that figure with superimposed as colored curves the results of AXISYM-3L for 4 extreme values of P-wave velocity $c_L := c_p$ written in the legend.
Again the results are the same and show two families of curves separated by the fact that c_L is greater or less than the non-dispersive in-pipe velocity (labeled V_{NDLN}) which is just the velocity expressed in Model 1, Eq. (2.1).

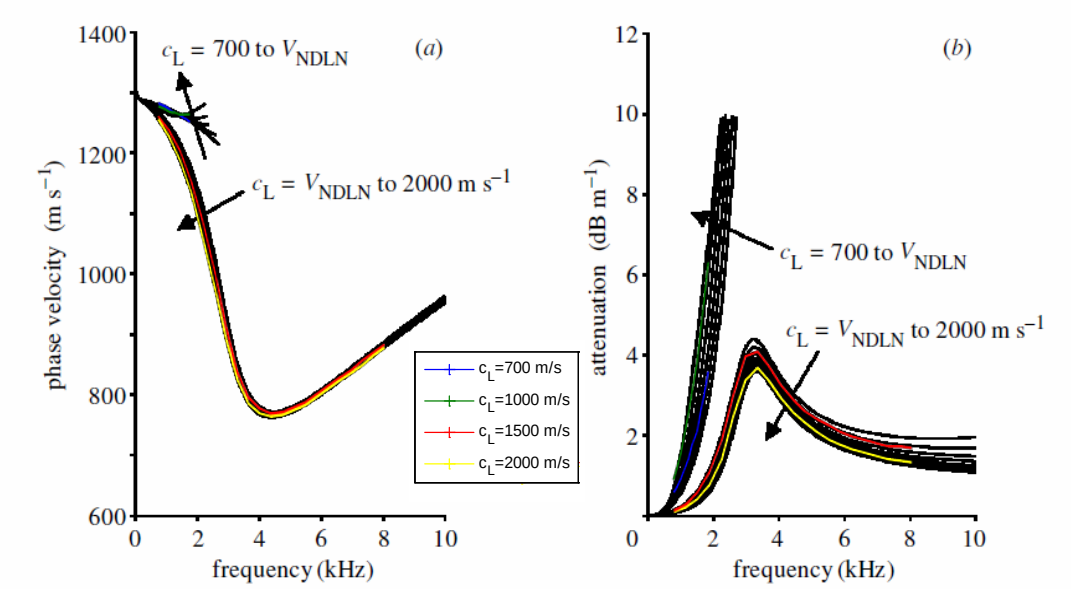

Figure 15. $\alpha 1$ mode dispersion curves below 10 dB m^{-1} for 10 in bore, cast-iron pipe (wall thickness 16 mm) surrounded by soil model with c_L = 700–2000 m s^{-1}. (*a*) Phase velocity. (*b*) Attenuation.

Figure 4.2. Dispersion and attenuation curves taken from Long et al. [12], with superimposed (colored) curves computed by AXISYM-3L for a buried water-filled pipe.

4.1.3. Air-Steel

This test is meant to prove the ability of the algorithm to compute propagation parameters of the fundamental fluid-borne mode in a gas-filled elastic pipe.
In this case, unlike liquids, the pipe is infinitely rigid to the gas, and the values of the pipe's physical properties are irrelevant like even the properties of any external medium.
On the contrary, the thermal effects are here important, in particular the boundary layer thermal, in addition to the usual viscous effects, and these can be accurately taken into account only by adding thermal terms in the shear wave velocity, Eq. (3.124) which leads to equation (3.125).
Therefore the results of AXISYM-3L are compared with those of Baik et al. [16] who, when dealing with thermo-viscous fluid mercury, include thermal terms in P-wave velocity (Eq. 13) but don't report that they modify S-wave velocity, which was actually not so important in their scenario, as next section shows.
It is important instead in this scenario (Table 4.1) at low frequency, where the simple analytic wide-tube approximation, Model 2 (Section 2.1.2) can offer an accurate term of comparison (even without elastic pipe correction).
I consider standard condition air in 40 cm diameter, 11 mm thick steel pipe, all parameters of the waveguide are precisely listed in Table 4.1.

Physical and geometrical parameters			
Symbol	Value	Unit	Description
Pipe geometry			
b	0.2	m	Pipe internal radius
h	0.0111	m	Pipe thickness
Internal fluid - Air			
ρ_f	1.23	kg/m^3	Density
c_f	340	m/s	Speed of sound in free medium
η	1.8x10^{-5}	Pas	Dynamic viscosity
γ	1.4	-	Specific heats ratio
Pr	0.71	-	Prandtl number
Shell material – Steel			
ρ_p	7800	kg/m^3	density
E	2x10^{11}	Pa	Young modulus
ν	0.3	-	Poisson ratio

Table 4.1. Parameters for test scenario.

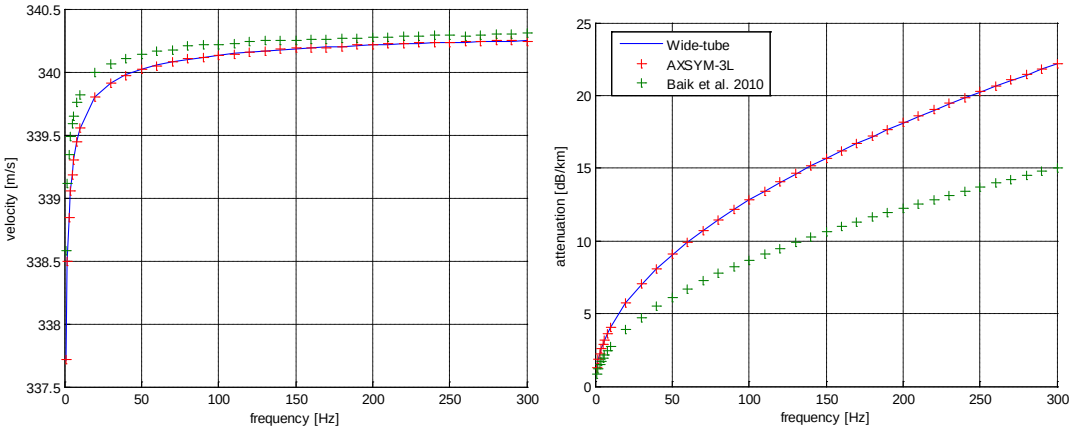

Figure 4.3. Dispersion and attenuation curves in a gas-filled pipe.

Figure 4.3 displays the propagation parameters as function of frequency computed with the three models, AXISYM-3L model closely follows the analytic Wide-tube curve whereas Baik's model does not because it doesn't take into account the thermal boundary layer but only the bulk thermal effect.

4.1.4. Mercury-steel

The previous test has displayed a relevant difference between AXISYM-3L model and that of Baik et al. [16] in the considered scenario and the former model resulted more accurate.

This test has the objective to assess the difference of results between the two models in the scenario described by [16] themselves which deals with another thermo-viscous fluid, mercury, enclosed in a 6.41 cm inner radius steel shell surrounded by vacuum (in this last feature the model is similar to Model 6, Elvira-Segura's [15]).

In figure 12 of [16], authors show dispersion and attenuation curves for that waveguide as function of a dimensionless frequency $k_1 b$ in a quite high frequency range (for instance $k_1 b = 2$ corresponds to about 7.2 kHz). The fundamental fluid-borne mode is here labeled ET0.

Figure 4.4 reports those figures with superimposed as red curve the results by AXISYM-3L up to a frequency of 20 kHz, the difference between the results of the two models cannot be detected in that scale, but even by looking closer to the curves, there is only a slight negligible difference in the attenuation.

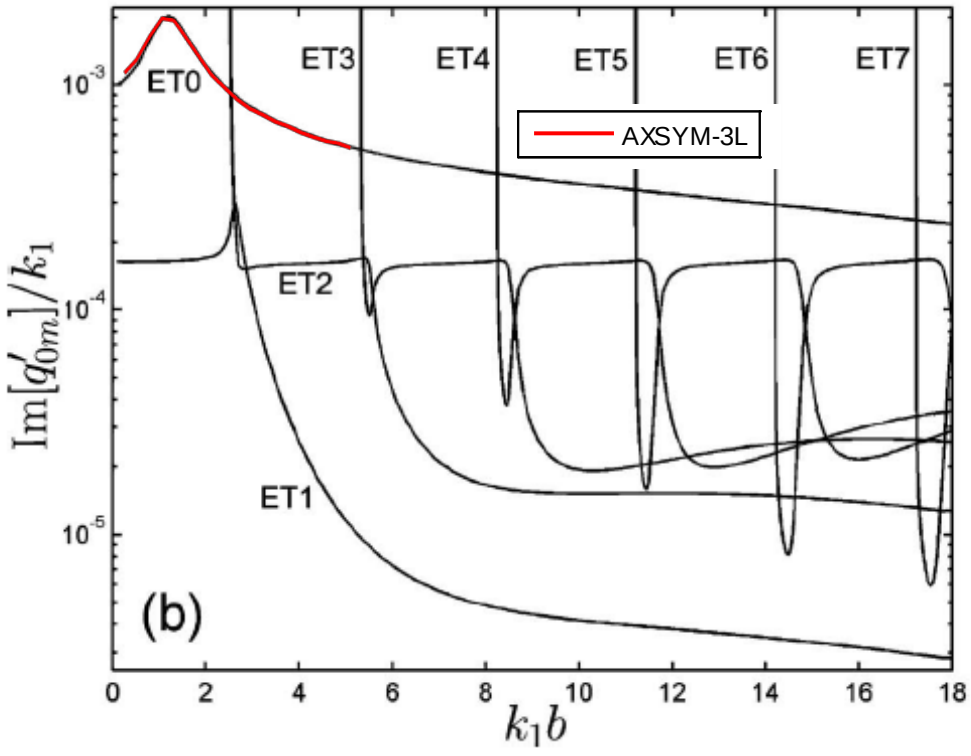

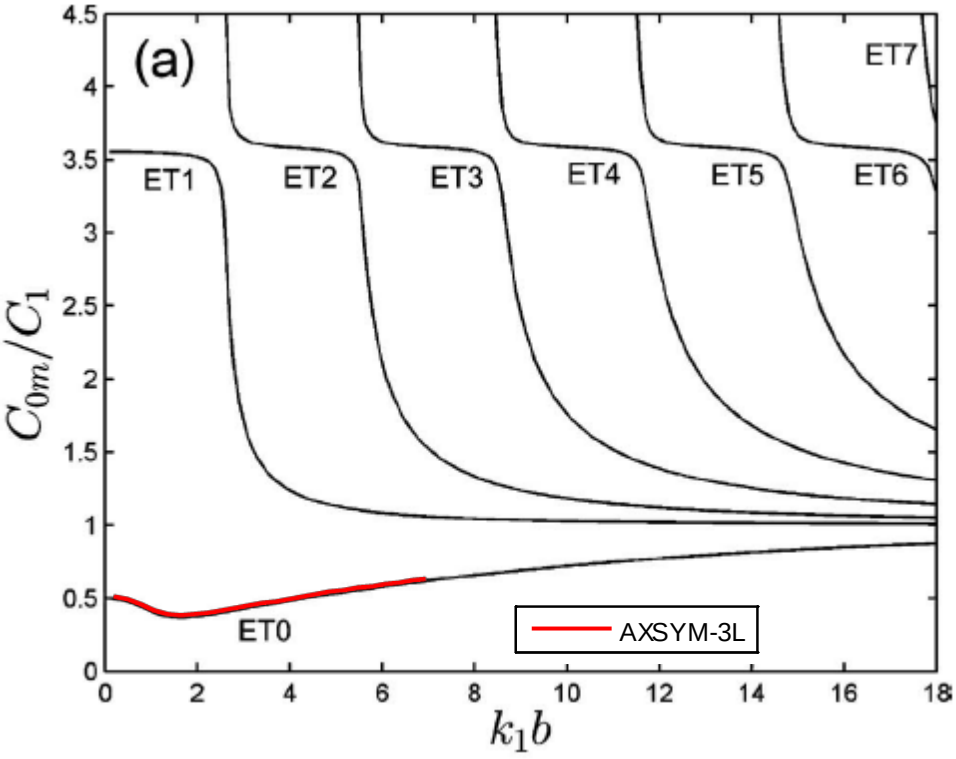

Figure 4.4. Dispersion and attenuation curves in a mercury-filled pipe taken from Baik et al. [16] with superimposed in red some results from AXISYM-3L.

At such high frequency in fact the bulk (viscous and thermal) effects are much larger than the boundary effects, while they are not in test 4.1.3, and this explain why Baik et al. [16] didn't need to include boundary thermal effects; at low frequency instead, the inclusion is needed.

4.2. Sensitivity to surrounding medium parameters

AXISYM-3L model is now analyzed in order to assess how propagation parameters (wavenumber) change as function of media parameters.

For gas pipelines, due to the high difference between the acoustic impedance of the gas and of the pipe shell, even at high pressure, the rigid tube assumption remains valid (Model 2 in section 2.1.2), and the influence of the external medium is negligible.

This is not true for oil pipelines: I show here the sensitivity of the propagation curves versus the external solid parameters, namely density and P-wave velocity. The shear wave velocity c_s is kept dependent on P-wave velocity c_s and computed as

$$c_s = c_p / \sqrt{3}\,.$$

Figure 4.5 shows the propagation parameters for variations of the surrounding medium density (other parameters fixed to the values in Table 2.1): along such variation, the phase velocity ranges from the value it would have without load (like in Elvira-Segura model which corresponds to null external density) to the free space velocity (like in rigid pipe approximation, high external density) whereas the increase in density reduces the attenuation at lower frequency (as tending to rigid pipe) but enhances it at higher frequency.

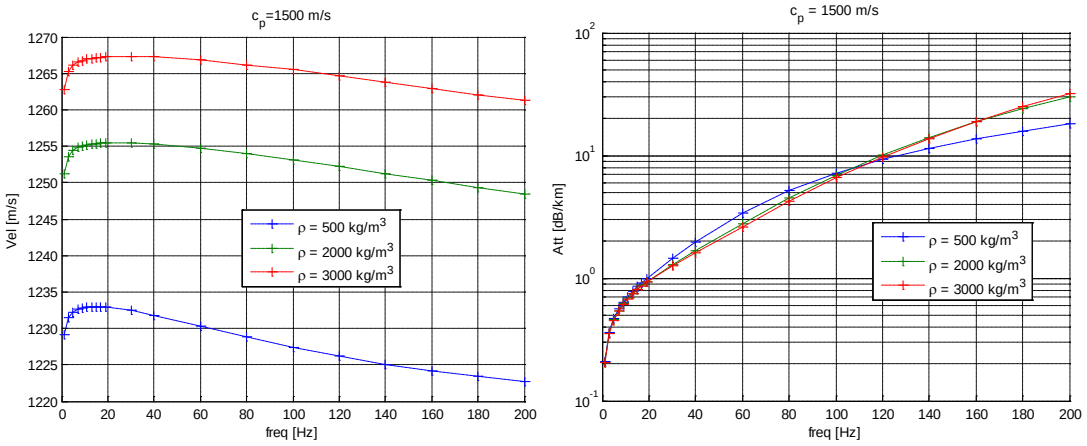

Figure 4.5. Phase velocity and attenuation for different values of surrounding medium density. External medium parameters are set as follows: c_p=1500 m/s, c_s=900 m/s.

Figure 4.6 shows the propagation parameters for variations of the surrounding medium P-wave velocity (other parameters fixed to the values in Table 2.1). An increase of the surrounding medium velocity corresponds to an increase of the system rigidity; conclusions, as regards dispersion, are similar to those aforesaid in case of density variations. Attenuation due to the external medium (radiation) takes place only if the medium wavespeed (either shear or compressional) is lower than the guided wave velocity. In figure, no radiation takes place for c_p=3000 m/s, only shear wave radiation for c_p=1500 m/s (and c_s=870 m/s), both shear and compressional wave radiation for c_p=700 m/s (and c_s=400 m/s).

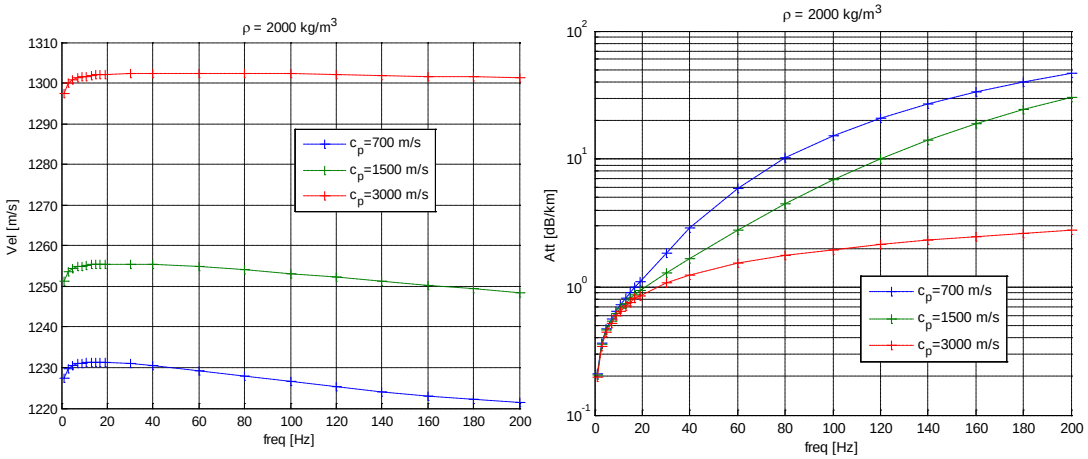

Figure 4.6. Phase velocity and attenuation for different values of surrounding medium P-wave velocity. External medium parameters are set as follows: ρ=2000 kg/m^3, $c_s = c_p / \sqrt{3}$.

4.3. Propagation parameters in buried/submerged oil pipelines

It is interesting also to analyze the propagation parameters for an oil pipeline buried or submerged: the difference is in the external medium. I consider again the oil pipeline with geometrical and filling-fluid parameters in Table 2.1, surrounded by three different media: air, water and dry loose sand (media properties in Table 4.2). Two acoustic and one elastic external media.
Attenuation factor and phase velocity are shown in Figure 4.7.

Surrounding medium: dry loose sand			
Symbol	**Value**	**Unit**	**Description**
ρ_m	2000	kg/m^3	Density
c_p	340	m/s	P-wave speed
c_s	200	m/s	S-wave speed
Surrounding medium: air			
Symbol	**Value**	**Unit**	**Description**
ρ_m	1	kg/m^3	Density
c_p	340	m/s	P-wave speed
η	1.8x10^{-5}	Pa*s	Dynamic viscosity
Surrounding medium: water			
Symbol	**Value**	**Unit**	**Description**
ρ_m	1000	kg/m^3	Density

c_p	1500	m/s	P-wave speed
η	$1x10^{-3}$	Pa*s	Dynamic viscosity

Table 4.2. Elastic parameters of 3 different surrounding media.

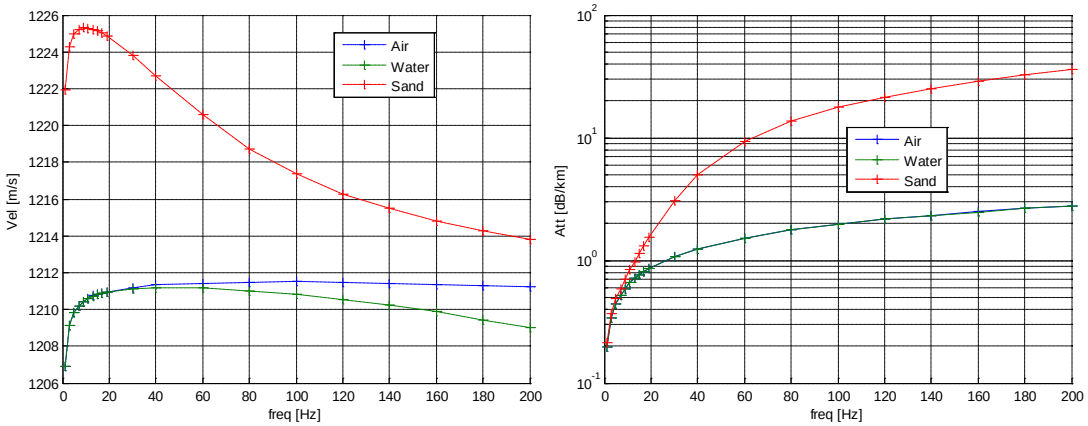

Figure 4.7. Phase velocity and attenuation for different surrounding media.

Sand provokes a much higher attenuation, in fact it enables radiation both of shear and pressure waves, whereas no radiation takes place in acoustic media. In case of air because its density is negligible to the pipe's, in case of water because its P-wave velocity is higher than the mode's velocity and no shear waves exist.
The phase velocity is instead quite similar in the three cases.

4.4. Comparison with literature models

In this section the results of AXISYM-3L model are compared with those of the models selected from literature and described in Chapter 2 for the scenario defined in Table 2.1, shortly buried oil pipe.
The following plots show the propagation curves computed with the AXISYM-3L model together with those of the other models up to 200 Hz, please notice that the vertical axis of the attenuation plot is set to logarithmic scale to cope with the large interval spanned by the attenuation coefficient.

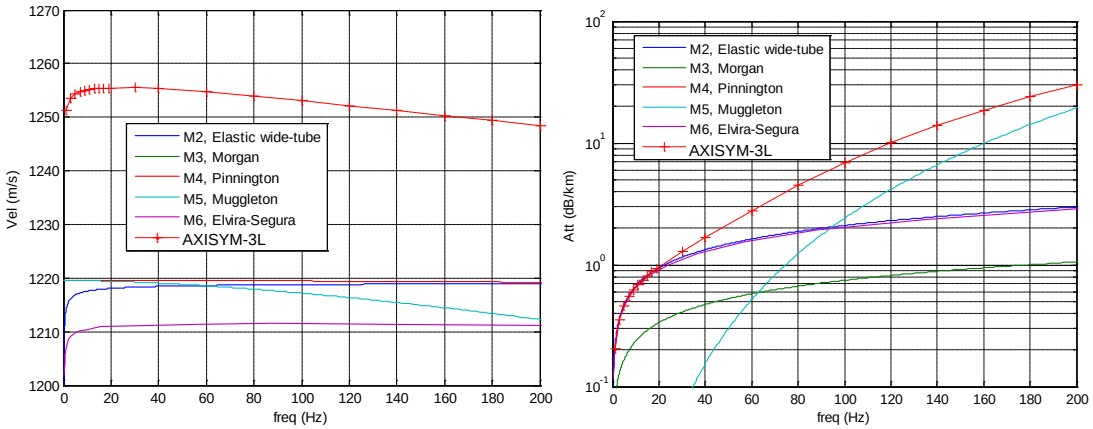

Figure 4.8. Phase velocity and attenuation computed with selected models.

The attenuation curve of the new model AXSYM-3L fits the curve of Elvira-Segura [15] (elastic wide-tube) up to about 20 Hz; for higher frequencies it begins to increase severely tending to approach the Muggleton [4] model.
The phase velocity looks quite higher than all the other models: this is due to the high P velocity of the medium surrounding the pipe, i.e. the stiffness of the solid external load makes the waveguide more rigid, increasing the wave speed.
As regards to the dispersion curve shape, at low frequency it is similar to Elvira-Segura and elastic wide-tube, whereas at higher frequencies the decrease resembles that of Muggleton [4].
Therefore the AXSYM-3L model is able to fit the attenuation curve of the elastic wide tube model at low frequency, the curve of Muggleton [4] at high frequency and to link these two curves with a transition curve not available otherwise.

4.5. Profiles of field variables

Finding a root for the determinant of the solution matrix at a given frequency implies finding also the values of the unknowns ($A_1, A_2, B_1, B_2, C_1, C_2, D_1, D_2$) that determine the dependence of the displacements (and stresses) on the radial coordinate as described in Section 3.9.
The next figures therefore will show as an example the profiles of 4 field variables for a buried oil-filled pipe at the frequency of 50 Hz.
In the axisymmetric case, a proper set of field variables is radial u_r and axial u_z displacements, normal τ_{rr} and shear τ_{rz} stresses, all these are expressed in physical units by setting the normal stress in oil (acoustic pressure) to a value of 1 bar, each graph shows the magnitude and the phase of the complex variables.
All parameters are still set to the values in Table 2.1.

Figure 4.9 shows the displacements up to a distance from the axis of 2 m, the main displacement is in oil in the axial direction, whereas the radial displacement has its maximum in the pipe and progressively decreases both in oil and in soil.
Actually the radial displacement doesn't tend to 0 but has a minimum at large distance and then increases again (this is not shown in the plot), which is the reason for attenuation due to radiation outward.

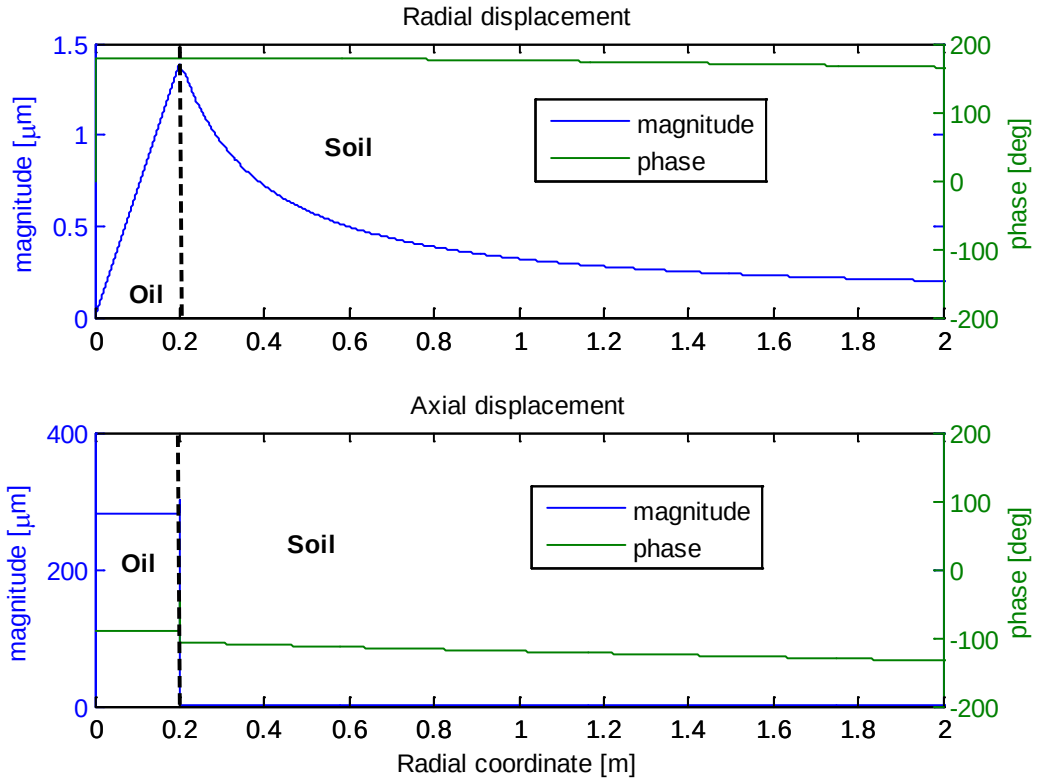

Figure 4.9. Radial and axial displacements in a buried oil-filled pipe at 50 Hz.

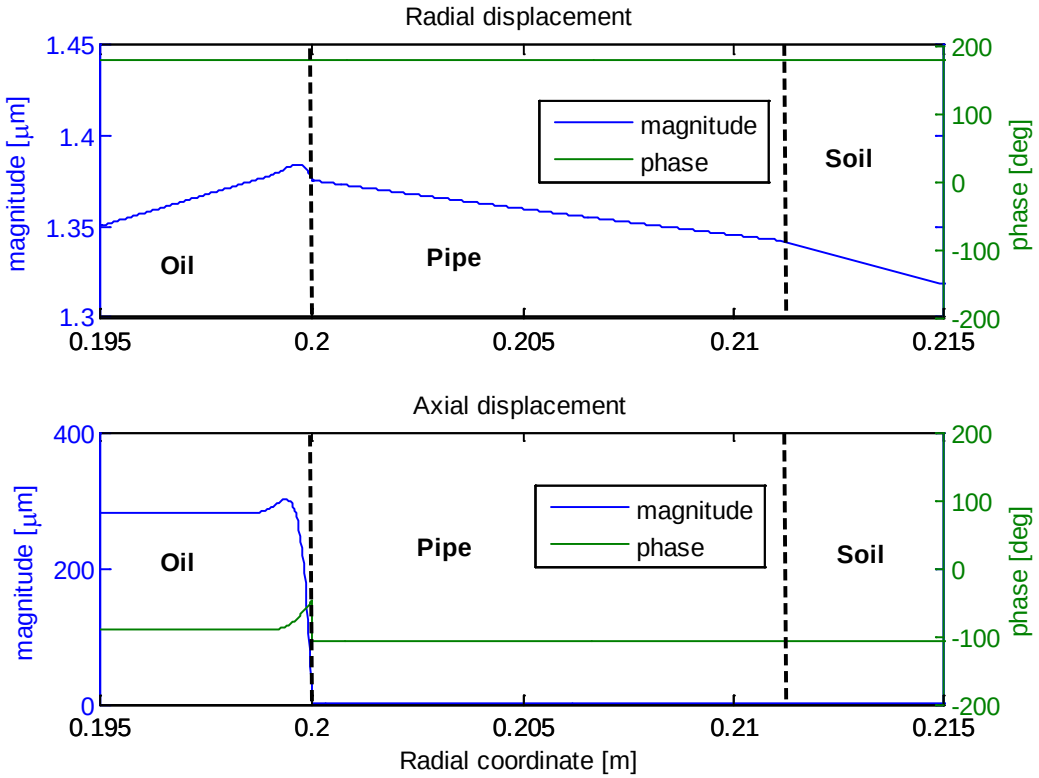

Figure 4.10. Radial and axial displacements in a buried oil-filled pipe at 50 Hz.. Zoom around pipe.

Figure 4.10 is a zoom around pipe, here particularly interesting is the boundary layer in the fluid where the axial displacement ranges from 0 to the plateau value, and the radial displacement has its maximum actually just in the boundary layer. The boundary layer is responsible for the viscous (also thermal in gas) attenuation at low frequency.

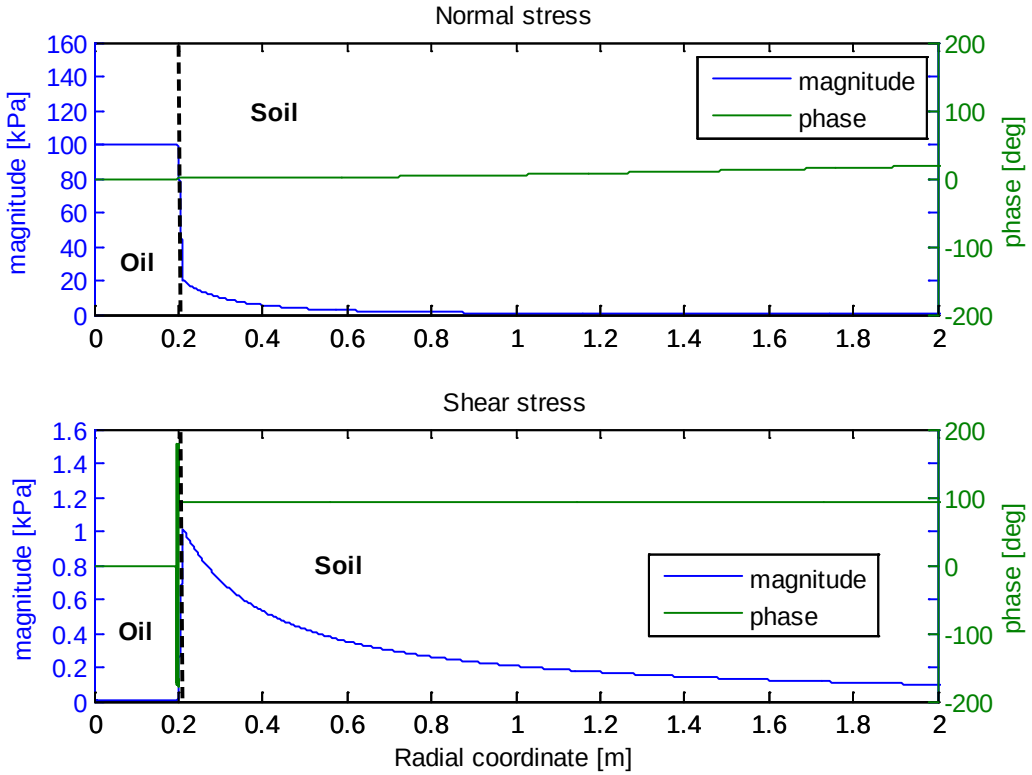

Figure 4.11. Normal and shear stresses in a buried oil-filled pipe at 50 Hz.

Figure 4.11 shows the stresses up to 2 m far from the pipe axis, the main stress is the pressure in oil whereas the shear stress is maximum in the pipe shell.

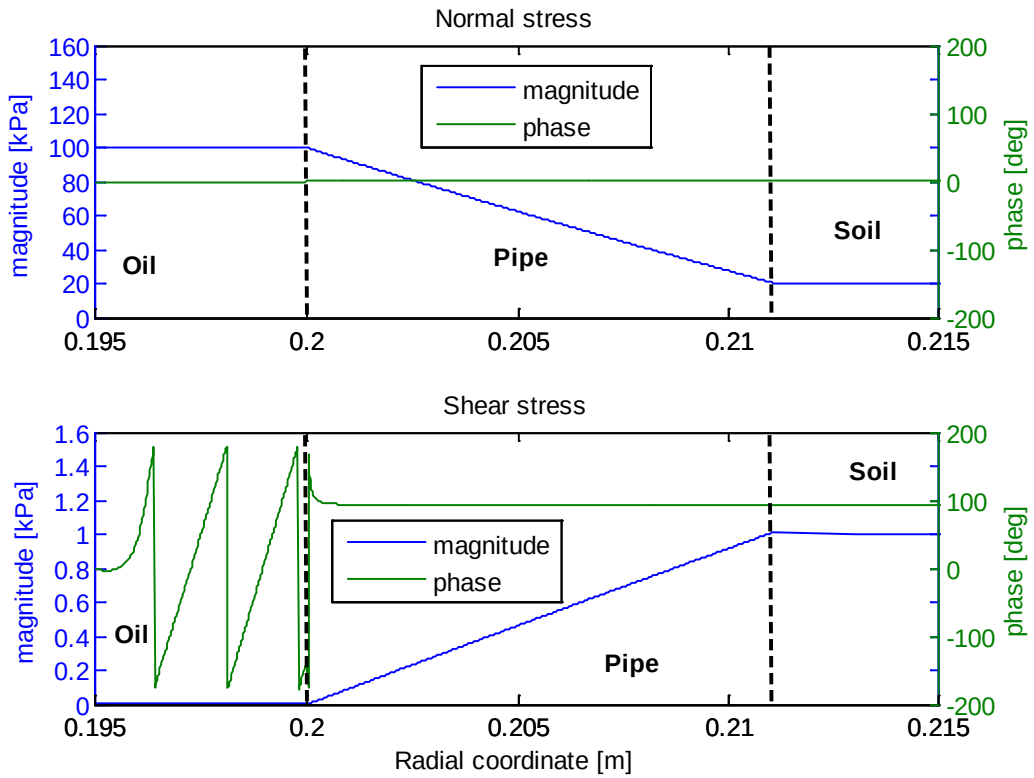

Figure 4.12. Normal and shear stresses in a buried oil-filled pipe at 50 Hz.. Zoom around pipe

The zoom of Figure 4.12 shows just linear links from values in oil to those in soil, the wrapping in the phase of the shear stress looks strange but the magnitude is close to zero in that interval.

Conclusion

The literature review on models of wave propagation in pipelines pointed out the need of a complete matrix method to take accurately into account all phenomena of propagation relevant in practical situations of pipeline monitoring.
A complete matrix method, called AXSYM-3L, was entirely derived from the basic equations considering 3 cylindrical (visco-) elastic media, the external of infinite radial extent; the wave equations in each medium were found as function of a proper set of unknowns. The continuity boundary conditions were applied to displacements and stresses at the two interfaces, resulting in a linear system of 8 equations in 8 unknowns.
The solution for the propagation parameters is found by setting the determinant of solution matrix to zero, which requires a numerical method in order to be computed.
A posteriori, any of the solid layer can be turned into a thermo-viscous fluid by a proper redefinition of Lamé parameters.
The method is thus presented in such a detail that it can be reproduced and methods are suggested to overcome possible numerical problems.
In consideration of the model scope, only axisymmetric propagation modes are considered.
The novelty compared to the commercial software Disperse lies in the fact that it can model thermal effects, both bulk and boundary layer, which is important normally in gas-filled pipes.
AXSYM-3L was successfully tested for fluid-filled pipes limitedly to the fundamental fluid-borne mode.
As regards the surrounding medium effect, results of Disperse software at high sonic frequency available in literature were taken as reference and verification included both the load effect on dispersion in case of external liquid and the radiation effect on attenuation in case of external solid.
In another test I have taken as reference the wide-tube approximation at low frequency in order to test the boundary layer thermal effect, in addition to the viscous.
The AXSYM-3L was compared to the other simpler models described and proved to be able to take into account all the phenomena it was design to.
Finally profiles of field variables in physical units, namely displacements and stresses, computed by AXSYM-3L were shown for the fundamental fluid-borne mode at 50 Hz. Profiles show in particular 2 reasons for attenuation: the boundary layer in the fluid close to the pipe and the movement of the external medium which doesn’t die out with radial coordinate.

Part II: Experimental validation and technological impact

Introduction

In part I of the thesis I discussed the theory of acoustic wave propagation in pipelines in a way that it was functional to the development of a research project called Dionisio, which I contributed to.
The aim of the project, promoted and supported by eni, the Italian oil company, was the design of a registered vibro-acoustic system for remote real-time monitoring of pipelines (e-vpms®). The system relies on a discrete network of pressure and vibration sensors installed on the pipeline, at relative distances of tens of kilometers (Figure 1). The acoustic and elastic waves produced for example by third party interference and by flow variations (leaks, spills, valve regulations, pig operations, etc.), propagate along the pipeline, and they are recorded at the monitoring stations.
The propagation parameters thus have a significant effect on measurements and here lies the importance of wave propagation theory.
Sensors and GPS signals are acquired in each local unit and local units are connected to a control unit that executes the multichannel processing, enabling the detection, localization and classification of the triggering event, but also to gain useful information on the pipeline system through advanced processing.
The e-vpms® system has been installed on both oil and gas transportation lines during several field campaigns.

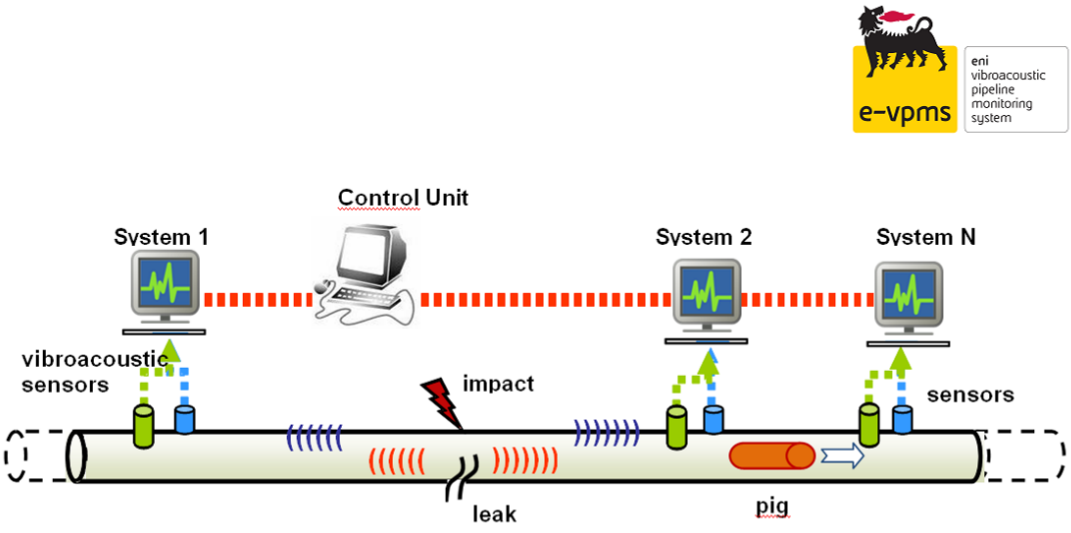

Figure 1. e-vpms® vibroacoustic monitoring system.

In the following chapters I will show some interesting experimental results obtained on different oil and gas pipelines:

- Gran San Bernardo, oil pipeline. Chivasso-Aosta (Italy) stretch;

- TRANSMED natural gas pipelines. Cap-Bon (Tunisia) - Mazara del Vallo (Italy);
- Passo Spluga air filled decommissioned pipeline. Stretch between Milano and Lecco (North Italy);
- Centro Studi Materiali (CSM) natural gas test pipeline. Full scale lab in Sardinia;
- Messina Channel offshore natural gas pipelines.

The field test campaigns have permitted to:

- derive and validate mathematical models of sound propagation within pipes;
- tune and realize a detection system for leaks and TPI (third party interference);
- track PIGs (pipeline inspection gauges) both in low pressure and high pressure scenarios;
- characterize the pipeline as equivalent acoustic transmission channel;
- apply long term monitoring of pipe for analysis of the transport efficiency, detection of anomalies such as deformations/obstructions and identification of fluid properties.

Throughout the development of Dionisio research project, I have been co-author of confidential documents delivered to eni, which contain much information on the field campaigns, device installation, measurements, data processing and interpretation.
These documents are listed in the Bibliography and are consultable upon agreement by eni.

5. Gran San Bernardo pipeline

This chapter deals with some experimental campaigns and consequent results performed on the Gran San Bernardo oil pipeline, Chivasso-Aosta stretch. Here a leak detection system was tuned, developed, deployed and validated through campaigns of controlled spills.
Measurements have been collected since 2010 which allow long term advanced data analysis, such as monitoring of pipeline operational conditions or pumps efficiency.
Thanks to measurements performed for a long time at two monitoring stations on this pipeline, the acoustic wave attenuation was reliably measured in a buried pipeline in service condition, showing the importance of the surrounding medium effect and thus validating AXSYM-3L model described in chapter 3.
Some of these results were published in [24], [25], [26] and [27].

5.1. Pipeline and monitoring system description

A vibro-acoustic monitoring system has been installed on the oil transportation pipeline in service in the North of Italy, managed by eni r&m, connecting Chivasso to Pollein (Aosta), about 100 km long (Figure 5.1). Pipe diameter is 16", oil pressure varies between 70 bars at the pumping station (Chivasso) down to 4 bars at the receiving terminal (Pollein). Flow rate is about 400 m^3/h. Two vibro-acoustic monitoring stations are located at the pipe ends (Chivasso and Pollein), and two along the pipeline (VM28 and VM35), at an intermediate distance of about 30 km. During some of the field campaigns 3 further temporary monitoring stations were installed on V19, V20 and V21. Recorded signals are vibrations of the pipe shell measured by accelerometers, and pressure within the fluid measured by two different hydrophone to obtain both the low-frequency signal (the background fluid pressure) and the higher frequency signal, namely acoustic pressure produced by travelling waves. Figure 5.2 shows the hydrophones mounted and the prototypal monitoring system at Chivasso station. Table 5.1 describes all valve stations along the considered pipeline stretch providing additional geometrical and flow parameters.
Reference [26] was published in 2010 after that the prototypal version of this system was installed and the first field test campaign was performed in a controlled scenario by producing artificially TPI and leaks.

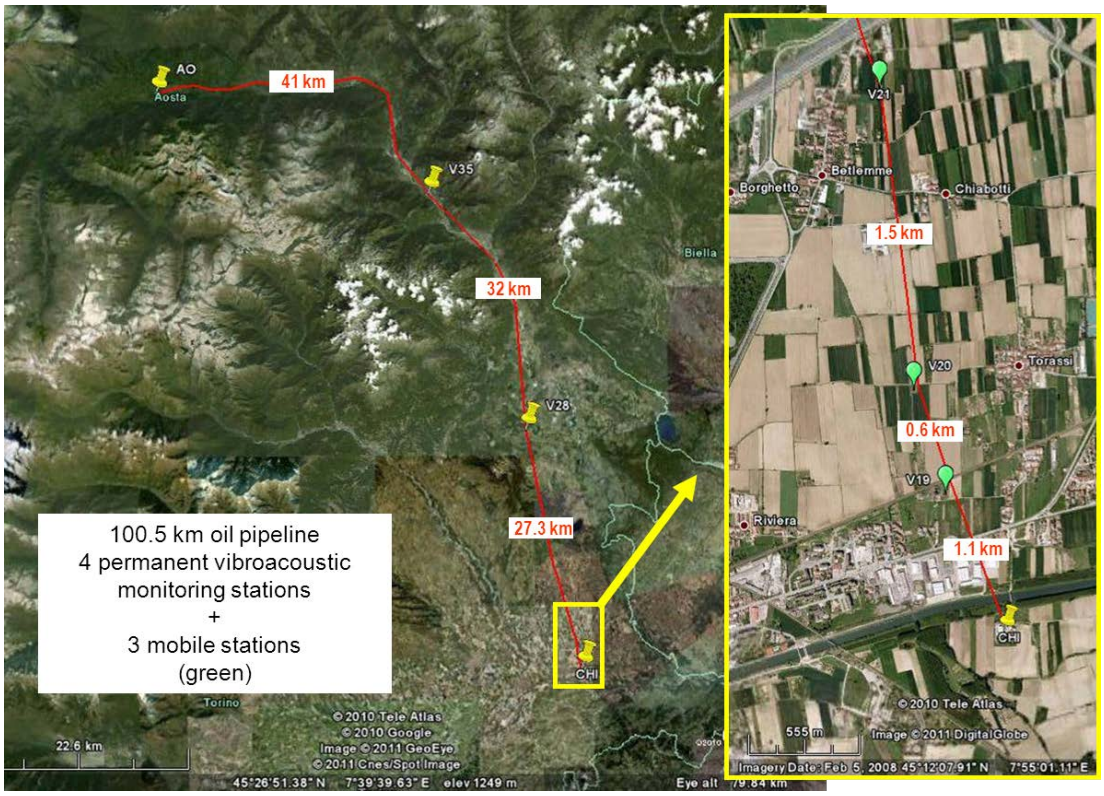

Figure 5.1. Satellite map showing oil pipeline route (red line) and measurement stations (yellow dots) on the Chivasso-Pollein (Aosta) pipeline stretch. Three temporary measurements stations are in green.

Figure 5.2. Pressure sensors (left) and prototypal monitoring system (right)

Valve VM	Place	Latitude	Longitude	Height m	Length m	Partial len m	DN inch	DN int mm	Thick mm	Vol m3	Partial vol m3
213	Chivasso	N 45 11.507'	E 7 55.218'	181	0.00	0.00	16"	384.20	11.10	0.00	0.00
19	Castelrosso	N 45 11.865'	E 7 54.996'	187	1102.55	1102.55	16"	384.20	11.10	127.82	127.82
20	Torassi	N 45 12.169'	E 7 54.888'	191	1664.49	561.94	16"	384.20	11.10	192.97	65.15
21	Betlemme	N 45 12.972	E 7 54.786'	193	3165.48	1500.99	16"	384.20	11.10	366.98	174.01
22	Betlemme	N 45 13.456	E 7 54.730'	202	4137.01	971.53	16"	384.20	11.10	479.61	112.63
23R	Boschetto				5714.71	1577.70	16"	384.20	11.10	662.52	182.91
24R	Vallo				9157.26	3442.55	16"	384.20	11.10	1061.63	399.10
25	Arè	N 45 16.908'	E 7 53.181'	253	11007.04	1849.78	16"	384.20	11.10	1276.07	214.45
26	Rodallo	N 45 17.254'	E 7 52.974'	257	11699.62	692.58	16"	384.20	11.10	1356.37	80.29
27R	Barone				15208.32	3508.70	16"	384.20	11.10	1763.14	406.77
28	Chiusella	N 45 24.983'	E 7 50.757'	238	27378.68	12170.36	16"	384.20	11.10	3174.08	1410.94
29R	Fiorano				33085.99	5707.31	16"	384.20	11.10	3835.75	661.66
30R	Lessolo				36918.32	3832.33	16"	384.20	11.10	4280.04	444.29
31	Tavagnasco	N 45 32.303'	E 7 49.910'	260	42330.42	5412.10	16"	384.20	11.10	4907.48	627.44
32	Tavagnasco	N 45 32.493'	E 7 49.983'	277	42719.71	389.29	16"	384.20	11.10	4952.61	45.13
33	Quincinetto	N 45 34.477'	E 7 48.454	289	47582.47	4862.76	16"	384.20	11.10	5516.36	563.75
34	Quincinetto	N 45 34.697'	E 7 48.157'	290	48181.04	598.57	16"	384.20	11.10	5585.75	69.39
35	Arnad	N 45 38.326'	E 7 43.008'	357	59307.04	11126.00	16"	384.20	11.10	6875.62	1289.87
36	Arnad	N 45 38.528'	E 7 42.989'	362	59755.17	448.13	16"	384.20	11.10	6927.57	51.95
37	Arnad	N 45 38.876'	E 7 42.438'	372	60740.27	985.10	16"	384.20	11.10	7041.78	114.21
38	Verres	N 45 40.536'	E 7 40.561'	379	65341.02	4600.75	16"	384.20	11.10	7575.16	533.38
39	Issogne	N 45 40.673'	E 7 40.414'	348	65727.53	386.51	16"	384.20	11.10	7619.96	44.81
Connection	Champdepraz				67943.96	2216.43	16"	384.20	11.10	7876.92	256.96
40	St. Vincent	N 45 44.396'	E 7 39.361'	580	73821.87	5877.91	16"	384.20	11.10	8558.36	681.44
41	St. Vincent	N 45 44.470'	E 7 38.827'	471	74694.74	872.87	16"	384.20	11.10	8659.56	101.19
42	Fenis	N 45 44.351'	E 7 28.705'	500	89580.17	14885.43	16"	384.20	11.10	10385.26	1725.71
43	Nus	N 45 44.298'	E 7 28.153'	520	90388.28	808.11	16"	384.20	11.10	10478.95	93.69
43bis	Nus				91242.62	854.34	16"	384.20	11.10	10578.00	99.05
44	St. Marcel				92061.67	819.05	16"	384.20	11.10	10672.95	94.95
45	St. Marcel				92452.66	390.99	16"	384.20	11.10	10718.28	45.33
301	Pollein	N 45 43.948'	E 7 21.074'	558	100485.57	8032.91	16"	384.20	11.10	11649.55	931.28

Table 5.1. Stations along Chivasso-Aosta oil pipeline.

5.2. Leak detection system

After campaigns of tests and tuning, we have deployed a leak detection system on the Chivasso-Pollein stretch of the oil pipeline which relies on measurements performed on 4 stations: Chivasso, V28, V35 and Pollein.

The detection and localization is run on the control unit computer for each intermediate pipe stretch, by processing the pressure signals collected at both adjacent stations. Since interruption of flow produces interruption of the pipeline acoustic channel (because of closure of non-return valves) and pressure decrease, background pressure signal can be used to switch on/off the detection procedure.

The acoustic response of every pipe stretch is computed and updated with a time interval of some minutes, exploiting the pump noise produced at pumping stations as travelling signal.

Signals measured at both ends of a stretch are filtered and back-propagated using the time varying acoustic response, and then they are correlated in short time windows (few seconds) at discrete positions (every 20-100 m) along the pipeline stretch: the result is an image-like representation of correlation values versus distance (pipeline coordinate) and time axis. Anomalies appear as high amplitude events (outliers with respect to average values): the alarm threshold has to be tuned during a calibration stage, and it can be adaptively updated during standard pipeline operation.

The following sections describe the leak detection and localization procedure which was tuned, tested, implemented and validated on the Chivasso-Pollein oil pipeline.

5.2.1. Estimation of acoustic response

The response of the acoustic channel can be experimentally measured using the pressure transients produced at the pumping terminals as source signal. Referring to Figure 5.3, let $s_0(t)$ be the source signal, $x_B(t)$ and $x_C(t)$ the pressure signals recorded at station B and C, $h_{BC}(t)$ the (possibly time varying) acoustic response for sound propagation from B to C. The leak detection system computes all the responses between pair of stations using adaptive filter theory, in particular with a Widrow-Hoff algorithm.

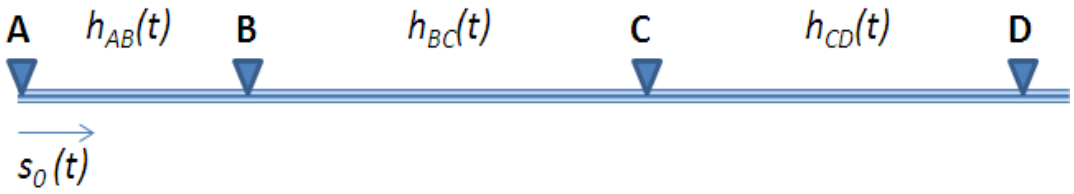

Figure 5.3. Scheme for estimation of response of the acoustic channel . Recording stations in A, B, C, D, pump noise $s_0(t)$.

Considering the sampled version of the signals, the Widrow Hoff algorithm for a *N*-th order filter can be summarized as [28]

$$\mathbf{x}_B(n) = [x_B(n), x_B(n-1), \ldots, x_B(n-N+1)]^T$$

$$e(n) = x_C(n) - \hat{\mathbf{h}}_{BC}^T(n)\,\mathbf{x}_B(n)$$

$$\hat{\mathbf{h}}_{BC}(n+1) = \hat{\mathbf{h}}_{BC}(n) + \gamma\, e(n)\,\mathbf{x}_B(n)$$

for $n=1,2,3,\ldots,N$ and with γ= step size, initialization $\hat{\mathbf{h}}_{BC}(0) = [0,0,0,\ldots 0]$

Given the stationarity of the flow process, the filter becomes stable after some tens of seconds, and it is updated with a time interval of some minutes.
The filter obtained in this way represents an experimental sample of the propagation function from B to C and therefore the experimental propagation parameters (at least at low frequency) can be extracted and compared with the propagation models of Part I.

5.2.2. Leak detection algorithm

The complete leak detection algorithm can be divided in two steps:

Step 1: Noise reduction (Figure 5.4)

– Estimate of acoustic channel response: compute transfer functions between couples of stations (using pump/valve noise)
– From segment T_1-A: compute right-going noise generated at T_1
– From segment T_2-B: compute left-going noise generated at T_2
– Remove noise from A and B after propagation with previously computed transfer functions

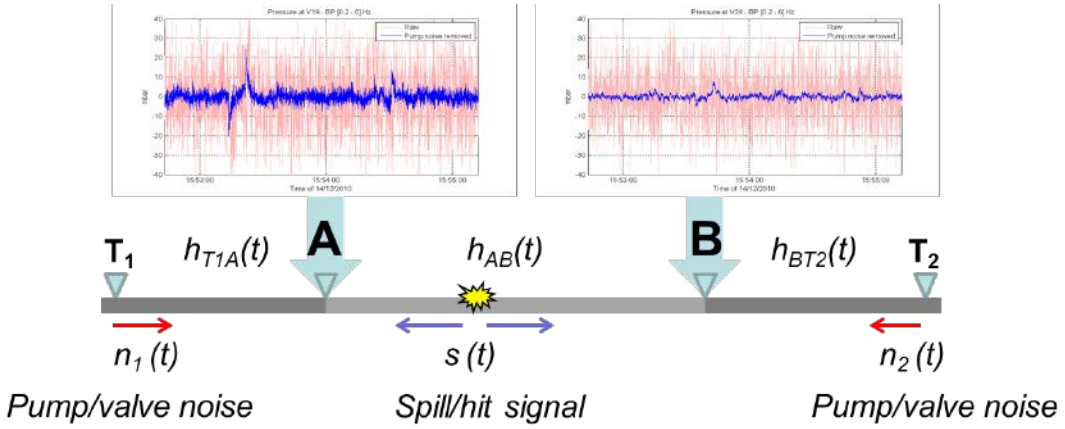

Figure 5.4. Reduction of pump noise from monitoring stations A and B.

Step 2: leak detection (Figure 5.5)

– Back propagate signal A to signal B and vice-versa and cross-correlate pressure signals
– Detect peaks on cross-correlation matrix.

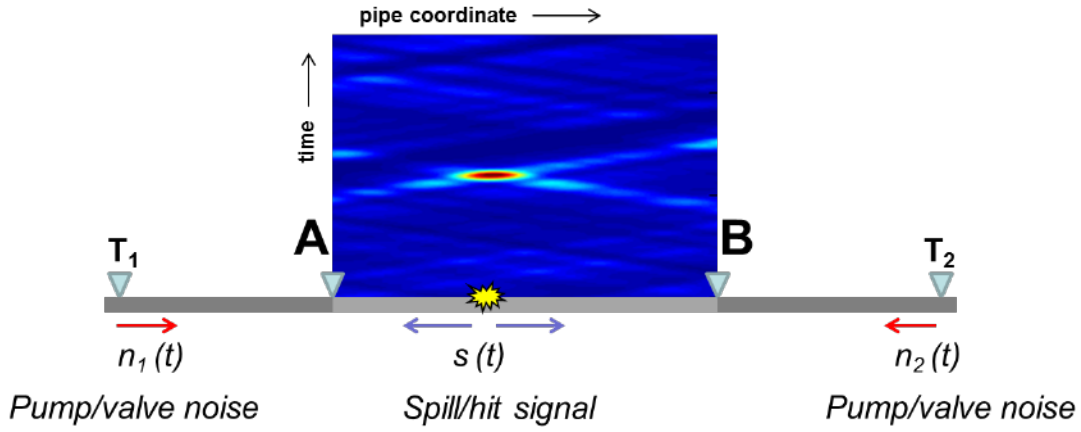

Figure 5.5. Detection of leaks occurred between stations A and B

I have contributed to establish and implement these leak detection procedures which have been tuned in order to detect fast spills/leaks with hole >0.2".

In 2012 a validation test has been performed by generating a total of 86 spills in different conditions:

- spilling diameter from 0.06 to 0.49 inches;
- spill locations at VM22, VM31 and VM33;
- fast & slow spill opening/closing.

The expected behavior of the e-vpms® has been successfully confirmed.
The calibrated system shows excellent performances in terms of false alarms (reduced to 0% in the monitored period at the expense of possible missing detection for spills minor of 0.2" diameters).
The e-vpms® installation with leak detection system on GSB oil pipeline has been kept fully operational. No alarms of real leaks have been issued so far.

5.3. Advanced processing

Beyond the leak detection system, e-vpms® technology allows also to store a large amount of data which, properly processed, can provide additional important information on the pipeline and the carried fluids such as flow efficiency, pipe integrity, fluid physical properties, malfunctioning of mechanical devices. The availability of data measured for a long time in fact, allows to learn the usual, standard operational conditions and easily identify different measurements that result from anomalous situations.
This section shows examples of such advanced processing:

1) Long-term measurements of acoustic wave attenuation up to 200 Hz and comparison with theoretical models.
2) Long-term monitoring of sound speed and comparison with theoretical models.
3) Long-term monitoring of attenuation/sound-speed relation and comparison with theoretical models
4) Pump noise listening and failure detection.
5) Long-term monitoring of anomalous reflectors.

5.3.1. Acoustic wave attenuation

The curve of the acoustic wave attenuation in the oil pipeline is here computed up to a frequency of 200 Hz and compared with theoretical models of Part I of this thesis.
The attenuation is computed by measuring the same travelling pressure signal at two monitoring stations, the travelling signal considered is the noise of the pumps which is produced at Chivasso pumping station and travels towards Pollein (Aosta): such noise indeed appears to correlate very well between all couples of stations from Chivasso to VM28, meaning that all hydrophones record the same signal that is travelling in the pipe.

In order to estimate the attenuation curve up to high frequency I consider a couple of stations at short distance which is Chivasso-VM21 (distance 3165 m). As an example let's consider ten minutes of signal, starting at December 14th 2010, 15:10 (GMT time): Figure 5.6 shows the signals (only 10 seconds for clarity) recorded by hydrophones at the two stations and the power spectral density (PSD) computed on 10 minutes, Figure 5.7 displays the cross-correlation between the signals.
Figure 5.6 shows how PSD of V21 signal lays down to the sensor sensitivity limit little above 200 Hz, which gives the frequency limit of validity of the attenuation curve.

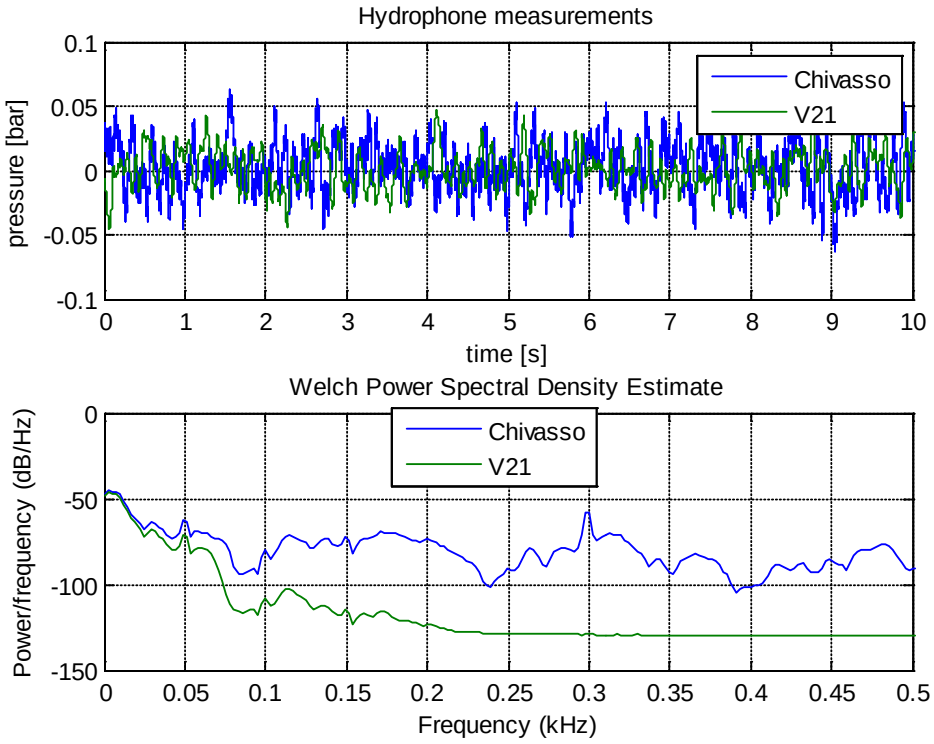

Figure 5.6. Acoustic pressure at Chivasso and VM21. Time signal (top), power spectral density (bottom).

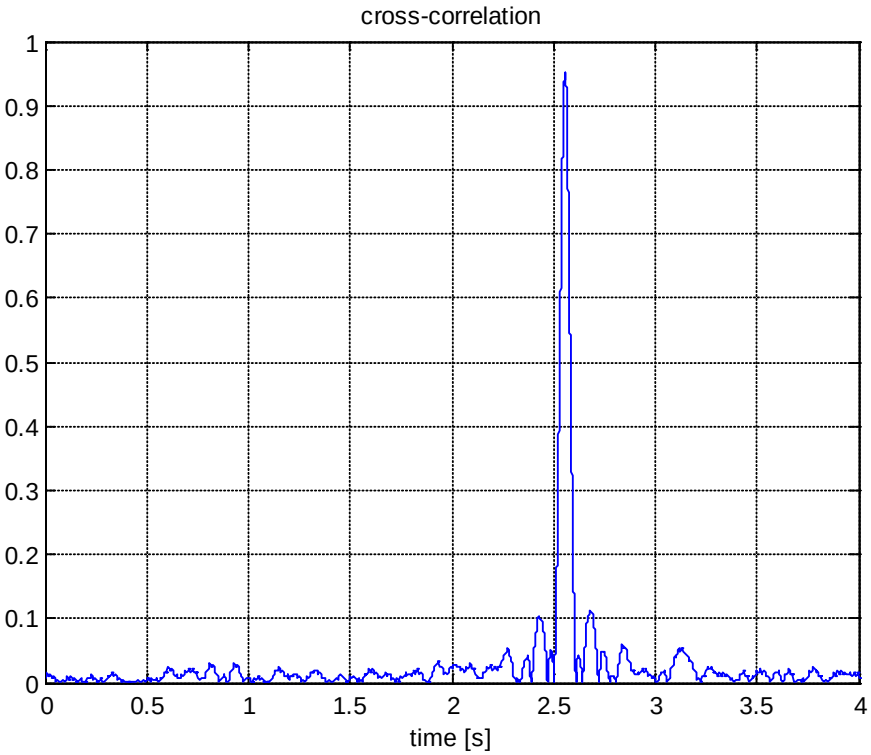

Figure 5.7. Propagation from Chivasso to VM21. Cross-correlation of pressure signals.

The high value of the cross-correlation peak clearly shows that the 2 receivers are measuring mostly the same signal travelling along the pipeline. From the delay of the cross-correlation peak, a rough estimate of the average wave-speed is possible, yielding 1238 m/s for the Chivasso-VM21 propagation.
The difference between the power spectral densities (in dB) divided by the distance (in km) gives a measure of the attenuation (in dB/km).

For a more reliable dataset of experimental data, the procedure just described was applied to periods of some minutes in different days over more than two years. The periods chosen were dependent on the availability of data and the working condition of the line. The curves are displayed in Figure 5.8 and the dates of measurements are written in legend, from December 2010 to January 2013.

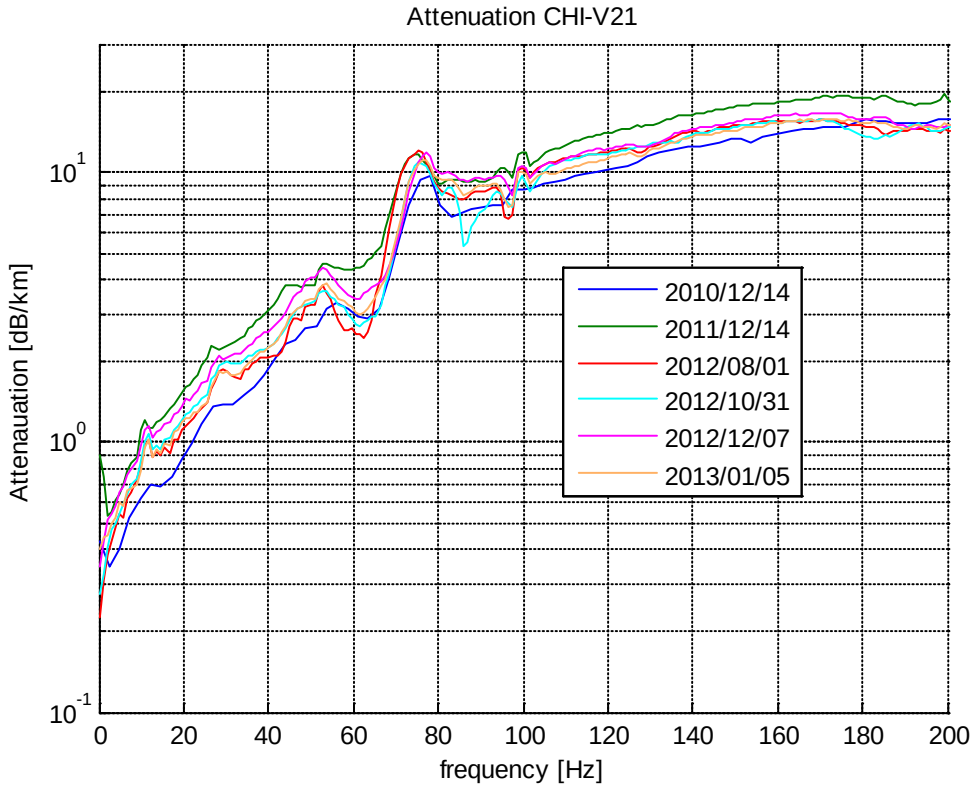

Figure 5.8. Experimental wave attenuation

Given the similarity of the curves, the measurements are quite repeatable, which implies that they are also reliable and can be used to validate the wave propagation models; the oscillations in the curves (in particular at about 80 Hz in the blue curve) are likely related to resonance effects in the measuring points.

In order to compute the attenuation curves with some propagation models, it would be useful to know the correct physical parameters of the pumped oil and the elastic parameters of the soil surrounding the pipe.
In practice the oil changes its composition and the variable pressure would add uncertainties as well, moreover the soil is likely to change its properties all along 3 km too, so that a data driven approach is here preferred to get the values of models parameters. The values in Table 2.1 are still a good first guess.
Such inversion procedure is performed on the new model AXSYM-3L which is expected to be the most comprehensive among the presented models in chapters 2 and 3.
In fact I have found a set of parameter values, Table 5.2, not so different from those of Table 2.1, for which a good fitting, at least up to 140 Hz, is displayed (Figure 5.9).

Physical and geometrical parameters			
Symbol	Value	Unit	Description
Pipe geometry			
b	0.2	m	Pipe internal radius
h	0.0111	m	Pipe thickness
Internal fluid – Oil			
ρ_f	850	kg/m^3	Density
c_f	1350	m/s	Speed of sound in free medium
B_f	1.8x10^9	Pa	Bulk modulus (function of ρ_f and c_f)
η	1.2x10^{-2}	Pas	Dynamic viscosity
γ	1	-	Specific heats ratio
Pr	Not used	-	Prandtl number
Shell material – Steel			
ρ_p	7800	kg/m^3	Density
E	2x10^{11}	Pa	Young modulus
χ	0	-	Loss factor
ν	0.3	-	Poisson ratio
Surrounding medium – soil			
ρ_m	1400	kg/m^3	Density
c_p	1200	m/s	P-wave speed
c_s	850	m/s	S-wave speed

Table 5.2. Geometrical and media parameters

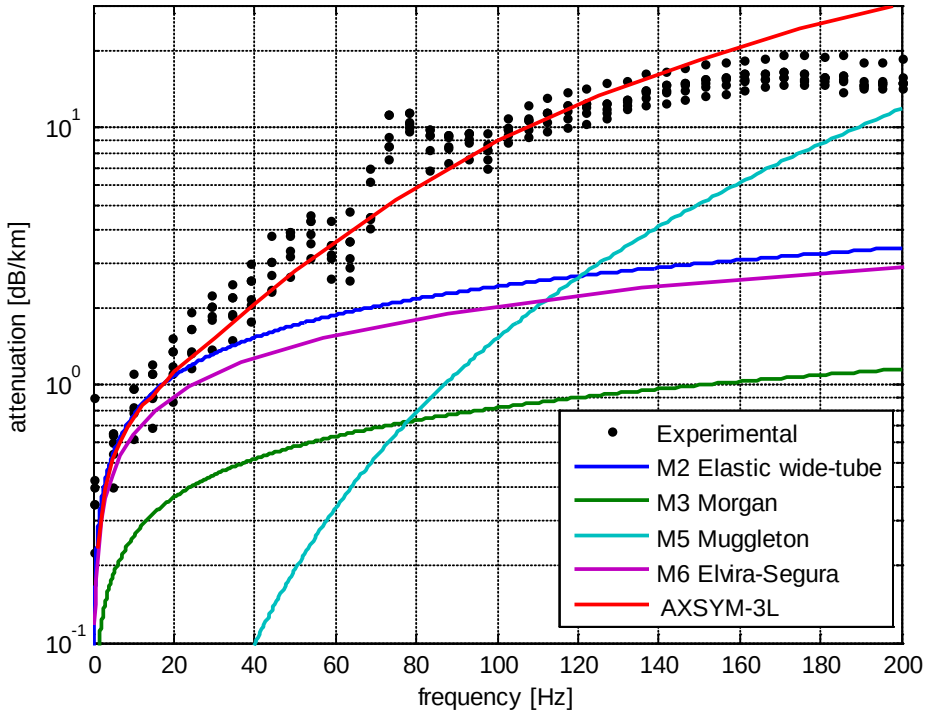

Figure 5.9. Attenuation curves measured and computed by models

As expected the AXSYM-3L model fits best the experimental attenuation curve, it just diverges gradually from it starting at 120 Hz; this might be due to inaccurate measurements because of low energy at such high frequency, where in fact the PSD of VM21 receiver approaches the plateau.

Analogous measurements of phase velocity can be done, but the values of phase velocity are very sensitive to the fluid speed of sound and therefore to the type of oil carried during measurements which often varies during pipeline exercise, like one can see in the next section.
Therefore it would be impossible to validate the propagation model as regards the phase velocity without knowing the particular sound speed of the conveyed crude oil. For completeness however the corresponding dispersion curves are shown in Figure 5.10, except for Model 3 (Morgan) whose curve would lay far outside the figure.

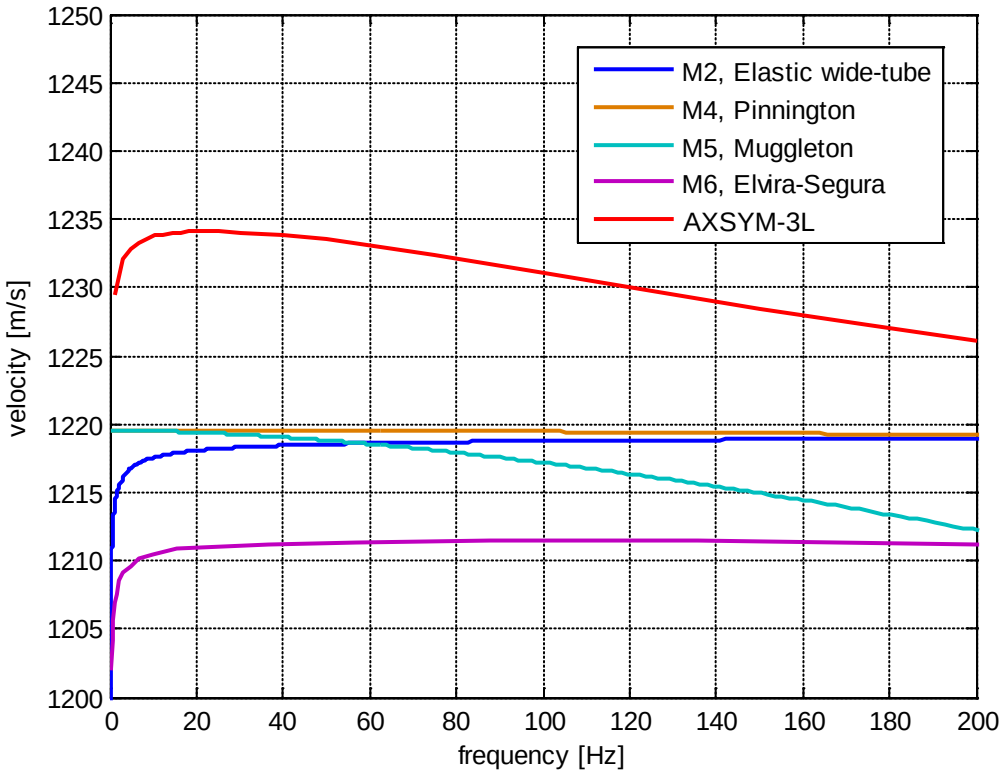

Figure 5.10. Dispersion curves computed by models

5.3.2. Speed of sound of conveyed oils

Similarly to the previous section, here I compute the speed of sound along the pipeline from the measurements of acoustic pressure signals travelling along the line. This time, three couples of subsequent stations are considered at once:

- Stretch 1: Chivasso-V28
- Stretch 2: V28-V35
- Stretch 3: V35-Pollein

Figure 5.11 reminds their position on the line

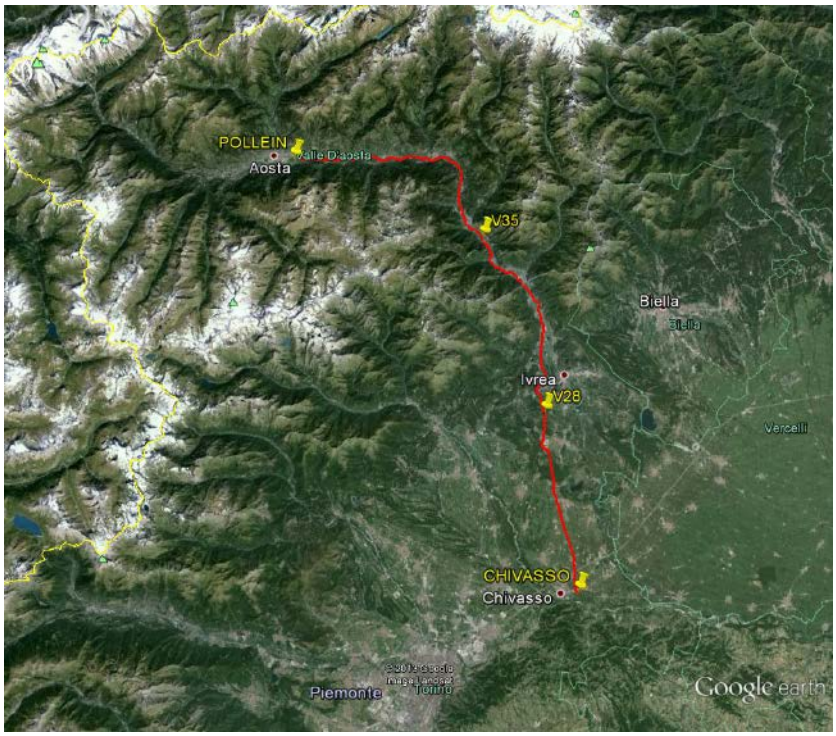

Figure 5.11. Monitoring stations along Chivasso-Aosta pipeline.

The data here considered span a six month interval of year 2011, during which the pipeline has transported oils whose properties are within the ranges reported in Table 5.3.

Symbol	**Min value**	**Max value**	**Unit**	**Property**
ρ_f	750	850	kg/m^3	Density
η	2	20	cP	Dynamic viscosity

Table 5.3. Oil properties in GSB pipeline.

I obtain the travel-times of pressure waves along each pipeline stretch by searching the maximum of the cross-correlation between pressure signals recorded at the delimiting stations.
These travel-times are computed every minute. Given the fixed length of the pipe stretches, I then obtain the sound velocity within the oil: Figure 5.12 is the result, gaps in the curves correspond to absence of flow (pipeline at rest).
Sound velocity differences between the stretches are consistent with the different background pressures. Sound velocity variation along time is an indicator of changing fluid (oil).

From these time series I create a two-dimensional speed/pressure histogram with pressure bins of 125 mbar and velocity bins of 1.5 m/s. The histogram displays, over the whole investigated interval, the number of operational minutes falling within each bin. Figure 5.12 (right) displays such histogram for stretch 1.
It is interesting to notice a clusterization of the measured values mainly in three operational status (A, B and C), that I relate to the three different oil types.
Table 5.4 collects the average numerical values of the sound speed associated to the 3 oils in each of the 3 stretches, characterized by a typical background pressure.

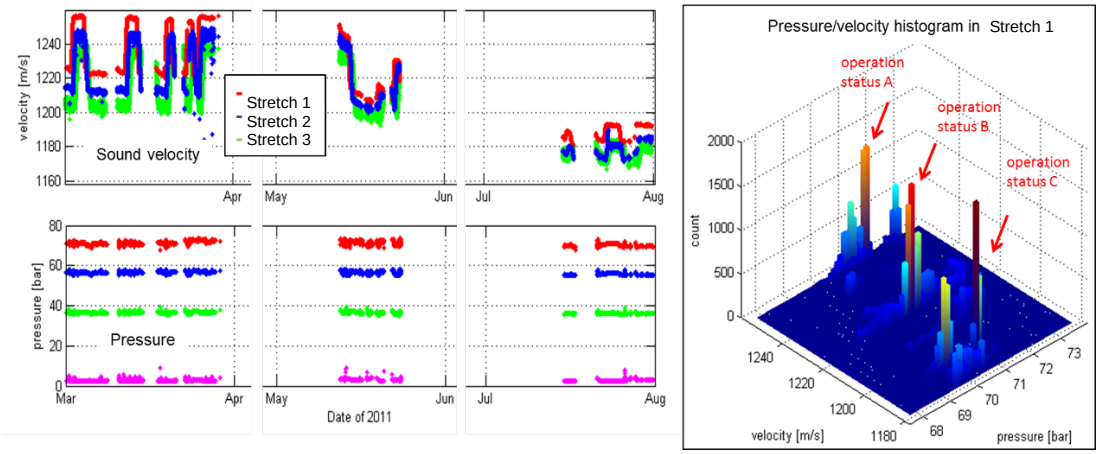

Figure 5.12. Sound speed (top left) and pressure (bottom left) within the oil in the different pipe sections. Pressure/speed histogram in the first stretch (right)

Pipeline stretch	Stretch length [km]	Avg. pressure [bar]	OIL A sound speed [m/s]	OIL B sound speed [m/s]	OIL C sound speed [m/s]
Stretch 1	27.3	63	1256	1223	1193
Stretch 2	32	46	1245	1213	1181
Stretch 3	41	17	1236	1203	1174

Table 5.4. Measured sound speed and background pressure.

With the aim of comparing the measured sound-speed with the theoretical one, I obtain the oil free medium sound speed c_f from the experimental in-pipe velocity c by inverting the equation (2.1), which is here simplified (with unitary correction factor ε):

$$c = \frac{c_f}{\sqrt{1+\frac{B2b}{Eh}}} \tag{5.1}$$

where

b: pipe internal radius;
B: oil bulk modulus;
E: pipe Young modulus;
h: pipe thickness.

Then, I compute the theoretical sound-speed c_f with the Batzle and Wang model [29] for dead oil at 15°C,

$$c_f = 15450 \cdot (77.1 + API)^{-0.5} - 3.7 \cdot T + 4.64 \cdot P + 0.0115 \cdot (0.36 \cdot API^{0.5} - 1) \cdot T \cdot P \qquad (5.2)$$

where
API: oil grade;
P: pressure [MPa];
T: temperature [°C];
c_f is expressed in m/s.

The oil grade is a function of density, I have chosen one value of density for each of the 3 oils: 750, 800, 850 kg/m^3. The resulting curves are displayed in Figure 5.13 together with the experimental results: the agreement is very good.

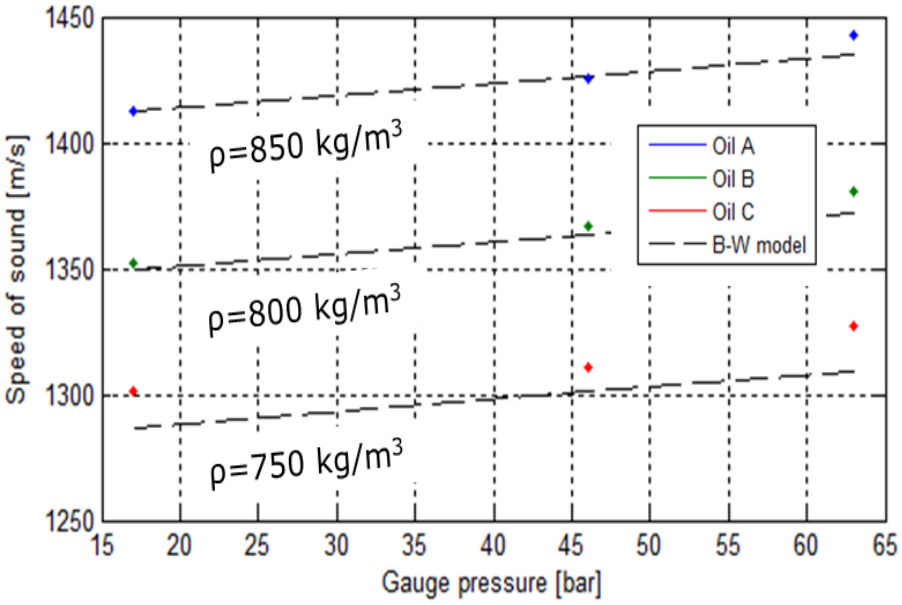

Figure 5.13. Pressure - sound speed relation. Experimental data (dots) and Batzle and Wang (B-W) model [29].

This shows how the measured speed of sound can be related to oil physical properties such as their density and therefore allow to discern the type of oil conveyed.

5.3.3. Attenuation - Sound speed diagram

Here I show an advanced processing that allows to clearly distinguish between two pipeline conditions: before and after operations of maintenance.
The sound speed and the attenuation at low frequency are together measured in order to obtain long-term statistics and compare them with theoretical reference values.
At low frequency (<15 Hz) the attenuation coefficient α can be approximately computed with the simple wide-tube approximation, even neglecting thermal terms, as a function of signal angular frequency ω, oil viscosity η, pipe radius b and sound speed c:

$$\alpha = \frac{1}{b}\sqrt{\frac{\omega\eta}{2\rho c^2}} \tag{5.3}$$

The important unknown parameter in this formula is the viscosity. There are several literature models that relate the viscosity μ with the oil temperature T and *API* density. I use here three of them:

- Model 1 (Labedi [30], original coefficients):

$$\ln\eta = a_1 + a_2 \ln API + a_3 \ln T \tag{5.4}$$

- Model 2 (Glaso [31], original coefficients):

$$\ln\eta = a_1 + a_2 \ln T + +a_3 \ln(\ln API) + a_4 \ln T \ln(\ln API) \tag{5.5}$$

- Model 3 (Beggs and Robinson [32], Canadian oils coefficients):

$$\ln(\ln(\eta + 1)) = a_1 + a_2 API + a_3 \ln T \tag{5.6}$$

The constants a_i are given in the cited references.
To compute the free-medium sound-speed I use again Eq. (5.2) (Batzle and Wang [29]) and turn it into in-pipe sound-speed with Eq. (5.1).
In this way I can compute "theoretical" attenuation and sound-speed for the three models in Eqs.(5.4)-(5.6) with the parameters in Table 5.5.

Parameter	Value	Unit	Property
ρ	750-850	kg/m^3	Density
T	15	°C	Temperature
ω	2π(2-15)	rad/s	Ang. Frequency
b	20.32	cm	Internal radius
h	1.11	cm	Pipe thickness
E	2x10^{11}	Pa	Pipe elastic modulus
B	ρc_f^2	Pa	Fluid bulk modulus

Table 5.5. Model parameters for theoretical attenuation/sound-speed relation.

I have then measured the actual attenuation and sound-speed along stretch 1 of the pipeline, by comparing the pressure signals at the delimiting stations.
Figure 5.14 compares the attenuation/sound-speed relation according to the theoretical models with the experimental data measured in 2011, the blue cloud in fact represents a two dimensional histogram (darker blue means higher occurrence) that synthetizes a numerous statistic of values measured in several months in year 2011. Attenuation measured at different frequencies has been normalized by the square root of frequency so that a unique statistic collects all frequencies together.
Three sub-clouds (A, B and C) are pointed in the figure and can be associated to the same three oils mentioned in the previous section.
There is a general agreement between the shape of the curves, but experimental attenuation is higher than the predicted one for equal sound-speed. In Fig. 5.15 the same theoretical models are displayed together with an analogous statistic of experimental data measured in several months in 2012, after pipeline maintenance. In this case the measured attenuation fits the theoretical attenuation much better.
A possible explanation is that before maintenance, deposits in the line increase the wave attenuation partly because they reduce the pipe section and partly because they act as sound absorbers.
The important evidence is that after deposits removal the attenuation shifts close to the theoretical attenuation-soundspeed curve which can therefore be used as reference.
Again this demonstrates that vibro-acoustic data can be exploited for fluid characterization and monitoring of transportation efficiency.

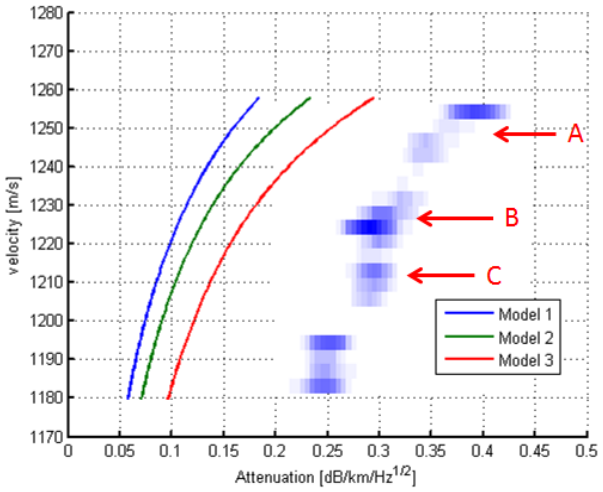

Figure 5.14. Attenuation-sound speed diagram. Theoretical models and experimental data (blue "areas"), measured in 2011.

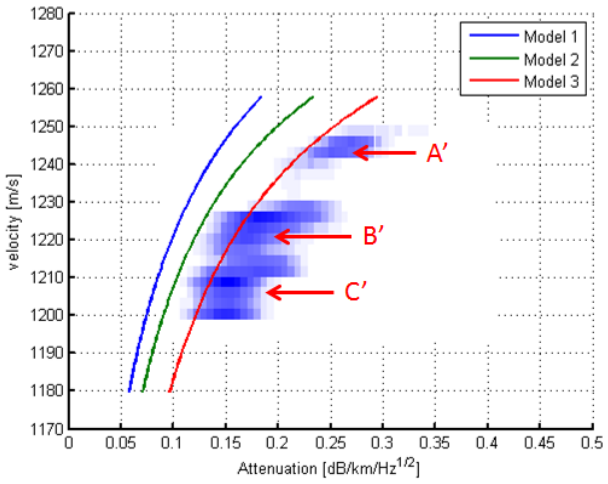

Figure 5.15. Attenuation-sound speed diagram. Theoretical models and experimental data (blue "areas"), measured in 2012.

5.3.4. Pump monitoring

Pump equipment generates vibro-acoustic signals, that can be heard in air but also within the pumped fluid. Here I compare pressure signals before and after a pump replacement at Chivasso station, due to a failure occurred on May 11th, 2012.
Figure 5.16 shows the pressure signals at the three monitoring stations closer to the pumping terminal (Chivasso, V21, V28), from 0 a.m. to 6 a.m. on May 11th, before the pump replacement: the signals show several periodic negative peaks coming from Chivasso station.

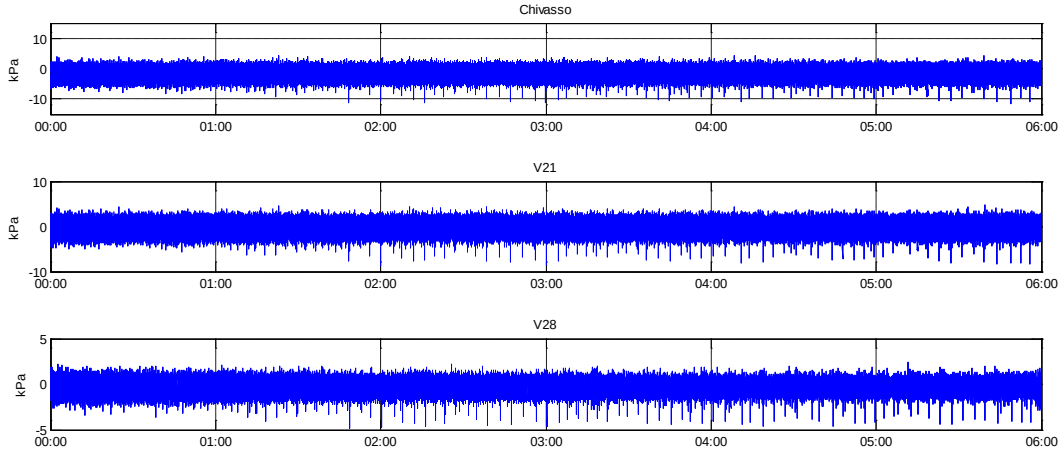

Figure 5.16. Pressure signal before pump replacement (May 11th, 2012).

Figure 5.17 shows the pressure variations at the same stations, from 0 a.m. to 6 a.m. on May 12th, after the pump replacement: the periodic peaks are not present any more.

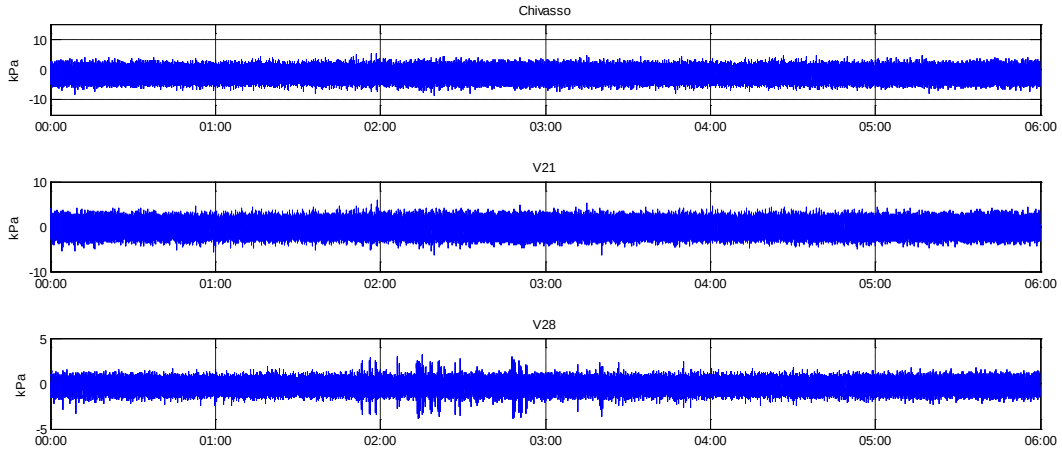

Figure 5.17. Pressure signal after pump replacement (May 12th, 2012).

It could be useful to process these time series in order to ease a system of automatic detection of the anomaly, for example to get the pressure values distribution (number of values falling in each pressure interval) or to compute the spectrogram of the pressure time series.
Figure 5.18 shows the pressure distribution of the signals before (blue) and after (red) the pump replacement, the negative tails of the distributions are noticeably reduced after pump replacement.

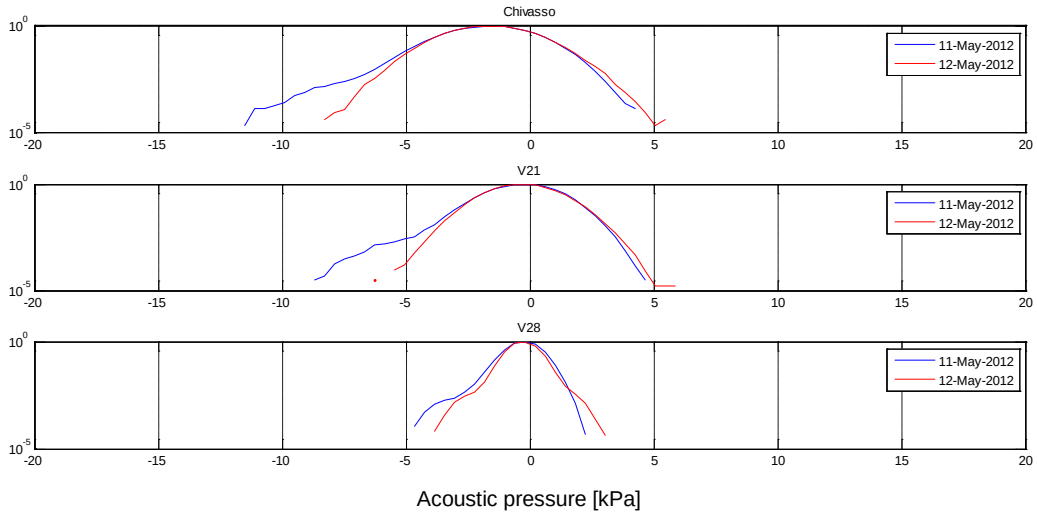

Figure 5.18. Pressure values distribution before and after pump replacement.

Figure 5.19 shows the spectrograms of Chivasso pressure signal before (top) and after (bottom) pump replacement: it is clearly apparent the different operational regime of the pump from the presence or absence of red stripes covering a wide frequency range.

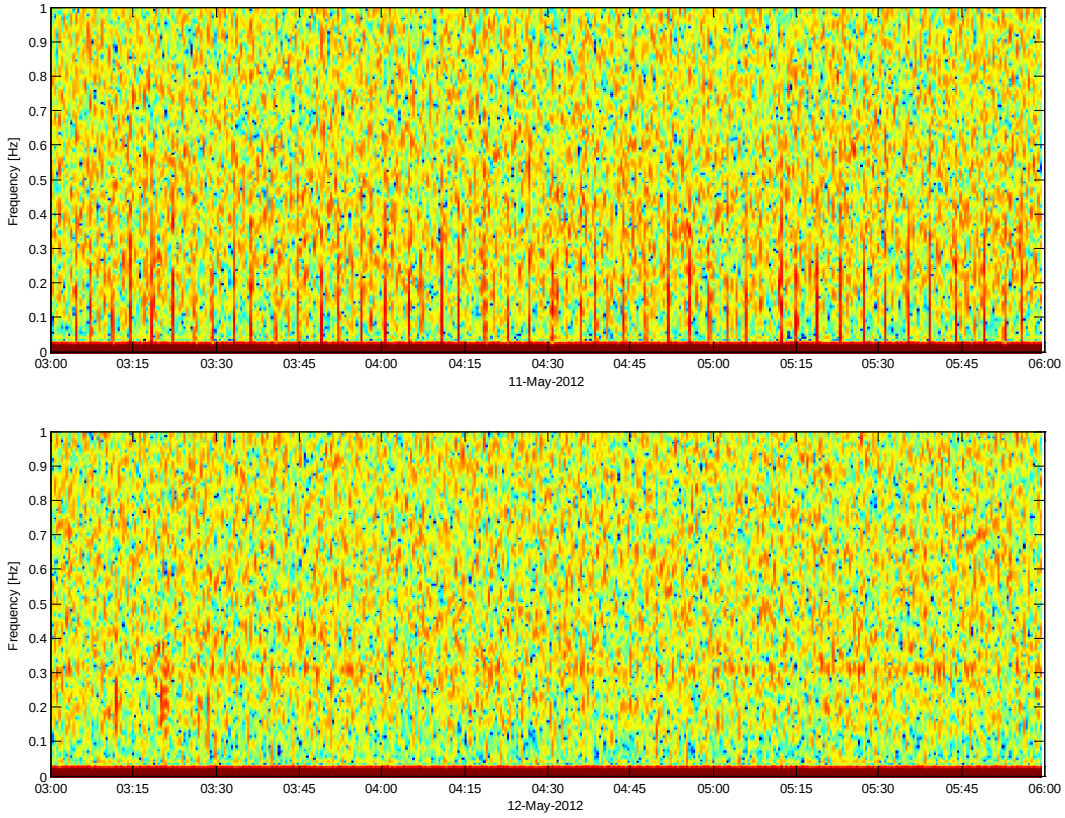

Figure 5.19. Frequency content of Chivasso pressure signal before (up) and after (bottom) pump replacement.

I can therefore conclude that e-vpms® data can help pump/valve equipment monitoring, in fact long term data analysis and training procedures can be used to define a set of normal operation parameters (e.g. maximum amplitude of acoustic pressure, signal statistical moments, typical peak frequencies), in order to detect pump equipment anomalies.

5.3.5. Detection of reflectors

The noise produced at the pumping stations travels along the pipeline and it is possibly reflected by discontinuities in the transmission waveguide. Discontinuities can be related to pipe deformations, internal occlusions, partial valve opening, etc. By measuring the pressure signal it is possible to detect and locate such reflectors: in

case they are permanent, their presence should be detected every time the pipeline is working and pump noise propagates along it.
Auto-correlations of pressure signal measured at the terminal stations are a suitable method to detect reflectors, since they look for delayed copies of the noise that departs from the station. I test this idea on the pressure data collected at the two pumping stations of Chivasso-Pollein oil pipeline.

Chivasso side

Figure 5.20 to Figure 5.24 show auto-correlations of pressure signals at Chivasso station for some time windows in December 2010, March 2011 and December 2011. Signals are band-pass filtered [1 10] Hz, and correlations are computed every hour on half an hour long signals.
Correlation is normalized to 1 and colors span the range 0-0.1.
Figures show that, except for some intervals when pumps are not working and/or valves are closed, there is a permanent echo at about 5.5 seconds. The small variation of this value is related to the variation of speed of sound in the transported oil.
Using the measured speed of sound (continuous output of standard vpms® operation), I obtain that two-way travelled distance of the echo is 6.8 km, corresponding to a reflector 3.4 km far from Chivasso station.

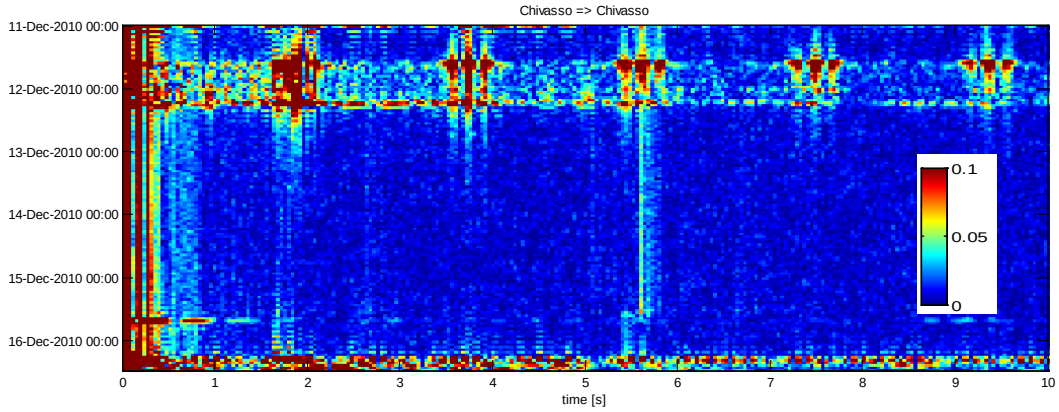

Figure 5.20. Autocorrelation of pressure signal at Chivasso station in December 2010.

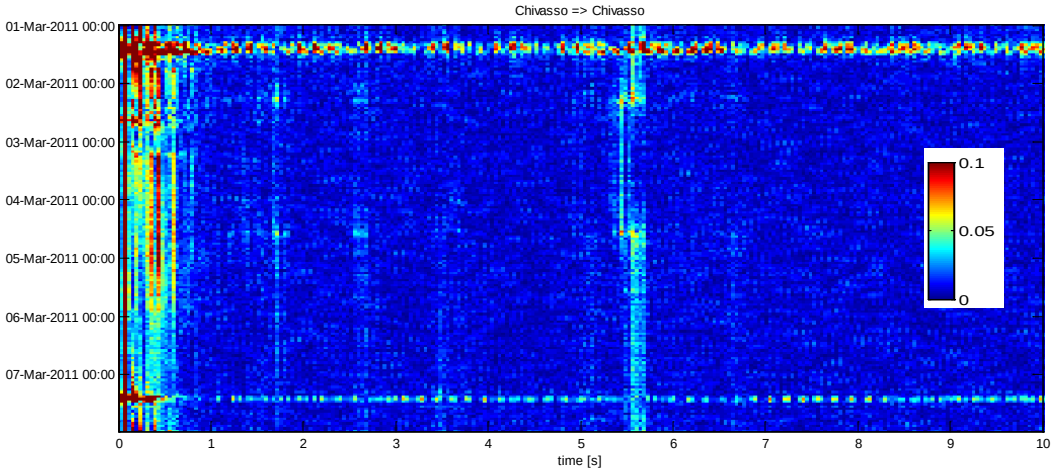

Figure 5.21. Autocorrelation of pressure signal at Chivasso station in March 2011.

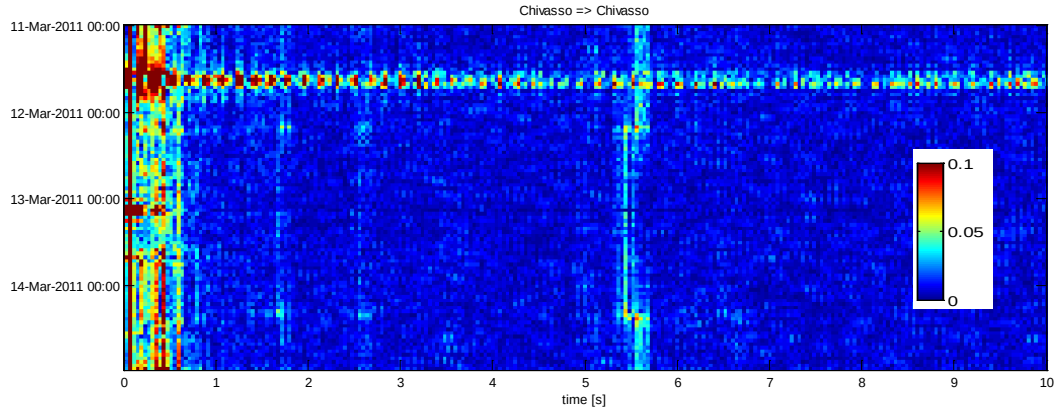

Figure 5.22. Autocorrelation of pressure signal at Chivasso station in March 2011.

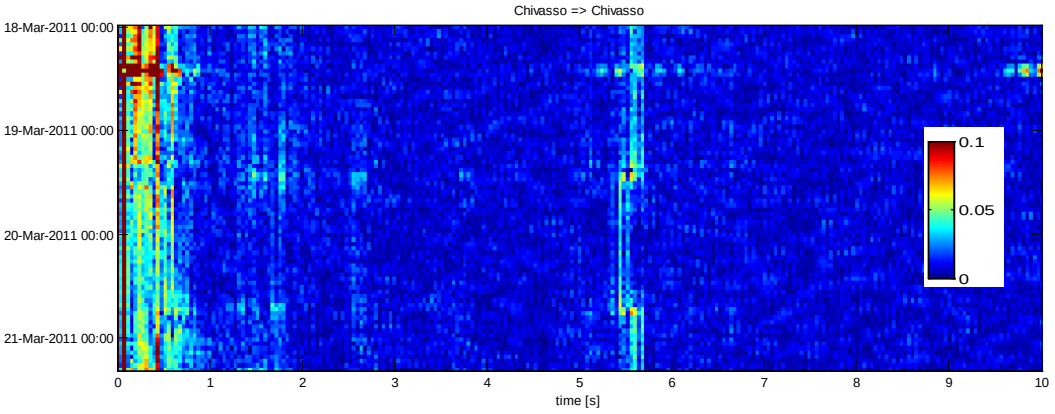

Figure 5.23. Autocorrelation of pressure signal at Chivasso station in March 2011.

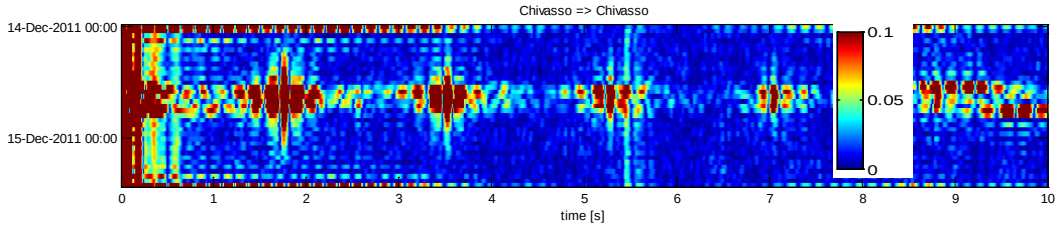

Figure 5.24. Autocorrelation of pressure at Chivasso station in December 2011.

Auto-correlation detects the distance of the reflector from Chivasso station, but it doesn't tell if it lies downstream (towards Pollein) or upstream (towards Ferrera, the preceding pumping station). In order to remove this ambiguity, I exploit the event when a fluid change is occurring within the pipe: a different oil is departing from Ferrera, and it is replacing the previous one at the flow velocity (around 1 m/s). Sound speed in the two oils is slightly different, and the autocorrelation image will show a variation in the position of the "echo". There can be these two cases:

- the reflector is located upstream if the time position of the echo changes before new oil reaches Chivasso station;
- the reflector is located downstream if the time position of the echo changes starting from when the new oil has reached Chivasso;

Figure 5.25 compares the autocorrelation of pressure variations at Chivasso (left), zoomed on the echo at around 5.5 s, with the travel-time between Chivasso and V28 (right). Autocorrelation is computed with higher resolution with respect to Figures 5.20-5.24, on 20 min time windows overlapped by 10 min, and signal is band pass filtered at [1 Hz – 40 Hz].
Chivasso-V28 travel-time shows that the front of the new faster oil passes through Chivasso on 12 March at about 4 a.m., which is the same time when the echo travel time starts decreasing. This means that the reflector is downstream to Chivasso.

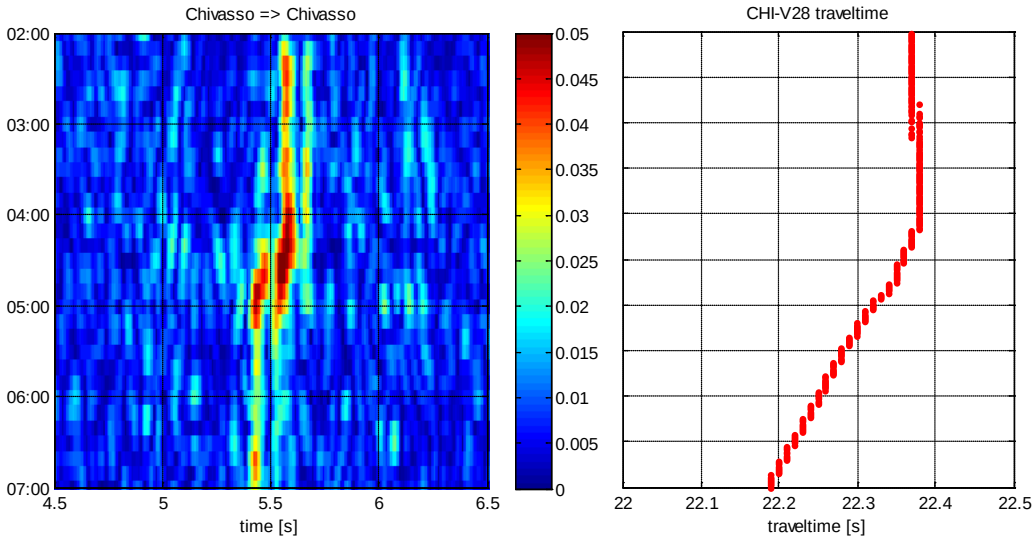

Figure 5.25. Autocorrelation of pressure signal at Chivasso station, focus on travel time shift (left). Travel time from Chivasso to V28 stations in same time interval (right).

This position is compatible with the Milano-Torino highway which is just downstream to V21 station. Figure 5.26 shows a scheme of the pipeline and Figure 5.27 is a map displaying the position of the highway.

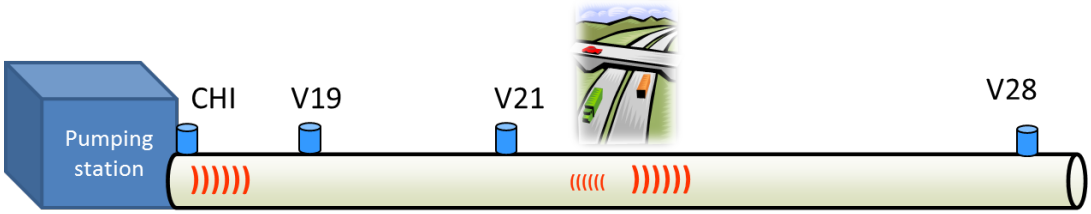

Figure 5.26. Pipeline scheme showing the position of the reflector, likely the highway.

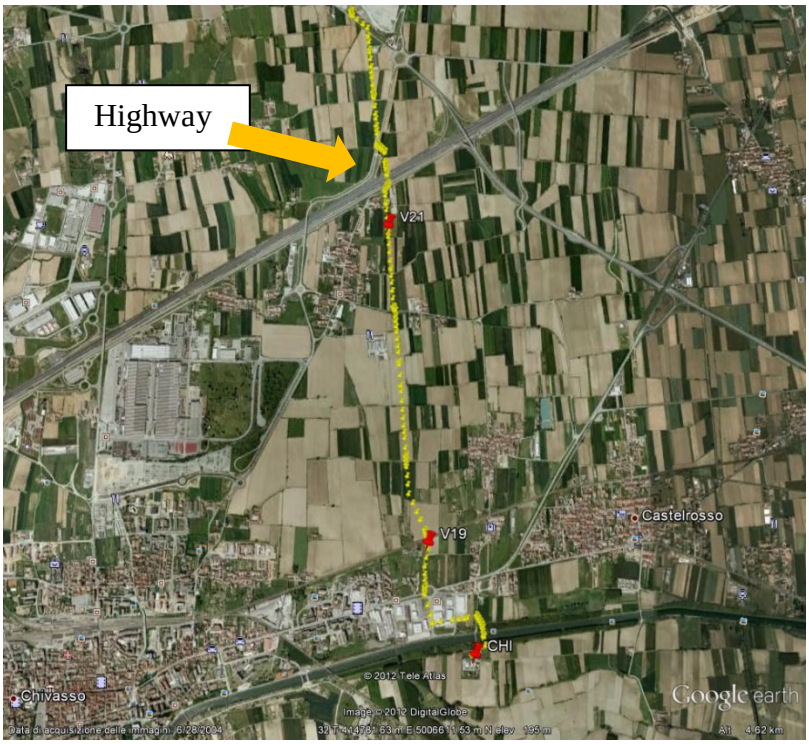

Figure 5.27. Map showing the position of the intersection between pipeline and Milano-Torino highway.

Pollein side

Auto-correlations are performed also for the Pollein station in the same time windows as Chivasso station.
In this case there is a reflection delayed by about 27 seconds, corresponding to a reflector 16 km far from Pollein station.

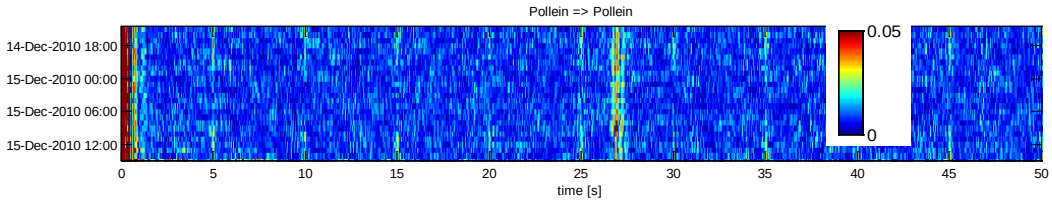

Figure 5.28. Autocorrelation of pressure signal at Pollein station in December 2010.

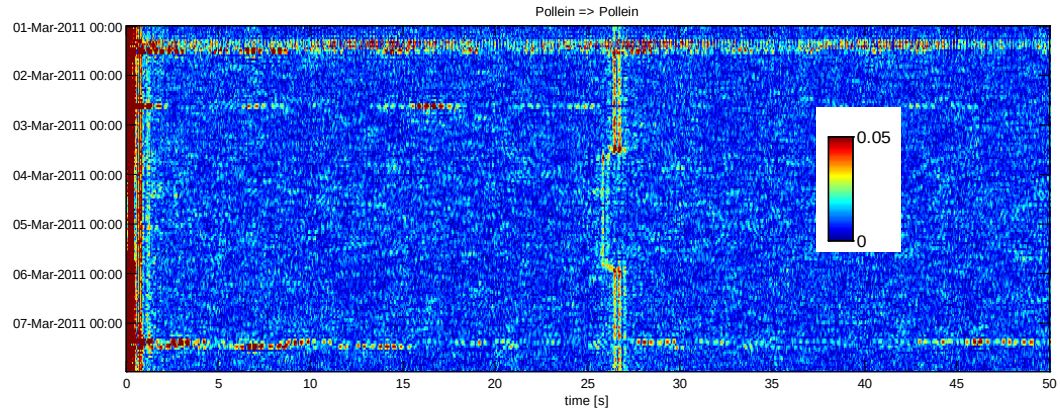

Figure 5.29. Autocorrelation of pressure signal at Pollein station in March 2011.

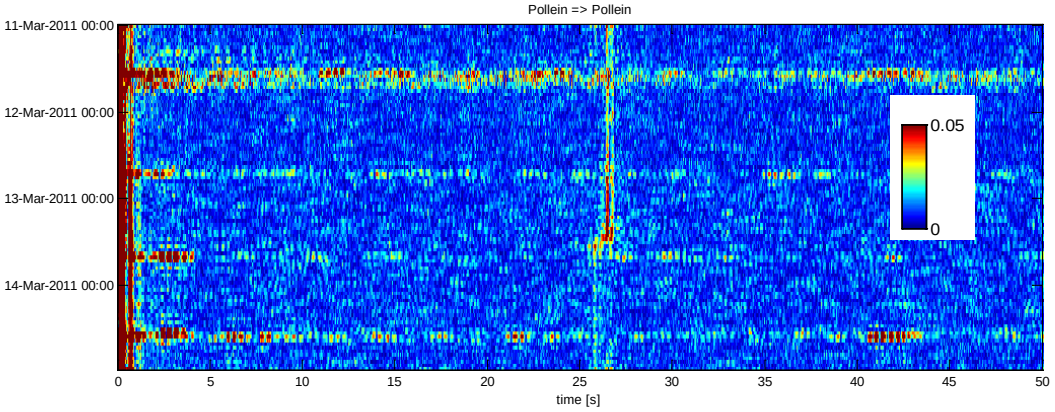

Figure 5.30. Autocorrelation of pressure signal at Pollein station in March 2011.

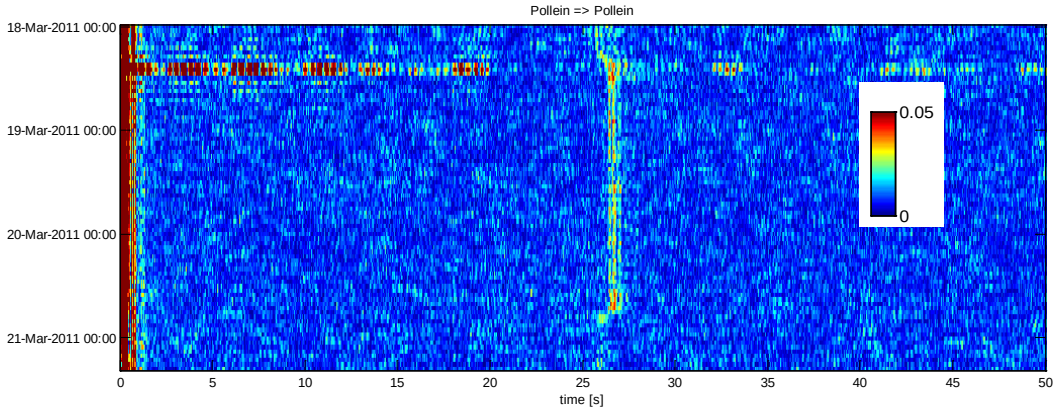

Figure 5.31. Autocorrelation of pressure signal at Pollein station in March 2011.

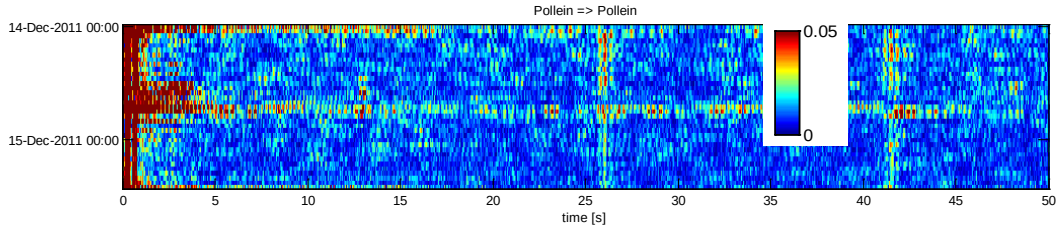

Figure 5.32. Autocorrelation of pressure signal at Pollein station in December 2011.

Figure 5.32 shows that a new echo appears in December 2011 at 41 seconds corresponding to a reflector 25 km far from Pollein.
In Figure 5.33 the Pollein autocorrelation during one shift of echo travel time is compared to the travel time shift from Pollein to V35 stations (computed by cross-correlation). Pollein-V35 travel-time shows that the front of the new faster oil passes through Pollein on 3rd March at about 12 a.m., which is the same time at which the echo travel time starts decreasing. This means that the reflector is downstream to Pollein.

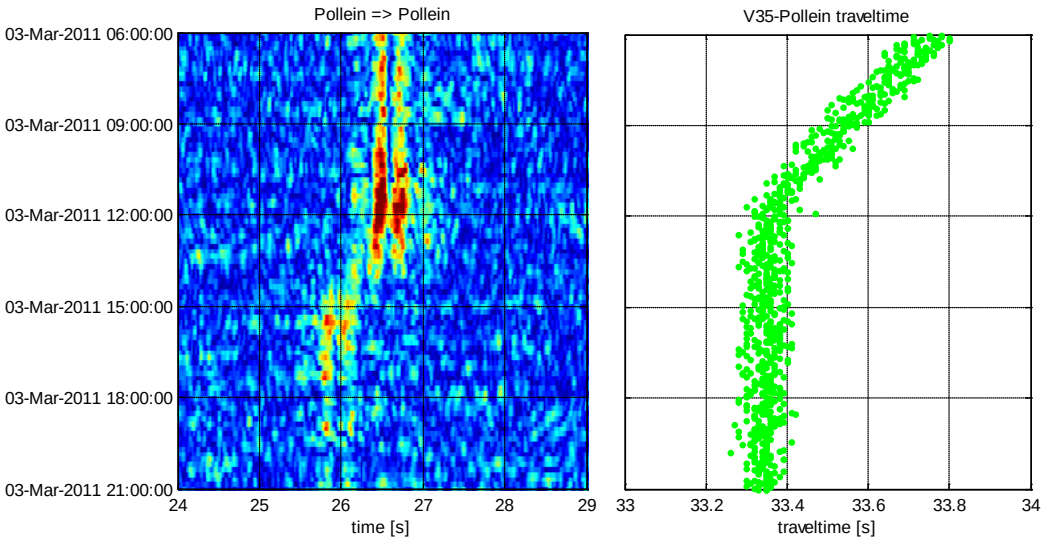

Figure 5.33. Autocorrelation of pressure signal at Pollein station, focus on travel time shift (left). Travel time from Pollein to V35 stations in same time interval (right).

In fact the following pumping station, Etroubles, is 15.85 km downstream from Pollein station, therefore the conclusion is that pump noise propagating from Pollein is "bouncing" at Etroubles (reflector at 27 s).
The other reflector has appeared only in December 2011, and there is not an oil change during its occurrence to discriminate the side. On the downstream side, at 41 s travel-time there is the Grand San Bernardo tunnel (8.53 km from Etroubles), on

the upstream side the reflector would be in the vicinity of valve VM41, which is more likely.
A further evidence of the fact that there is a reflector at 16 km from Pollein (identified as Etroubles pumping station) can be obtained from the raw signal measured at Pollein and superimposing a delayed and attenuated copy of itself.
Figure 5.34 shows the acoustic pressure (blue line) at Pollein station in 2 time windows during December 15th, when strong pump noise is recorded, together with the same signal delayed of 27 s and multiplied by a factor equal to -1/10 (red line). Signals are band-pass filtered [.1 1] Hz. The red line is meant to simulate the reflection 16 km away, and in fact it fits quite well some of the events in the blue line.

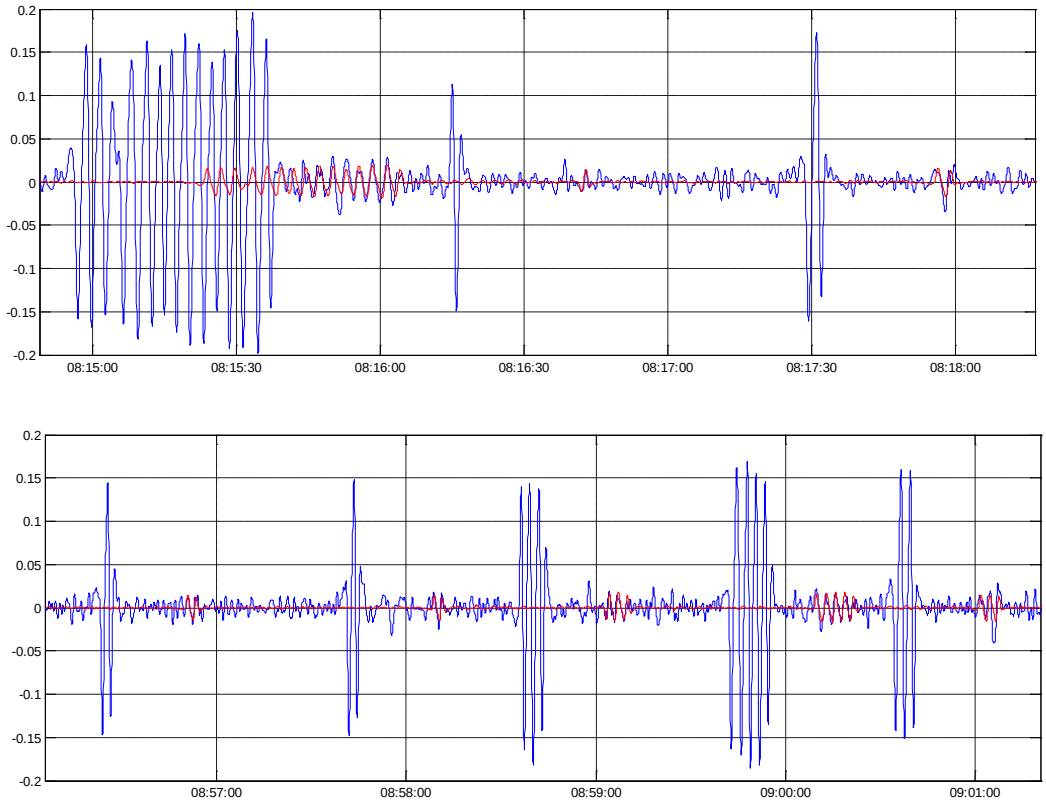

Figure 5.34. Pollein pressure signal(blue line) superposed to a scaled and delayed copy of itself (red line).

Discussion

The pump noise from Chivasso station is reflected by a discontinuity located where the pipe passes below the Milano-Torino highway, just downstream from V21 station: the discontinuity may be due to permanent (buckle) or dynamic (moving

vehicles) pipe deformation. Measurements at Pollein station detect an echo of its noise that come from Etroubles station.
Echo analysis (through autocorrelation of pump noise) can be run continuously in order to detect in real time important pipe anomalies, partial valve openings or localized occlusions.

5.4. Summary

On Gran San Bernardo oil pipeline e-vpms® technology supports a leak detection system which was installed and validated.
Moreover the available data measured and stored make possible (long term) advanced processing whose main results are:

- The acoustic attenuation curve measured up to 200 Hz fits with AXSYM-3L Model showing its strong dependence on the external medium properties.
- The long-term measured sound speed can be related to the type of oil transported, and to its API grade through literature models.
- The event of pump failure is easily detectable from measurement of acoustic pressure.
- The autocorrelation of pressure signals measured at pumping stations can help to spot even weak reflectors.

6. TMPC-TRANSMED pipeline

This chapter deals with the experimental campaign on TMPC-TRANSMED offshore natural gas pipeline, linking Cap Bon (Tunisia) and Mazara del Vallo (Sicily), the installation of the monitoring system and some interesting data processing.
The 1st section describes the installation of the monitoring system, the second shows some methods to monitor the movement of different pigs and the 3rd assesses the efficiency of the acoustic channel constituted by the whole pipeline during standard gas transportation.
Some of these results were published in [24], [33] and [34].

6.1. Pipeline and monitoring system description

TRANSMED lines L1S and L2S convey Algerian natural gas from the pumping station in Cap Bon (Tunisia) to the receiving station in Mazara del Vallo (Italy). Table 6.1 reports the parameters of the pipeline.

Line parameter	TRANSMED (20" lines)
External diameter	20" – 508 mm
Length	155 km
Maximum depth	610 m
Conveyed fluid	Natural Gas
Gas composition	Methane (88.8 mol %) Ethane (6.5 mol %)
Working pressure	90/110 bar – 150/180 bar
Gas direction	Cap Bon → Mazara del Vallo
Gas Temperature	56 → 10 °C

Table 6.1. TMPC pipeline: parameters of lines L1S and L2S.

Dionisio research project started just with the installation of a prototypal vibro-acoustic monitoring system on two lines (L1S and L2S) of the TMPC-TRANSMED pipeline, at Mazara del Vallo terminal. During the data acquisition period an offshore stretch of line L2S has been replaced (at 34 km from the coast), and pig operations have been carried out on both lines, in different operational conditions.
Moreover, after pipe maintenance, vibro-acoustic stations collected data in a three days period at both ends of pipe L1S (Cap-Bon and Mazara del Vallo).

Two phases of installation took place:
Phase 1: Installation at Mazara del Vallo, Lines L1S and L2S.
Phase 2: Installation at Cap Bon and at Mazara del Vallo, line L1S.

Figure 6.1 to Figure 6.5 show the installation details and the satellite maps of the pipeline and of the terminal stations.

Figure 6.1. TMPC TRANSMED pipelines

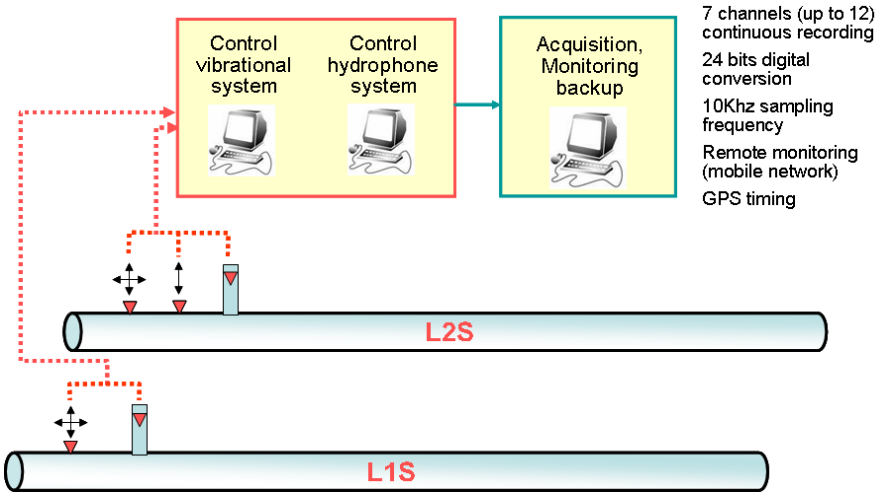

Figure 6.2. Phase 1: scheme of monitoring system

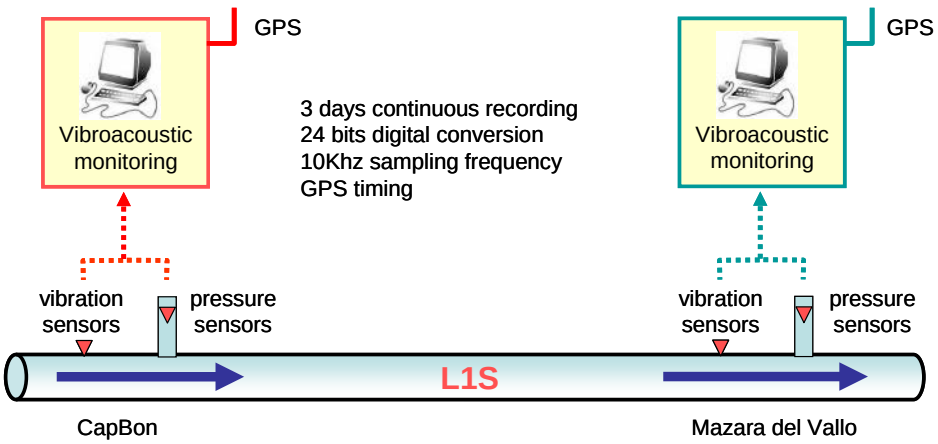

Figure 6.3. Phase 2: scheme of monitoring system

Figure 6.4. Satellite view: TMPC TRANSMED station of Mazara del Vallo (Italy) and sensor location.

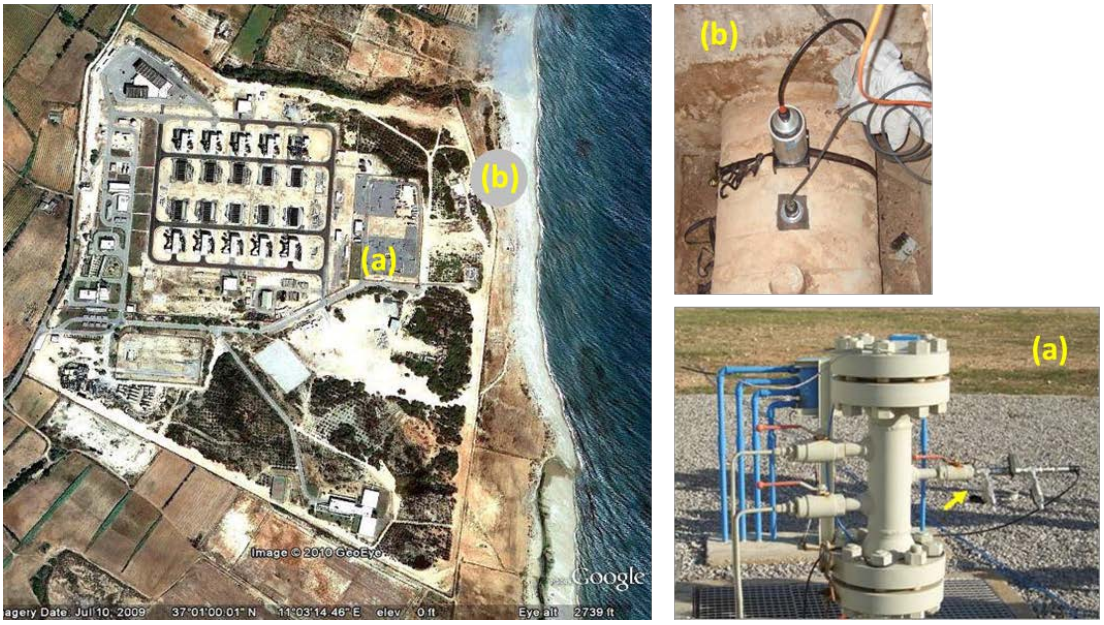

Figure 6.5. Satellite view: TMPC TRANSMED station of Cap Bon (Tunisia) and sensor location.

6.2. Monitoring of pigging operations

6.2.1. Low pressure pigging

Different pigs have been sent on both lines L1S and L2S. I analyze here the vibro-acoustic signal produced by a pig sent on 25th August 2009 from Cap Bon, and arrived at Mazara del Vallo on 26th August 2009, 17.20 GMT (Figure 6.6).

Figure 6.6. Line L2S, Mazara del Vallo, pig arrival on 26th August 2009.

The pipeline was filled with air at around 8 bar. Differential pressure at pig ends was around 2 bar. Figure 6.7 shows the pressure signal measured at Mazara terminal in a 3 hours period including the pig arrival: amplitude peaks (>1000 Pa) correspond to pig movement, detectable some hours before the arrival. Pig movement results discontinuous, with stop intervals of some minutes and sudden motion of tens of seconds.

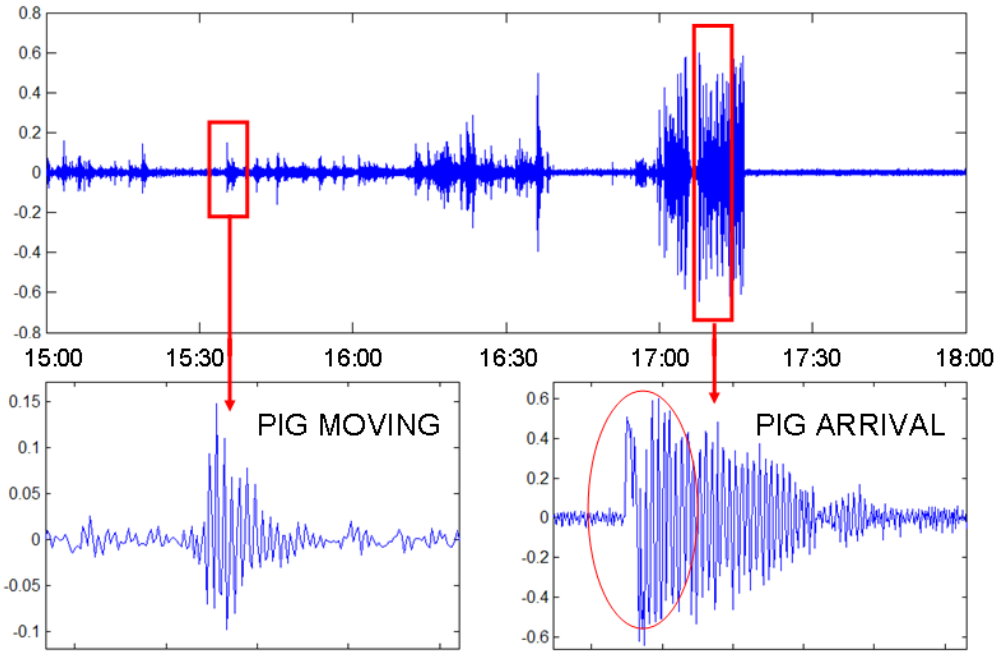

Figure 6.7. Line L2S, Mazara del Vallo. 5 Hz low pass pressure signal on 26th August 2009. GMT time. Vertical axis in Volts (10 kPa/Volt).

Figure 6.8 presents on the right the spectrogram of the shown pressure signal, the fundamental (lower) frequency (f_1) emphasized in the spectrogram together with the subsequent harmonics can be linked to the pig distance from pipe end. On the left of the figure there is the interpretation of the pig-induced stationary waves, whose frequency is an odd multiple of a quarter wavelength.
In fact the noise produced by the pig, when it moves, is continuously reflected by the pipe end and by the pig, so that stationary waves arise, the (fundamental) frequency of a stationary wave depends only on the speed of sound and the stretch length. Hence the distance of the pig from the pipe end can be easily computed from the frequency of the noise measured.

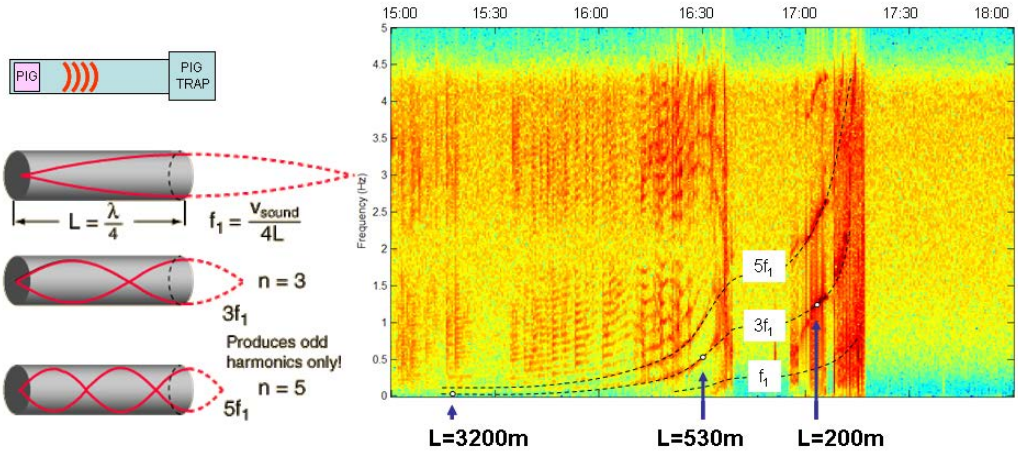

Figure 6.8. Line L2S, Mazara del Vallo. Pressure signal spectrogram on August 26 2009. GMT time. Explanation of pig-induced stationary waves. Time to distance conversion with an estimated sound velocity of 340 m/s.

6.2.2. High pressure pigging

During the vibro-acoustic monitoring period, other pig operations were performed in conditions of standard natural gas transportation. The pig travels at an almost constant velocity, and it produces pressure transients (sounds) when it crosses the pipe internal welds.

Figure 6.10 shows a five days log of the acoustic pressure (absolute values): the effect of two pigging operations is clearly visible (red boxes), on October 5th 2009 (smart pig, here called PIG1, Figure 6.9) and October 8th 2009 (magnetic pig, here called PIG2). The pipeline was in standard operation, at around 90-100 bar. The sound produced by the travelling pig increases almost exponentially as it approaches the receiving station, in agreement with the theory of sound propagation in cylindrical tubes: I have validated this behaviour with mathematical models in the following section.

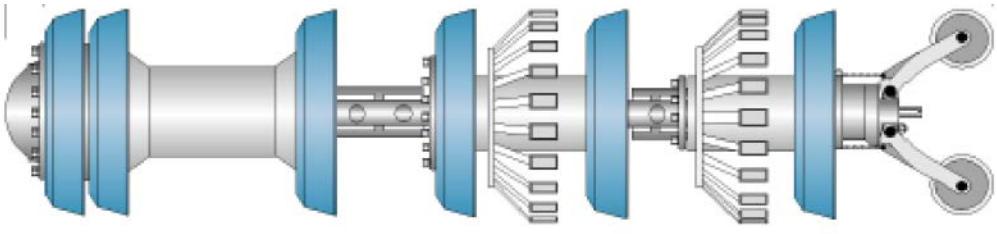

Figure 6.9. Inspection pig (www.RosenInspection.net).

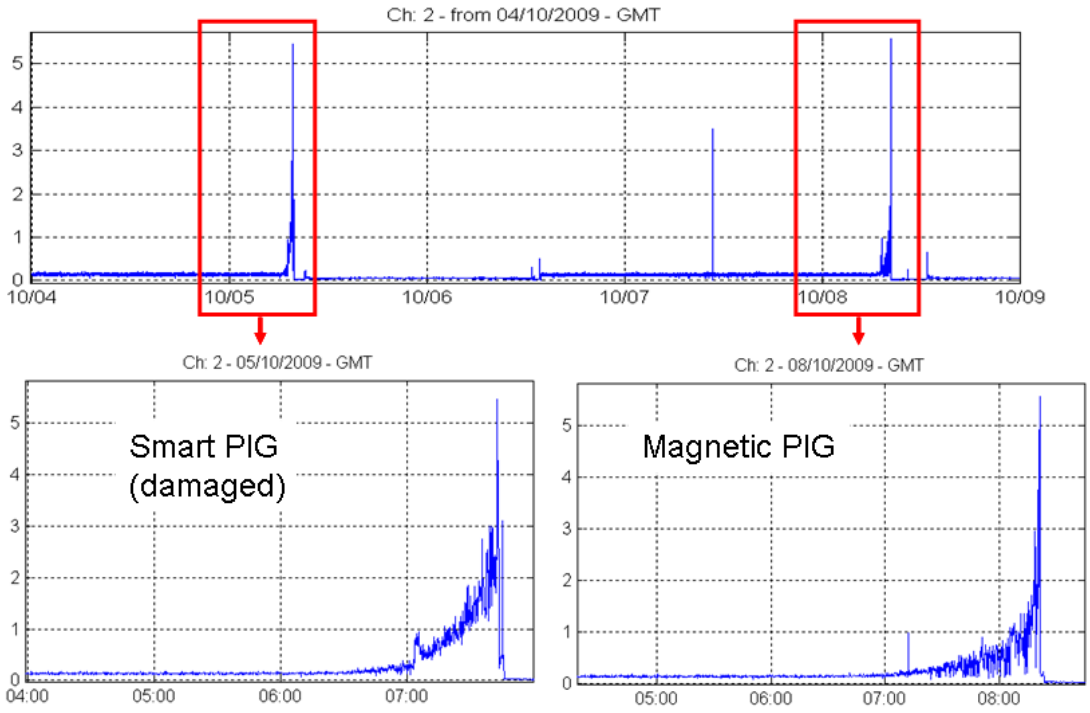

Figure 6.10. Acoustic pressure maxima on line L2S. Vertical axis in Volts (10kPa/Volt)

It is interesting to note an anomaly in the exponential increase, for PIG1 (Figure 6.11, top, red circle). In order to listen the anomalous signal, I have applied an upward shift of the signal bandwidth (originally below 100 Hz) to audible frequencies (around 1000 Hz) obtaining an audio rendering (for signal in red box in Figure 6.11, bottom) that reveals a probable damaging event, as one can hear noise of metallic objects scratching the inner pipe wall. Pig distance was around 8 km from the arrival monitoring station.

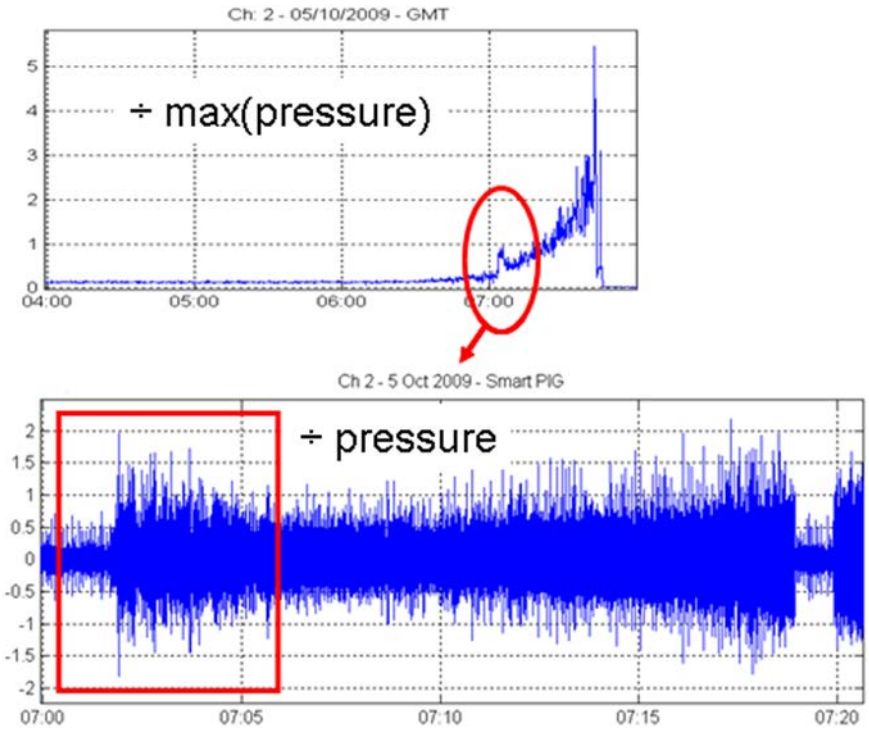

Figure 6.11. 5 Hz low pass pressure signal (absolute value on top, raw signal on bottom). Red circle indicates PIG1 damage. Vertical axis in Volts (10kPa/Volt).

Figure 6.12 in fact shows pictures of the extraction of PIG2, carrying fragments of the previously damaged PIG1.

Figure 6.12: PIG2 arrival, carrying fragments of previous damaged PIG1.

Figure 6.13 is the pressure signal when PIG2 is approaching Mazara del Vallo terminal station. In the zoomed windows it is possible to distinguish the wavelets generated by the pig while crossing the welds, about 12 m apart one from the other. I can count 12-14 events per minute, corresponding to a pig velocity of 9-10 km/h. The velocity is very stable, at least since these events become visible, some hours before the pig arrival.

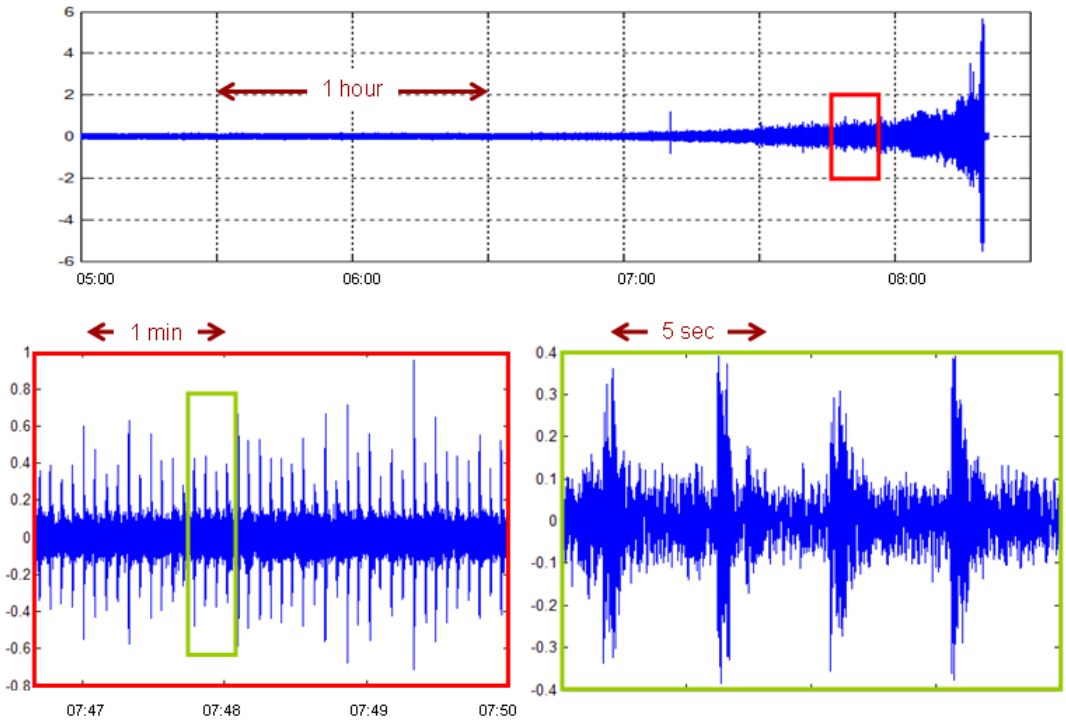

Figure 6.13. Pressure signal during PIG2 operation. Windows with increasing zoom factor. Vertical axis in Volts (10kPa/Volt).

In order to quantify the maximum detection distance, I performed a Short Time Average to Long Time Average processing (STA-LTA): Figure 6.14 is the result: every peak corresponds to the pig moving across a weld. By using a simple threshold criterion, I label the reliability of the events with a color scheme: green indicates correct detection, yellow is uncertain, red is missed. Figure 6.14 indicates that the pig becomes “visible” at more than 30 km from the arrival.

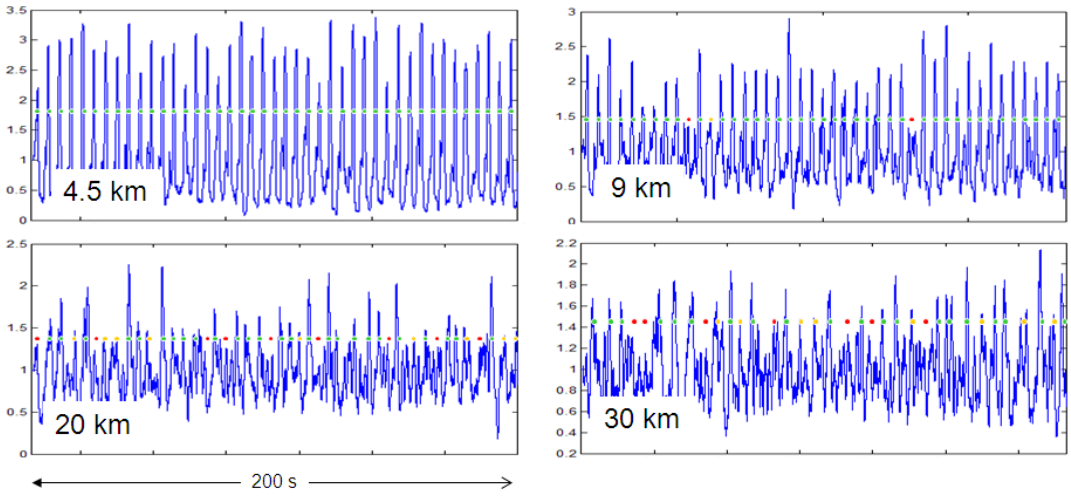

Figure 6.14. PIG2 detection, with STA-LTA processing on pressure signal (horizontal axis 200s).

Figure 6.15 shows the spectrogram of the pressure signal for PIG2 at around 5 km from the arrival station. Emissions at the welds have a bandwidth up to 500 Hz. Horizontal lines indicate resonance in pipe junctions (acoustical) and/or in the acquisition system (electrical).

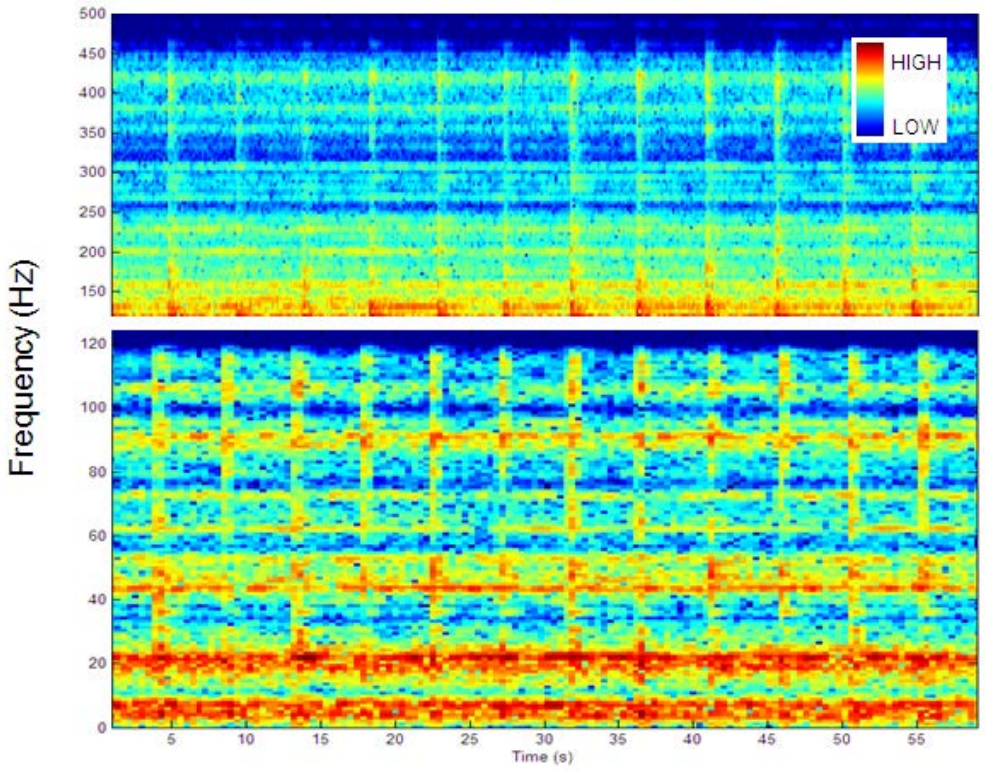

Figure 6.15. PIG2 pressure spectrogram. Pig distance around 5 km.

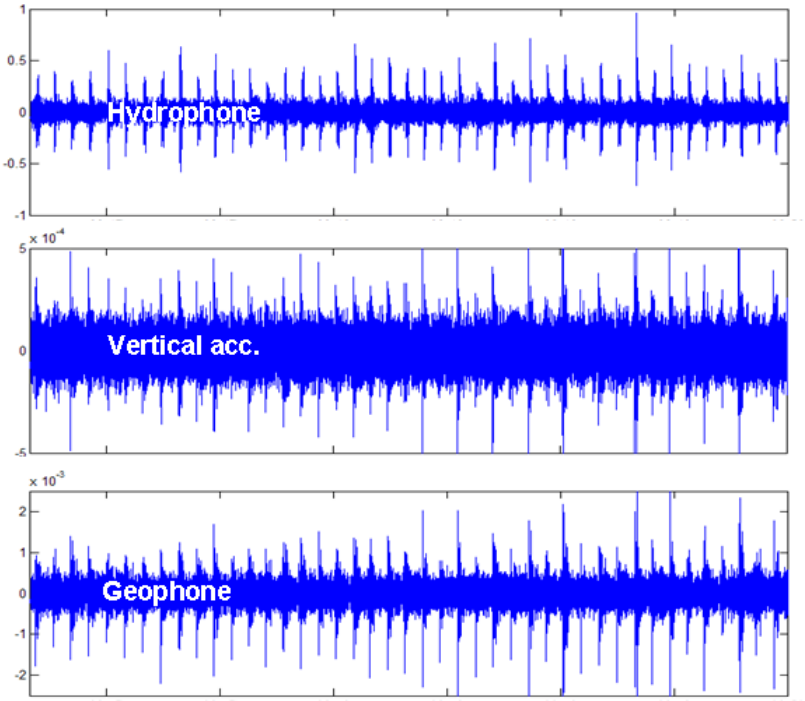

Figure 6.16. PIG2 pressure signal (top), acceleration on the pipe shell (center), velocity on the pipe shell (bottom). Pig distance around 5 km. Horizontal axis 200s. Vertical axis in Volts.

Figure 6.16 compares the signal recorded with different sensors (pressure in the fluid and vibrations of the pipe shell), for the pig at 5 km. Welds emissions are visible in all the sensors, but maximum detection distance is reduced to about 10 km for the pipe vibration monitoring (compared to 30 km for pressure).

6.3. Experimental computation of propagation parameters

By comparing the sound of the pig at different distances (Figure 6.17), one can also compute the acoustic wave propagation parameters within the gas in the pipeline, and compare them with the wide-tube mathematical formulation (Model 2, Eq. (2.5))

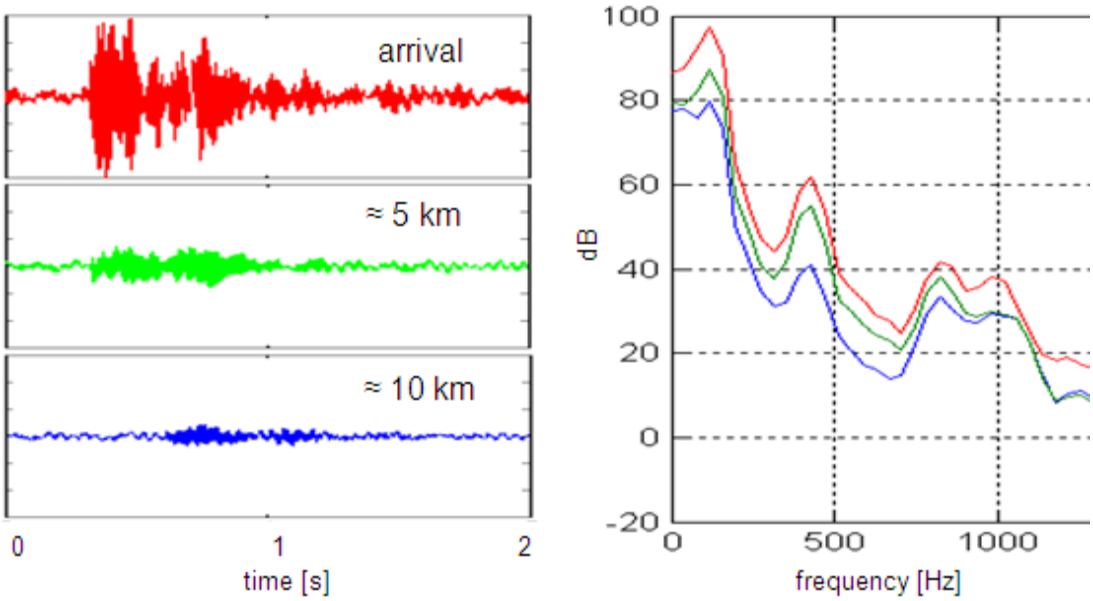

Figure 6.17: PIG2 signal at different distances (left) and power spectral density (right).

Figure 6.18 compares the theoretical (wide-tube approximation, Section 2.1.2) and the experimental attenuation factor. The analytical curve has been computed with the properties of the TransMed gas mixture (Table 6.1) at 100 bar. The fitting of the trend is good: discrepancies can be related to the noise generated by the gas flow, amplitude variations for the emissions at the welds (although the experimental result is averaged over 10 wavelets), acoustic or electric resonances.

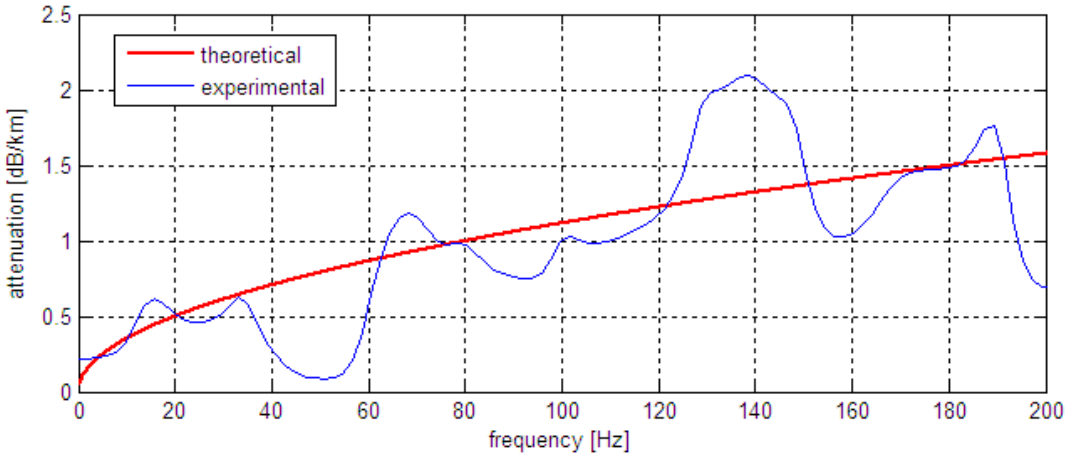

Figure 6.18. Experimental and theoretical attenuation coefficient

6.4. Acoustic channel analysis

After pigging operations, during standard gas transportation, I computed the correlation between the acoustic pressure signals recorded at two terminals of line L1S. A good correlation of the two signals would mean that acoustic waves can travel efficiently from one end to the other and therefore source signals produced within the line that are detected at one end, should be detected also at the other end. This occurrence allows localization.
The following assumptions apply:

- Both line terminals (Mazara and Cap Bon) produce pressure transients that travels towards the opposite end
- Line L1S constitutes an acoustic transmission channel between the terminal stations

In order to increase the signal/noise ratio which is rather low, I consider acoustic pressure maxima of the very low frequency component (lower attenuation).
Figure 6.19 is the block diagram of the cross-correlation processing. Spike-noise is mainly associated to manual hits on the hydrophone during the assembly of the system and is thus removed.

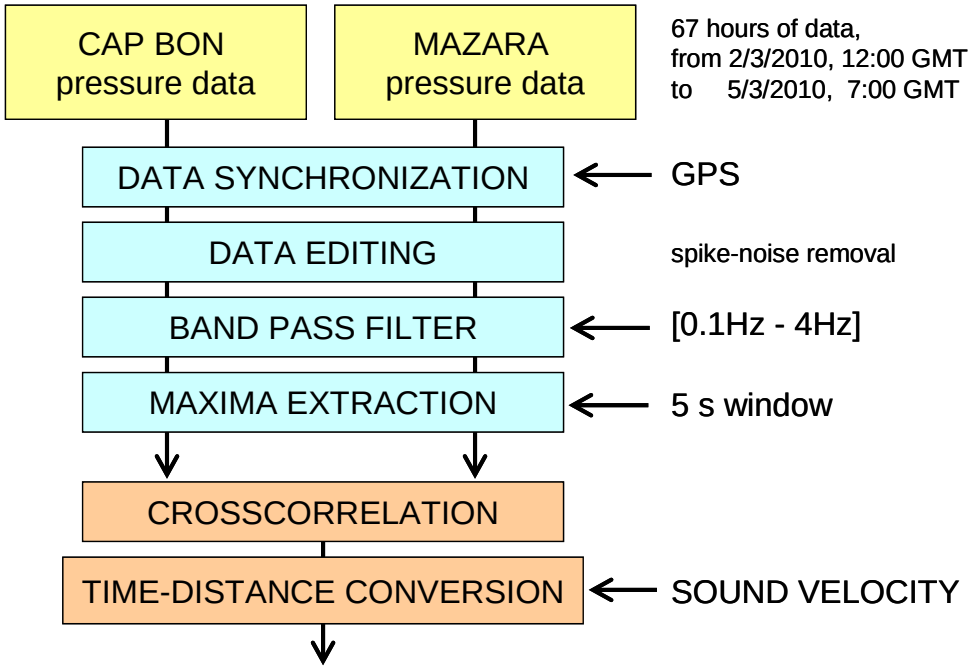

Figure 6.19. Block diagram of cross-correlation processing.

The result is shown in Figure 6.20. Time to distance conversion is obtained considering the gas flowing direction: flow velocity sums up to sound velocity for the downstream propagation, and it is subtracted from sound velocity for the

upstream propagation. According to personal communication from TMPC technicians, flow velocity is set to 10 m/s. Correlation peaks are visible at both pipe terminals even if they are not much stronger than background noise.

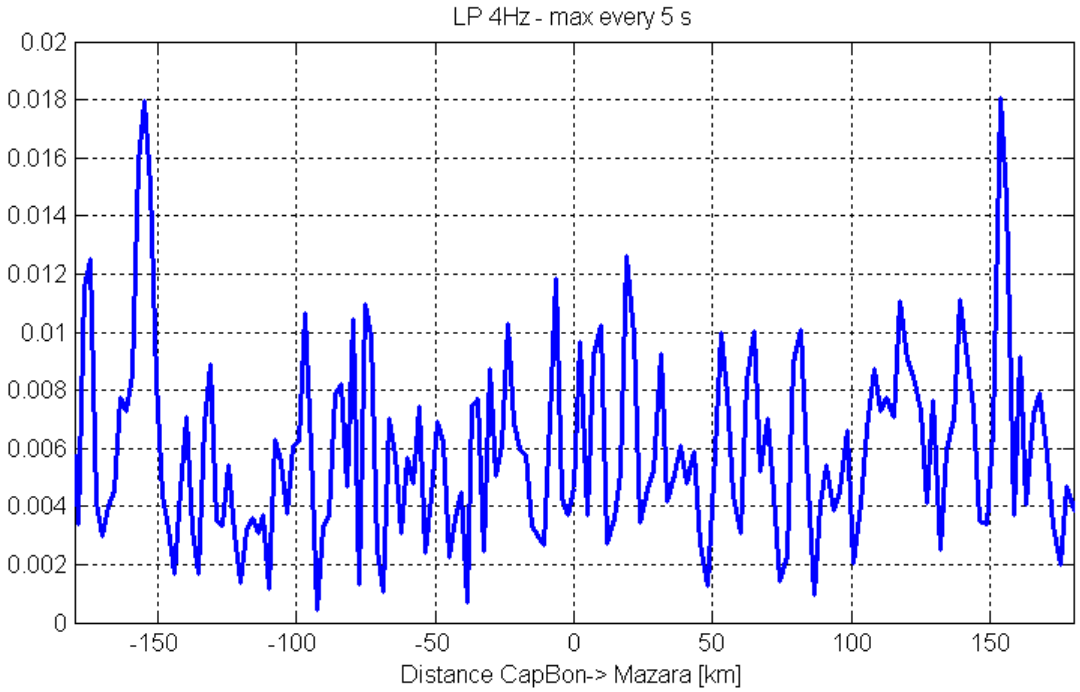

Figure 6.20. Cross-correlation of pressure signals measured at line terminals.

6.5. Summary

Main results from the TMPC-TRANSMED field campaign are the following:

- when the pig movement is discontinuous, sensors measure the noise of its sudden movement and the distance can be estimated from the resonant frequency;
- when the pig movement is continuous, sensors measure the noise produced when it passes through welds and its velocity can be estimated;
- pig movement and position can be detected from acoustic pressure measurements, up to tens of km;
- acoustic wave propagation within the gas can be approximated by Model 2 (Eq. (2.5), rigid wide-tube approximation);
- The total acoustic channel of the line (155 km) is weak but still works at low frequency (<5 Hz)

7. Passo Spluga pipeline

This chapter deals with the experimental campaign on Passo Spluga pipeline, in the stretch from Milano to Lecco (Italy), and some interesting results of the processing of measured data.
I participated to various field campaigns on this line, during which we installed a network of vibro-acoustic recording stations and produced controlled scenarios of leaks, impacts and third party interference.
The first section explains the installation of the monitoring system along the pipeline, the second deals with experimental measurements of propagation parameters and the last shows an application of reflectometry for detection of pipe anomalies.
Some of these results were published in [27] and [34].

7.1. Pipeline and monitoring system description

Passo Spluga pipeline is a 24" oil pipeline, at the time of field campaigns it is decommissioned and filled with air al low pressure (4-5 bar).
Table 7.1 shows the location of the main valves along the line stretch considered.

Valve	Location	km	Type	Latitudine	Longitude
V16	Cassina De Pecchi	71700	cameretta	45°31'06"N	9°22'13"E
V17	Bussero	73127	cameretta	45°31'46"N	9°21'60"E
VR17/a	Bussero	74001	pozzetto	45°32'13"N	9°21'53"E
VR17/b	Caponago	78914	pozzetto	45°34'17"N	9°23'08"E
VM18 - V19	Vimercate	82015	fabbricato	45°35'53"N	9°23'49"E
V20	Vimercate	82666	cameretta	45°36'10"N	9°24'03"E
VR20/a	Verderio Inferiore	88923	pozzetto	45°39'32"N	9°25'26"E
V21	Paderno	91435	cameretta	45°40'35"N	9°25'50"E
VM22-VM22a (V22)	Brivio	100605	fabbricato	45°44'37"N	9°25'57"E
V23	Capiate	104270	cameretta	45°46'26"N	9°25'31"E
VM25 - V26	Garlate	109496	fabbricato	45°48'48"N	9°23'41"E
VM27	Lecco Belledo	112575	fabbricato	45°50'22"N	9°24'17"E

Table 7.1. Main valves along the Passo Spluga pipeline, different colors distinguish stretches A and B.

For the campaigns two stretches of the pipeline were selected, both were stoppered at both ends and thus acoustically separated.

- Stretch A, total length 3080 m, submerged in the Garlate lake, from Garlate to Lecco-Belledo (Figure 7.1).
- Stretch B, total length 32580m, buried, from Cassina de' Pecchi to Capiate (Figure 7.2).

In stretch A, monitoring stations have been installed at the two extremes, that is at V26 and VM27; in stretch B, which is much longer, stations were installed at V17 – V19 – V20 – VM22a.

Station	Location	Distance [m]
VM25 -26	Garlate	0
VM27	Lecco Belledo	3080

24" pipeline, air pressure around 4 bar

VM26 GARLATE Station
1 accelerometer
3 hydrophones (for comparison and testing)

VM27 LECCO Station
1 accelerometer
3 hydrophones (for comparison and testing)

TESTS
- ambient noise
- hammer impact
- spilling (few sec)
- long time (>24h) electrovalve controlled spilling

Figure 7.1. Satellite map of stretch A (Garlate), and summary of tests and installation.

Station	Location	Distance [m] Total (partial)
V16	Cassina De Pecchi	0 (0)
V17	Bussero	1427 (1427)
VM18-19	Vimercate	10315 (8888)
V20	Vimercate	10966 (651)
VM22a	Brivio	28915 (17949)
V23	Capiate	32580 (3665)

24" pipeline, air pressure around 4 bar

V17	1 accelerometer 2 hydrophones
VM18-19 (variable)	3D accelerometers 2 hydrophones 1 static pressure 1 geophone 1 hammer
V20	1 accelerometer 2 hydrophones
VM22a	1 accelerometer 2 hydrophones 1 static pressure

Figure 7.2. Satellite map of stretch B, and summary of installation.

7.2. Experimental computation of propagation parameters

I here derive an experimental measure of the propagation parameters by comparing successive echoes of a pressure signal “bouncing” within the pipeline.
This happens for example during a spill test executed at V20: the source wavelet is sent in both directions and these two traveling waves are repeatedly reflected at the pipe ends until energy dies out. All this process determines the acoustic signal measured at V19 (Figure 7.3).

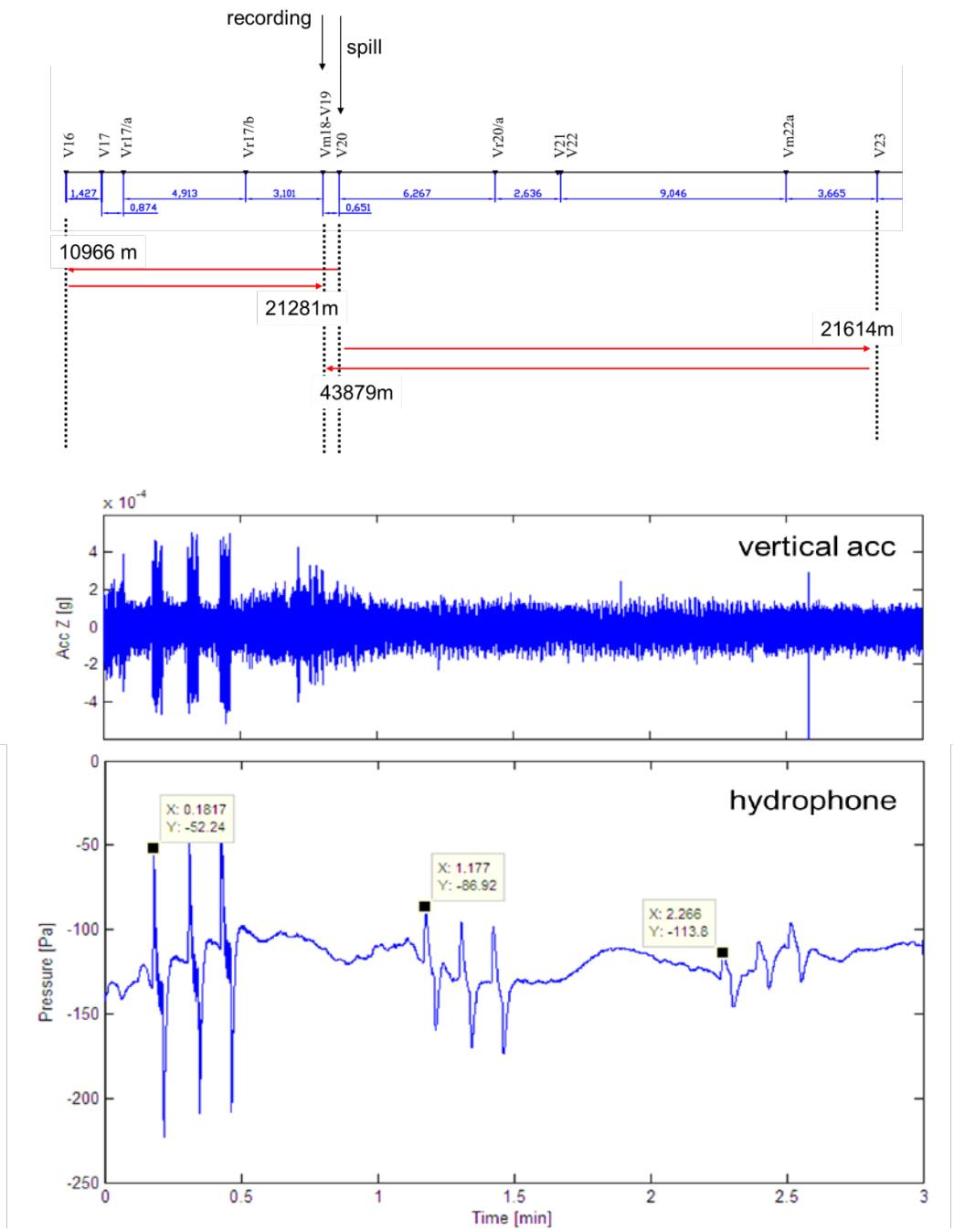

Figure 7.3. Example of data analysis. Spilling in V20, recording in V19: acoustic pressure within the fluid and acceleration on the pipe shell.

By comparing the amplitude of subsequent wavelets I compute the attenuation. Figure 7.4 and Figure 7.5 show the experimental and the analytical attenuation factor (in dB/km) for both the pipelines stretches A and B, the filling air is pressurized at the absolute pressures reported in the caption: the matching is very good.

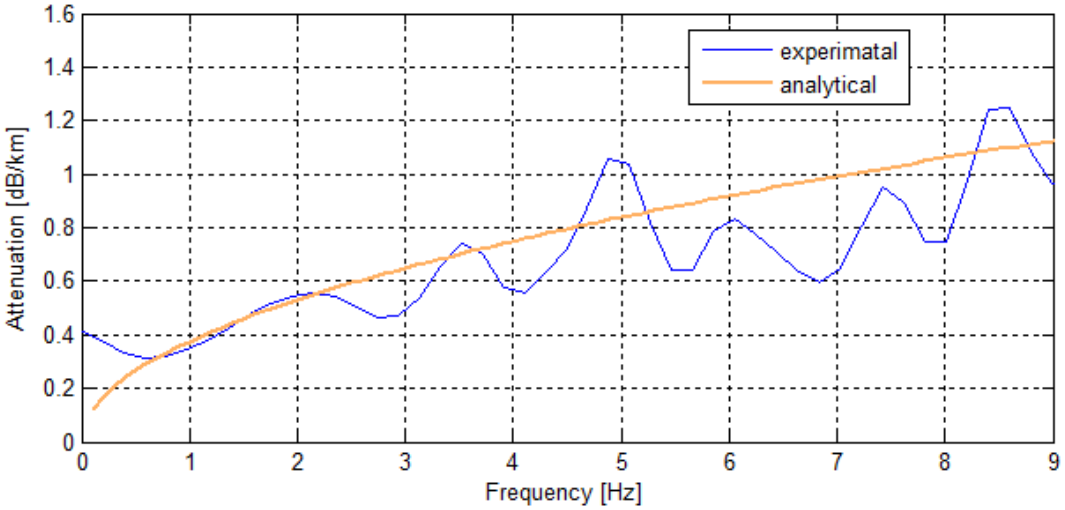

Figure 7.4. Attenuation of pressure waves in stretch A. Absolute pressure 5.2 bar.

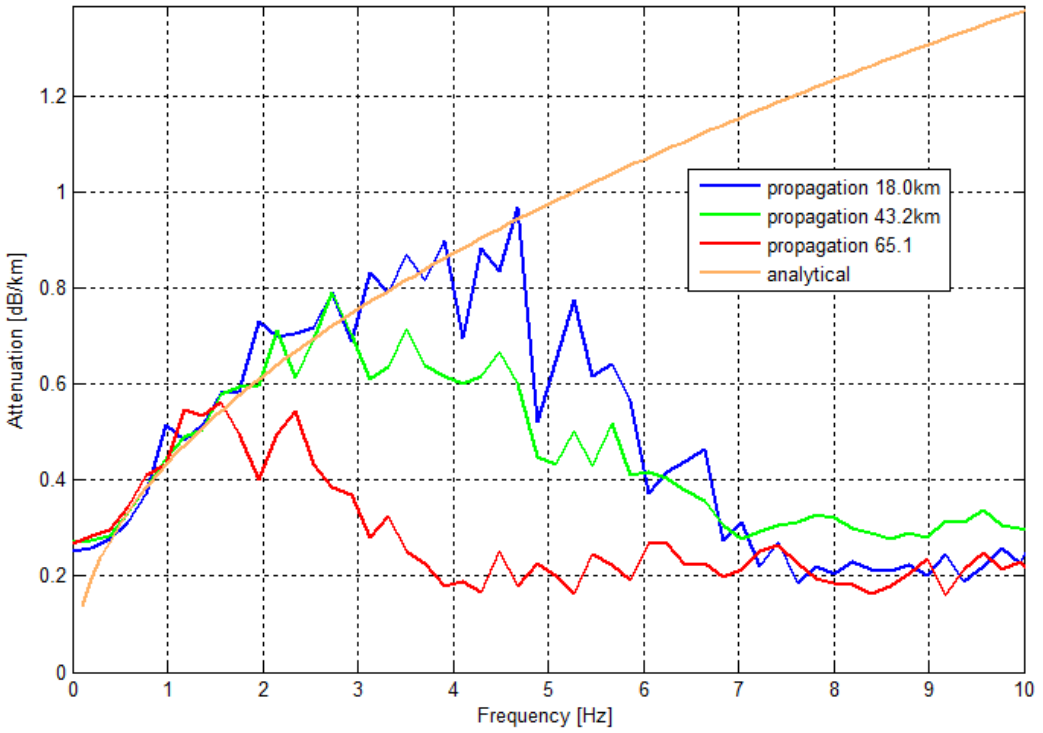

Figure 7.5. Attenuation of pressure waves in stretch B. Absolute pressure 3.8 bar.

Experimental lines are reliable up to 10 Hz (for the shortest propagation), as higher frequencies are continuously attenuated. Sound velocity, computed by picking the cross-correlation maximum between the pressure signals at two stations, is about 343 m/s, almost constant with frequency, consistent with air temperature of about 20 °C.

7.3. Acoustic reflectometry

I analyze here the pressure transients produced by a quick opening of a valve, in station V22. The pipeline is stoppered at V16 and V23. Pressure measurements are available at stations V19, V20, V22 (Figure 7.6).
Figure 7.7 shows the pressure signals at the three stations all together: the source wavelet is the first visible at about 5 s (red line), followed by the reflected echo by pipe occlusion at station V23, at around 25 s. The direct wavelet and its multiples are visible also in the other stations (blue and green lines).

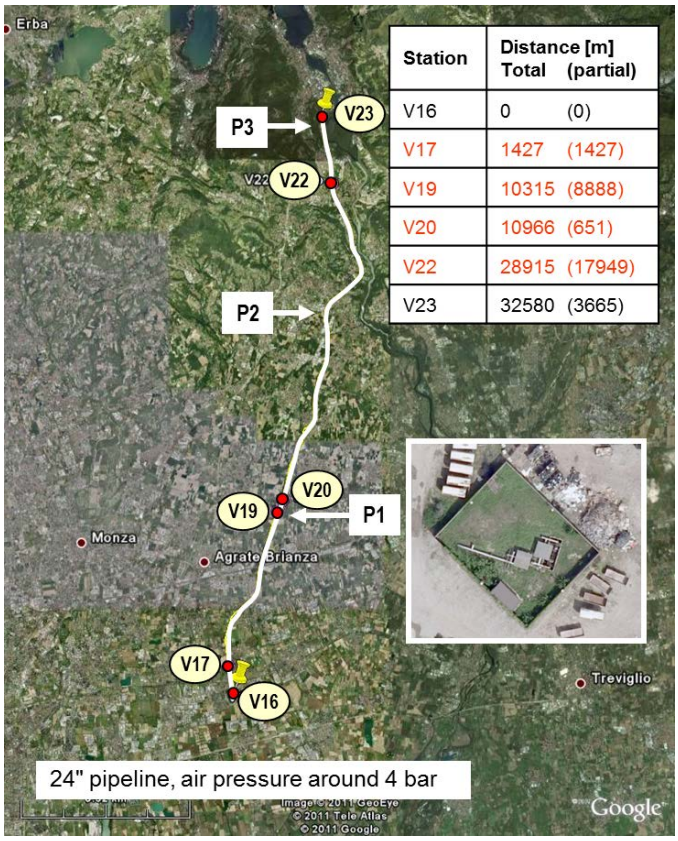

Station	Distance [m] Total	(partial)
V16	0	(0)
V17	1427	(1427)
V19	10315	(8888)
V20	10966	(651)
V22	28915	(17949)
V23	32580	(3665)

Figure 7.6. Satellite map of the pipeline route.

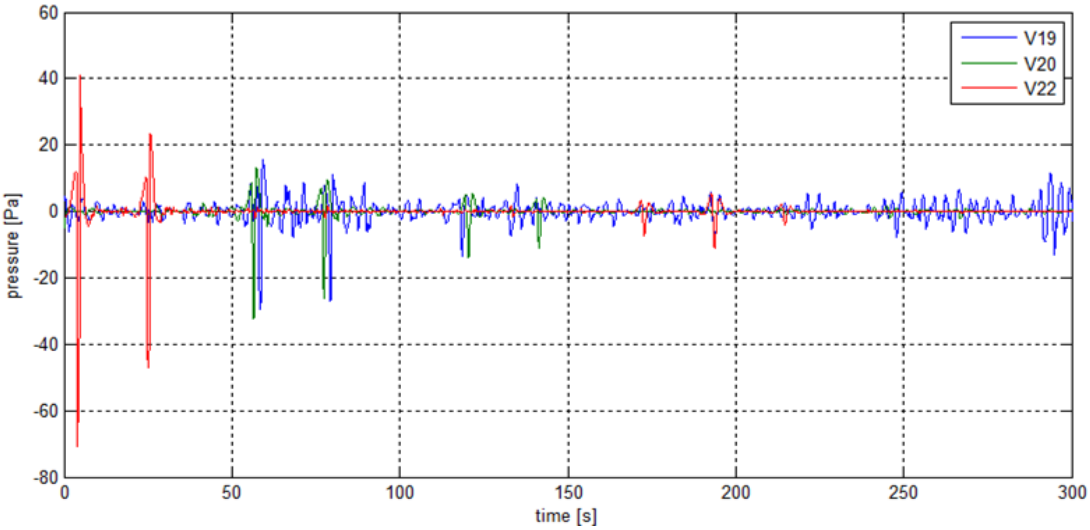

Figure 7.7. Pressure transients at V19, V20, V22, stations during an air spill test at V22.

I use then an acoustic simulator to compute the synthetic response of the pipe stretch, imposing a total reflection at both ends. The simulator is based on the Transmittivity Method, described in Appendix A, which derives from the Reflectivity Method (Müller [35]) and it takes into account the propagation phenomena occurring in pipes, such as attenuation and dispersion, and reflections/transmissions due to variations of internal cross-section. Attenuation and dispersion are functions of the filling fluid thermodynamic properties according to wide-tube approximation (Model 2, Section 2.1.2).

The best fit of data (Figure 7.8) is achieved with sound speed equal to 344.3 m/s, corresponding to air at 21 °C, and distance of the pipe end equal to 32510 m from V16, which therefore do not coincide with V23. Personal communication has confirmed that pipe occlusion is before station V23.

Figure 7.8 shows also some minor reflections (red arrows), that are not explained by the constant section-area pipeline.

They must be related to internal cross-section variations and/or pipe junctions. I have then run an acoustic reflectometry iterative inversion, looking for an equivalent mono-dimensional pipe model: such model takes as main parameter the section-area along the pipeline or, analogously, the equivalent radius *Req*. For such a pipe the nominal *Req* is set to 30.5 cm (12”).

The inverted model has the same total length and propagation velocity as the previous model (32510 m, 344.3 m/s, respectively), but it includes three main cross-section anomalies (say P1, P2 and P3) whose geometry and distance are displayed in Table 7.2.

The position of P1 anomaly coincides with station V19, where a by-pass pipe and a dead-end pipe branch are present (see aerial picture in Figure 7.6): in fact the inversion suggests a pipe section-area increase. P2 anomaly is positioned at a pipe

sectioning, where probably a buckle has been produced. P3 anomaly is located in a buried portion of the pipeline, very close to the final occlusion. Also here I suppose a buckle.
Figure 7.9 shows zooms of measured and computed signals at V22: most of minor echoes are correctly simulated (from 40 to 160 s), as well as their multiples, produced at pipe ends (from 220 to 360 s).

Anomalies	***Req* [cm]**	**Distance [m]**
P1	34.5	10315
P2	27.9	19815
P3	29.25	31305

Table 7.2. Minor anomalies in equivalent pipe model.

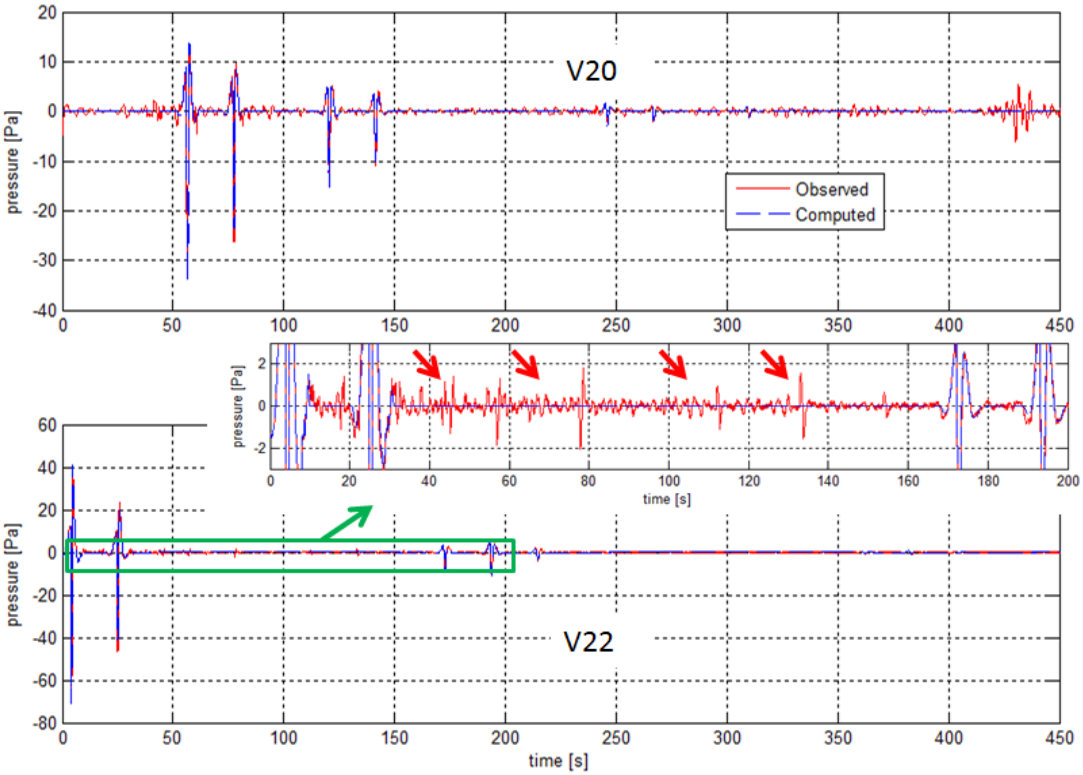

Figure 7.8. Measured and computed pressure signals at V20 (top) and at V22 (bottom)

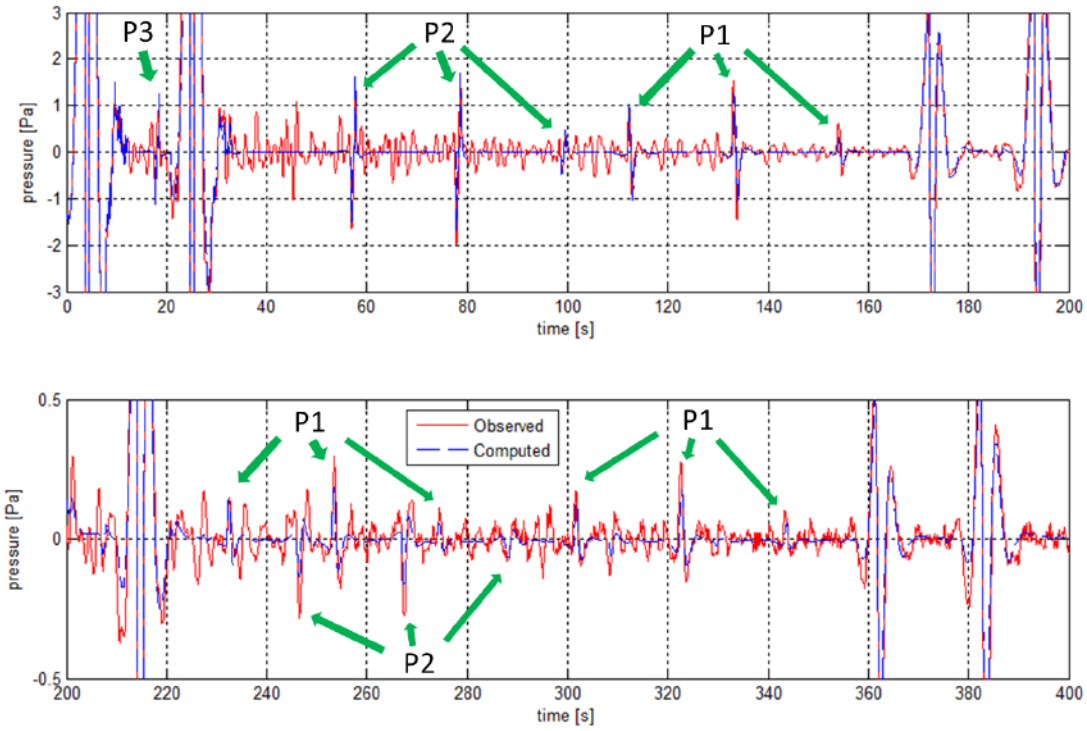

Figure 7.9. Measured and computed pressure signals at V22 station. Zoom on echoes from P1, P2, P3 (top). Zoom on multiples of P1, P2, P3 (bottom).

7.4. Summary

Passo Spluga pipeline is decommissioned and filled with air at few bars. Pressure noise within the pipeline is very low (around 1 Pa), while in operational pumping conditions it can reach several kPa and background pressure tens or hundreds of bars. The experimental propagation parameters were obtained and compared with theory, wide-tube analytic formula (Model 2 in Section 2.1.2) and the fitting was good.
Moreover an advanced procedure such as reflectometry was applied to the measurements which allows to localize and characterize some anomalous sections in the pipeline.

8. CSM pipeline

In this Section I analyze experimental measurements collected at Centro Sviluppo Materiali (CSM), a 500 m test pipe in Sardinia with the aim of estimating the propagation parameters of acoustic waves in high pressure gas-filled pipes.
Part of this material was published in [25] and [34].

8.1. Pipeline and monitoring system description

CSM is a full-scale test site endowed with a 535 m long steel pipeline (48" diameter) which simulates a portion of a natural gas pipeline, in order to study the mechanical properties of shell materials in extreme conditions (Demofonti et al. [36]). During one of these tests it was possible to install on the pipe a set of vibro-acoustic monitoring stations and to produce controlled pressure waves. In particular, besides other sensors, three hydrophones were placed at the two ends and approximately in the middle of the pipeline (Figure 8.1). The pipe was filled with Libyan-Algerian natural gas with increasing pressure up to 120 bar, and pressure transients were provided by gas spills and hammer strikes on the pipe.

Figure 8.1. CSM full-scale test pipeline map.

Station ID	Pipe coordinate [m]
Upstream pipe end	0
Station 1	1
Station 2	237
Station 3	534
Downstream pipe end	535

Table 8.1. Position of monitoring stations on CSM test pipe.

8.2. Experimental computation of propagation parameters

The speed of sound in the gas was estimated from the pressure signal measured by the hydrophones during the transients generated by spills. Spills were executed at different gas pressure conditions, so that a trend can be identified in the wave speed-pressure experimental function.
The wave speed estimate is performed in the frequency domain by considering a single receiver and looking for the resonance frequencies f_r. In fact, for a pipe closed at both ends of length L, internal diameter d, filled with a fluid with propagation velocity c, resonance occurs at frequencies

$$f_r = \frac{nc}{2(L + 0.8d)}$$

where n is a positive integer.
Therefore I can compute the sound-speed with this formula if I get the resonant frequency since the other variables are known.
As an example Figure 8.2 shows the acoustic pressure signals measured at two stations in a 8 minutes interval during spill test nr. 6, the pulse generated keeps on bouncing at the pipe ends for several minutes before dying out.

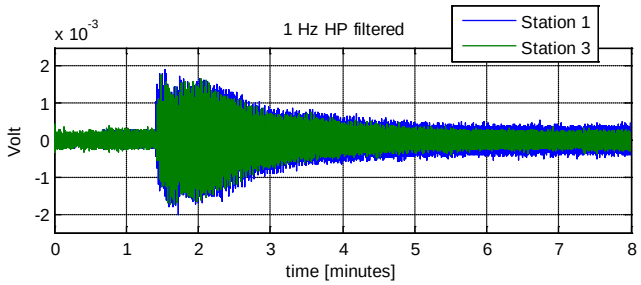

Figure 8.2 Acoustic pressure signal measured in the test pipe during spill.

The power of this long signal must be spread over the spectrum and the resonant frequencies must stand out.
In fact Figure 8.3 shows the spectrum of the raw pressure signal and arrows point to the lower 5 harmonics, from the first harmonic I compute the sound-speed.

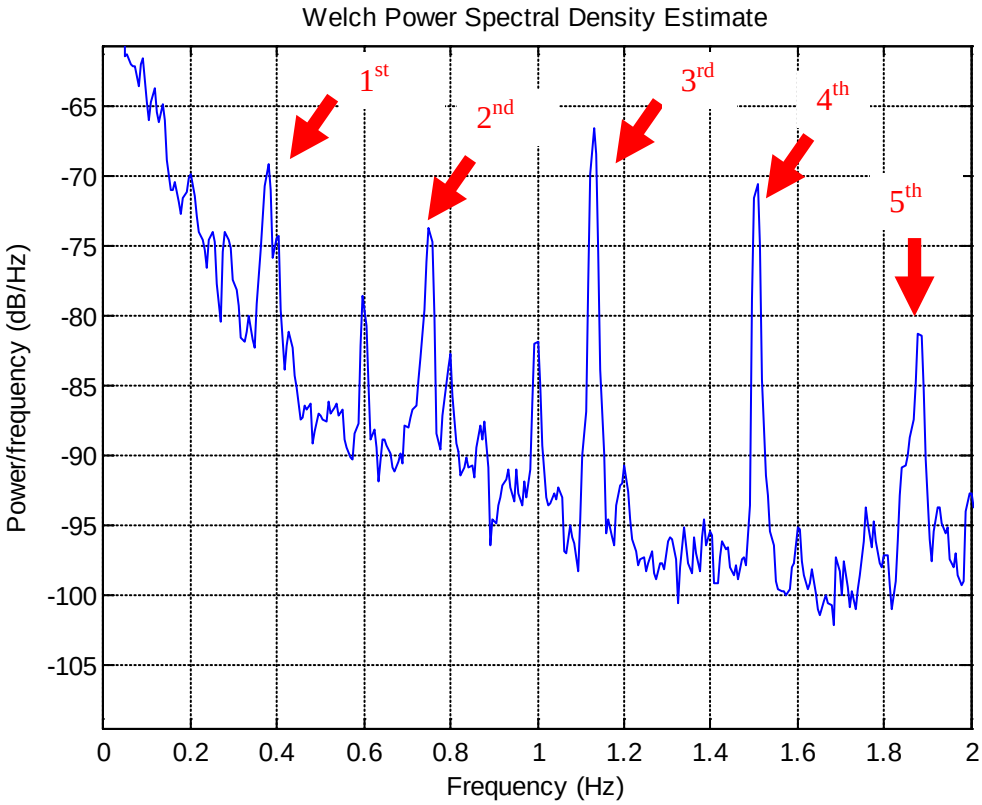

Figure 8.3. PSD of pressure signal during spill test nr. 6. Lower 5 harmonics.

The procedure is applied to 6 spill tests executed at increasing gas pressure, the fundamental resonant frequency is found and the sound-speed accordingly computed. Table 8.2 summarizes the results.

Spill test	Resonant frequency [Hz]	Wave speed [m/s]	Gas pressure [bar]
1	0.365	391	32
2	0.360	386	66
3	0.364	390	89
4	0.373	400	111
5	0.375	402	117
6	0.376	403	120

Table 8.2. Experimental speed of sound at CSM

It is interesting to note that the speed-pressure function is not monotonic, but it has a minimum at about 60 bar and this behavior should be confirmed by theoretical models of fluid properties.
I indeed compute the sound-speed of natural gas by means of a commercial software, Flowsolv™, which adopts report nr. 10 by AGA [37].

The natural gas composition reported in Table 8.3 is the result of a laboratory analysis of the actual gas filling CSM test pipe and I set it as input in the software.

Component	Vol (%)
N_2	2.2
C_4	88.7
CO_2	1.24
C_2	6.2
C_3	1.3
i-C_4	0.13
n-C_4	0.19
i-C_5	0.038
n-C_5	0.033
n-C_6	0.008

Table 8.3 CSM Natural gas composition

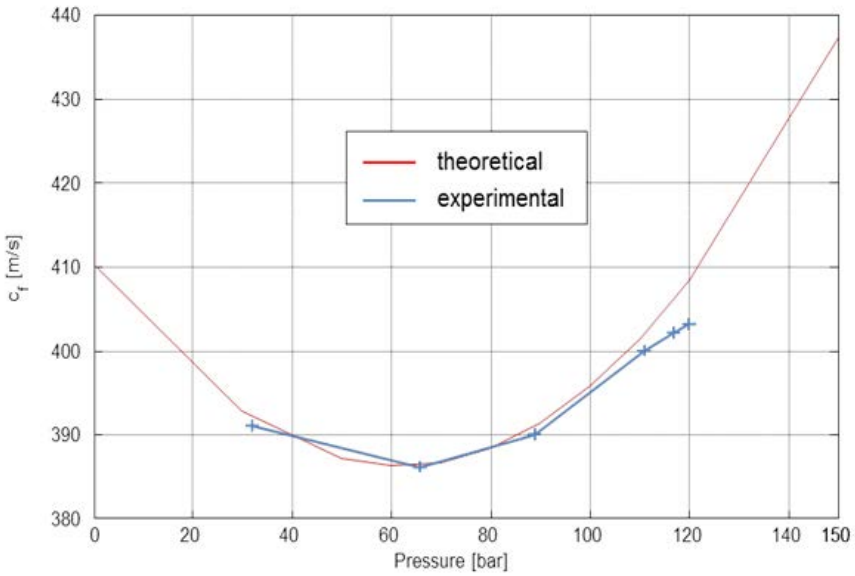

Figure 8.4. Experimental and theoretical (AGA10) speed of sound in natural gas.

The sound-speed computed in these way fits quite well the experimental data and presents the same minimum at about 60 bar (Figure 8.4).

9. Messina Channel pipelines

This chapter deals with the installation of the monitoring system on the offshore natural gas transportation pipelines crossing the Messina channel and the results of data processing. Details are in a eni confidential report (nr. 8 in Bibliography) , here I present results partly published in [34].
The objectives of the test campaign, still in progress, are the following:

- measure and analyze the environmental noise in service conditions;
- acquire vibro-acoustic data during controlled spill/leak test;
- design and test data processing routines for remote pig tracking;
- verify pipeline characterization with an equivalent acoustic transmission channel.

9.1. Pipeline and monitoring system description

e-vpms® stations have been installed on two offshore natural gas transportation pipelines crossing the Messina channel (Italy) and managed by SNAM RETE GAS. Both lines start at Messina station, line 1 (15.9 km) reaches Favazzina, line 4 (31.3 km) reaches Palmi.

Figure 9.1: offshore natural gas transportation Line 1 and Line 4.

9.2. Data analysis

Pressure noise is continuously generated by pumps, flow regulation equipment, local turbulence (“environmental” noise). In standard operation, absolute pressure is around 60-70 bar at the pumping station (Messina) and 50-60 bar at the receiving stations (Favazzina and Palmi). Low pass (0.5-10Hz) acoustic pressure noise is around 800-1800 Pa (8-18 mbar). Pressure noise has a comparable amplitude on all stations meaning that local turbulence and flow regulations are the main sources of

environmental noise. This noise is also comparable to measurements collected on the TRANSMED pipeline.
To assess the acoustic channel, I compute the cross-correlation between the acoustic pressure signals recorded at the two terminals of each line and do it repeatedly over about 1 day-long interval. The cross-correlation averaged over the same day is also given.
The pressure signals were previously low-pass filtered at 2 Hz.
Figure 9.2 is the result for line 1 (Messina - Favazzina): there is a correlation peak at around -40s, well standing out in the averaged cross-correlation (top) consistent with sound propagation from Messina to Favazzina at 386 m/s.
Figure 9.3 is the result for line 4 (Messina - Palmi): here a correlation peak is hardly detectable; in the probable case of propagation from Messina to Palmi at 386 m/s, the peak should lay at about -80 s. In the averaged cross-correlation a weak peak may be recognized at that time value but is really comparable with background noise.

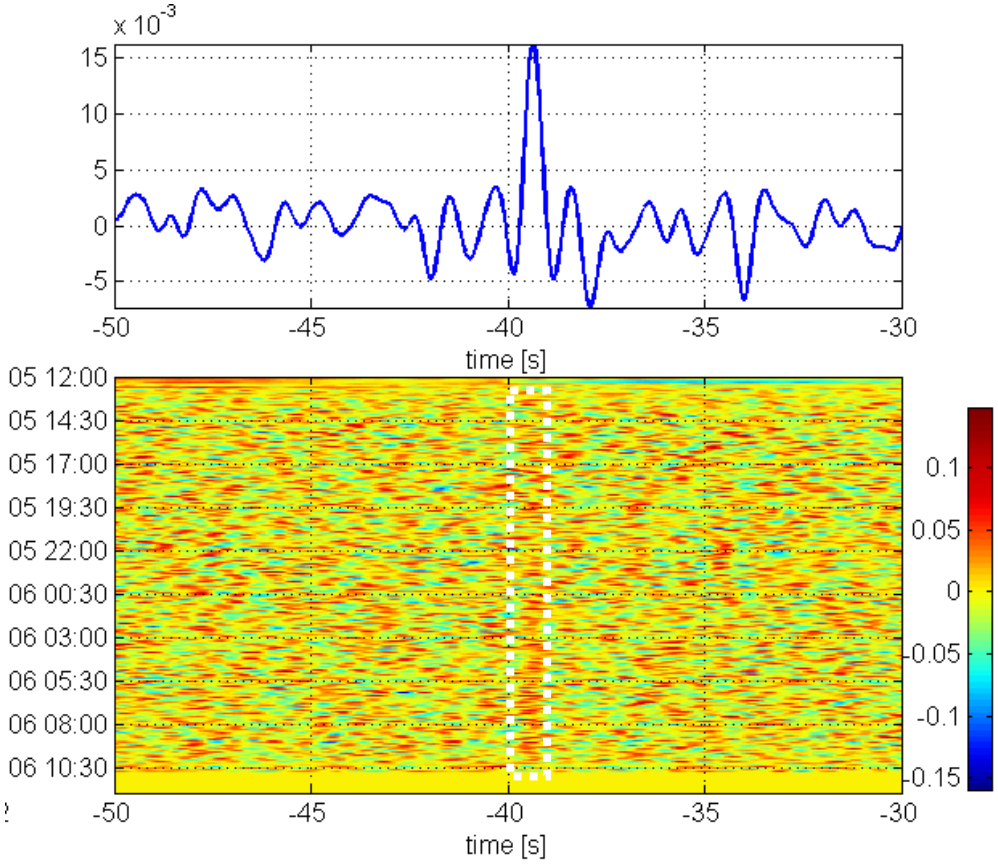

Figure 9.2. Normalized cross-correlation between pressure signals at Messina and Favazzina, from 12:00 Feb 5th 2013 (bottom). Average cross-correlation (top).

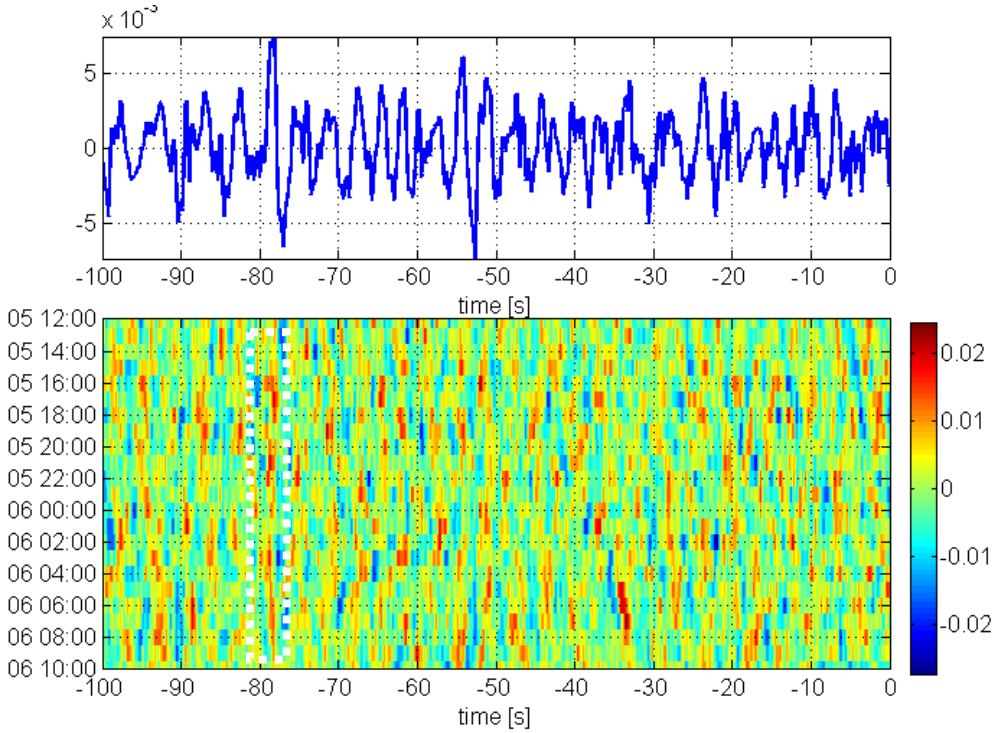

Figure 9.3. Normalized cross-correlation between pressure signals at Messina and Palmi, from 12:00 Feb 5th 2013 (bottom). Average cross-correlation (top)

.

Conclusion

During my PhD activity I contributed to the design of a registered vibroacoustic technology for remote real-time monitoring of pipelines (e-vpms®) promoted and supported by eni.
The system makes use of a network of discrete measurements along pipeline by means of sensors, such as hydrophones and accelerometers.
A considerable part of my contribution was the theoretical analysis of wave propagation in pipelines described in Part I and the processing of experimental data collected during several field campaigns: from one side the e-vpms® technology, in order to be designed and implemented, needed to rely on models of wave propagation in pipelines; from the other side such models could be tuned and validated thanks to the measurements made available by the monitoring system and proved to be valid even in operational conditions.
Furthermore theoretical links between propagation parameters and physical properties of the waveguide (mainly the conveyed fluid, but sometimes also the pipe and surrounding medium) help to interpret measurements and therefore to tune advanced processing for pipeline monitoring.
The monitoring system was installed and tested on different oil and gas pipelines.
On Gran San Bernardo oil pipeline the monitoring system evolved in an automatic leak detection system which was tuned and validated in-field by means of ad hoc tests.
A similar detection system was then installed also on Gaeta-Pomezia pipeline where it begins to benefit for the reason it was designed and produced, which is discovering actual oil theft.
An important goal reached is the validation of the AXSYM-3L model (Chapters 3 and 4) as regards the attenuation of acoustic waves in fluid-filled buried pipelines (even in service condition) at high frequency, where the effect of the surrounding medium elastic properties are important.
The e-vpms® system has been installed also on gas transportation pipelines both at rest and in service condition, with the following main results:

- In many gas pipelines the propagation parameters of sound were measured and found in agreement with the wide-tube approximation (Model 2 in Chapter 2).
- Travelling pigs generate vibro-acoustic transients when they begin to move and while they cross the pipeline internal welds. During travel, the pressure signal measured at one pipe end, can be effectively processed in order to track the position of the pig and its velocity from a distance of several tens of km.
- In an air-filled pipeline at rest, the wavelets produced by leaks were measured after travelling hundreds of km and I described a procedure to detect pipe anomalies that reflect those wavelets.

Furthermore, both in oil and gas filled pipes, as a side product of e-vpms® monitoring system, the available data measured and stored make possible advanced processing (even long-term) for pipeline monitoring such as identification of the standard pipeline operational conditions and detection of anomalous situations.
Finally the parameters of sound propagation and of fluid flow can be checked versus theoretically computable values, in order to derive additional information on fluid thermodynamic properties and/or pipeline infrastructure operational status.

Appendix A: Transmittivity Method

Here I describe the Transmittivity Method which is a way to compute the pressure wave-field in a one-dimensional waveguide, for instance a pipeline, triggered by a source excitation and shaped by its scattering on any number of interfaces constituted by cross-section variations.
The method can be used as the forward function in an inversion procedure to detect and localize possible anomalies in pipeline like it is performed in Section 7.3.
The following description is a synthesis of the treatment by Del Giudice [18], which is in turn the application to one-dimensional pipe stretches of the method described by Di Nicola-Sacchi [38]. Better known references are Kennett [39] and Müller [35].
The Transmittivity Method requires that the waveguide is modeled as a sequence of *n+1* stretches and *n* interfaces, the notation is displayed in Figure A.1.
Every stretch *i* is endowed with a length X_i and a cross-section radius b_i. If the section is not circular, b_i is the radius of the circle that has the same area as the stretch cross-section, named 'equivalent radius'.

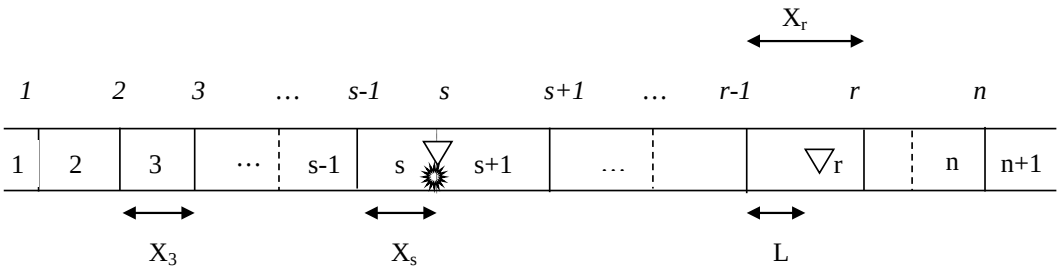

Figure A.1. Scheme of the one-dimensional waveguide used by the Transmittivity Method, the sun represents the source, triangles represent receivers.

The section where the source lies must be modeled as a fictitious additional interface called *s*.
The waveguide stretch containing the section where the solution wave-field is required is called *r* (after receiver) and the exact position is defined by the distance *L* from the left interface of stretch *r*.
Each interface can be associated with reflection *R* and transmission *T* coefficients for waves traveling in the two directions, *u* (after up) is used as superscript for waves travelling to the left, *d* (after down) for waves travelling to the right.
Therefore reflection and transmission coefficients associated to interface *i* can be expressed as function of the cross-section areas S of the two adjacent stretches.

$$R_i^d = \frac{S_i - S_{i+1}}{S_i + S_{i+1}} = \frac{b_i^2 - b_{i+1}^2}{b_i^2 + b_{i+1}^2}$$

$$T_i^d = \frac{2S_i}{S_i + S_{i+1}} = \frac{2b_i^2}{b_i^2 + b_{i+1}^2}$$
$$R_i^u = -R_i^d$$
$$T_i^u = 1 + R_i^u$$

Then Q_i is the factor that describes the propagation in stretch *i*, the direction doesn't matter, and can be defined through one of the propagation models of Chapters 2-3.
Now I introduce the reflectivity and transmittivity functions, $\mathbf{R}_i^d$, $\mathbf{T}_i^d$, $\mathbf{R}_i^u$, $\mathbf{T}_i^u$ which are someway similar to the corresponding coefficients but are ratios between signals instead of ratios between amplitudes and therefore they must contain all the (possibly infinite) sequence of reverberations that take place at the other side of the interface with respect to the incident wave considered.
This implies that these functions depend each on the subsequent except for those referred to extreme interfaces:

$$\mathbf{R}_n^d = R_n^d,\ \mathbf{T}_n^d = T_n^d$$
$$\mathbf{R}_1^u = R_1^u,\ \mathbf{T}_1^u = T_1^u$$

The other functions $\mathbf{R}_i^d$, $\mathbf{T}_i^d$ for *i=n* to *s+1* are iteratively computed with the following formulas starting from *i=n*.

$$\mathbf{T}_{i-1}^d = \left(1 - R_{i-1}^u Q_i \mathbf{R}_i^d Q_i\right)^{-1} T_{i-1}^d$$
$$\mathbf{R}_{i-1}^d = R_{i-1}^d + T_{i-1}^u Q_i \mathbf{R}_i^d Q_i \mathbf{T}_{i-1}^d$$

Similarly $\mathbf{R}_i^u$ and $\mathbf{T}_i^u$ for *i=1* to *s-1* are iteratively computed with the following formulas starting from *i=1*.

$$\mathbf{T}_{i+1}^u = \left(1 - R_{i+1}^d Q_{i+1} \mathbf{R}_i^u Q_{i+1}\right)^{-1} T_{i+1}^u$$
$$\mathbf{R}_{i+1}^u = R_{i+1}^u + T_{i+1}^d Q_{i+1} \mathbf{R}_i^u Q_{i+1} \mathbf{T}_{i+1}^u$$

Now let's consider the source and let's define the source signals sent to the right and to the left respectively S^d and S^u.
The aim is to compute the total signal P_s resulting from the propagation over the two packs of interfaces which would be measured at the source position *s*: this is the sum of the signal traveling to the left P_s^u and the signal traveling to the right P_{s+1}^d (the notation for signals P is explained in Figure A.2).

$$P_s = P_s^u + P_{s+1}^d$$

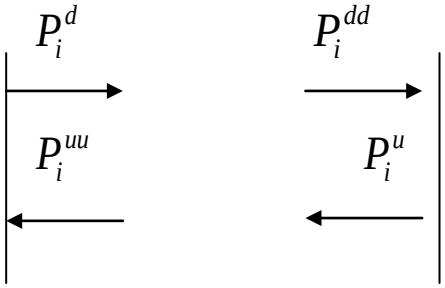

Figure A.2 Notation for signals P that depart from or impinge to an interface.

These addends are computed from the reflectivity functions referred to the two closest interfaces *s-1* and *s+1*, besides the propagators referred to stretches *s* and *s+1*.

$$P_s^u = (1 - \mathbf{R}_{s+1}^d Q_s Q_{s+1} \mathbf{R}_{s-1}^u Q_s Q_{s+1})^{-1} (Q_{s+1} \mathbf{R}_{s+1}^d Q_{s+1} S^d + S^u)$$
$$P_{s+1}^d = (1 - \mathbf{R}_{s-1}^u Q_s Q_{s+1} \mathbf{R}_{s+1}^d Q_s Q_{s+1})^{-1} (Q_s \mathbf{R}_{s-1}^u Q_s S^u + S^d)$$

Next, in order to have the signal measured in any position along the line, one needs to calculate the signals that depart from each interface in the two directions P_i^u and P_i^d.

Let's start from the signals just computed, P_s^u and P_{s+1}^d, and iteratively compute the signal at the close interface, through reflectivity and transmittivity functions.
For the interfaces on the left of the source:

$$P_i^d = \mathbf{R}_{i-1}^u Q_i P_i^u$$
$$P_{i-1}^u = \mathbf{T}_{i-1}^u Q_i P_i^u$$

from *i=s* to *2*.
And for the interfaces on the right:

$$P_i^u = \mathbf{R}_i^d Q_i P_i^d$$
$$P_{i+1}^d = \mathbf{T}_i^d Q_i P_i^d$$

from *i=s+1* to *n*.
Finally the signal A measured in any stretch *r* at any distance from left interface *L* is again the sum of a right-propagating signal A^d and a left-propagating one A^u.

$$A = A^d + A^u$$

Addends are computed from the signals departing from the two interfaces that limit stretch *r*, and by applying the proper propagators as function of *L*.

$$A^d = Q_r(L)P_r^d$$
$$A^u = Q_r(X_r - L)P_r^u$$

Bibliography

[1] Blackstock, D. T., Fundamentals of physical acoustics, *John Wiley & Sons, Inc.*, 2000.
[2] Stecki, J. S, & Davis, D. C., Fluid transmission lines: distributed parameter models, *Proceedings of the Institution of Mechanical Engineers*, 1986.
[3] Pinnington, R., & Briscoe, A., Externally applied sensor for axisymmetric waves in a fluid filled pipe, *Journal of Sound and Vibration 173*, 503–516. 1994.
[4] Muggleton, J., Brennan, M., & Pinnington, R., Wavenumber prediction of waves in buried pipes for water leak detection, *Journal of Sound and Vibration 249*, 934–954. 2002.
[5] Gazis, D. C., Three-Dimensional Investigation of the Propagation of Waves in Hollow Circular Cylinders, I. Analytical Foundation, and II. Numerical Results, *J. Acoust. Soc. Am.* 31, 568-577, 1959.
[6] Rama Rao, V. N. and Vandiver, J. K., Acoustics of fluid-filled boreholes with pipe: Guided propagation and radiation, *J. Acoust. Soc. Am.* 105, 3057–3066, 1999.
[7] Sinha, B. K., Plona, T. J., Kostek, S., & Chang, S., Axisymmetric wave propagation in fluid-loaded cylindrical shells. I. Theory, *J. Acoust. Soc. Am.* 92 (2), 1132–1143, 1992.
[8] Plona, T. J., Sinha, B. K., Kostek, S. & Chang, S. K., Axisymmetric wave propagation in fluid-loaded cylindrical shells. II. Theory versus experiment, *J. Acoust. Soc. Am.* 92, 1144-1155, 1992.
[9] Lowe, M. J. S., Matrix Techniques for ModelingUltrasonic Waves in Multilayered Media, *IEEE Transactions Ultrasonics ferroelecrics and frequency control*, 1995.
[10] Pavlakovic, B. N., Leaky guided ultrasonic waves in NDT, *Ph.D. dissertation*, Imperial College London, 1998.
[11] Aristégui, C., Lowe, M. J. S. and Cawley, P., Guided waves in fluid-filled pipes surrounded by different fluids, *Ultrasonics* 39, 367–375, 2001.
[12] Long, R. S., Cawley, P. and Lowe, M. J. S., Acoustic wave propagation in buried iron water pipes, *Proc. R. Soc. A* 459, 2749–2770, 2003.
[13] Vogt, T., Lowe, M., & Cawley, P., Measurement of the material properties of viscous liquids using ultrasonic guided waves, *IEEE Trans. Ultrason. Ferroelectrics Frequency Control*, 737-747, 2004.
[14] Ma, J., Lowe, M.J.S. and Simonetti., F., Measurement of the properties of fluids inside pipes using guided longitudinal waves, *Ultrasonics, Ferroelectrics and Frequency Control, IEEE Transactions on* 54(3) 647-658, 2007.
[15] Elvira-Segura, L., Acoustic wave dispersion in a cylindrical elastic tube filled with a viscous liquid, *Ultrasonics* 37, 537-547, 2000.
[16] Baik, K., Jiang, J., & Leigthon, T. G., Acoustic attenuation, phase and group velocities in liquid-filled pipes: Theory, experiment, and examples of water and mercury, *J. Acoust. Soc. Am.*, 128, 2610–2624. 2010.
[17] Liu, H., Pipeline engineering. *CRC Press LLC*, 2003.

[18] Del Giudice, S., Analysis of ducts by means of acoustic reflectometry (in Italian), *MSc thesis*, Politecnico di Milano, 2008.
[19] Morgan, G. W. & Kiely, J. P., Wave propagationin a viscous l iquid contained in a flexible tube, *J. Acoust. Soc. Am. 26*, 323, 1954.
[20] Junger M. C., The Physical Interpretation of the Expression for an Outgoing Wave in Cylindrical Coordinates, *JASA* 25(1), 1953.
[21] Abramowitz, M. and Stegun, I., Handbook of Mathematical Functions: With Formulars, Graphs, and Mathematical Tables, *United States Department of Commerce*, 1972.
[22] Nagy, P. B. and Nayfeh A. H., Viscosity induced attenuation of longitudinal guided waves in fluid-loaded rods, *J. Acoust. Soc. Am.* 100, 1501–1508, 1996.
[23] Kinsler, L. E., Frey, A. R., Coppens, A. B. and Sanders, J. V., Fundamentals of Acoustics, 4th ed. *Wiley*, New York, 2000.
[24] Bernasconi, G., Del Giudice, S., Giunta, G., Pipeline Acoustic Monitoring, *Pipeline Technology Conference*, Hannover, 2012.
[25] Bernasconi, G., Del Giudice, S., Giunta, G., Dionigi, F., Schiavon, R., Zanon, F., Advanced pipeline monitoring using Multipoint Acoustic Data, *11th OMC Conference and Exhibition*, Ravenna, 2013.
[26] Giunta, G., Dionigi, F., Bassan, A., Veneziani, M., Bernasconi, G., Del Giudice, S., Rovetta, D., Schiavon, R., Zanon, F., Third party interference and leak detection on buried pipelines for reliable transportation of fluids, *10th Offshore Mediterranean Conference*, Ravenna, 2011.
[27] Bernasconi, G., Del Giudice, S., Giunta, G., Dionigi, F., Advanced pipeline vibroacoustic monitoring, *Proceedings of the ASME 2013 Pressure Vessels & Piping Division Conference*, July 14-18, 2013, Paris, France, PVP2013-97281, 2013.
[28] Haykin, S., Adaptive Filter Theory, *Prentice Hall*, 2002.
[29] Batzle, M. and Wang, Z., Seismic Properties of Pore Fluids, *Geophysics* 57(11), 1396-1408, 1992.
[30] Labedi, R., Improved Correlations for Predicting the Viscosity of Light Crudes, *Journal of Petroleum Science and Engineering* 8(3), 221-234, 1992.
[31] Glaso, O., Generalized pressure–volume–temperature correlations, *Journal of Petroleum Technology*, 32(5), pp. 785-795, 1980.
[32] Beggs, H.D., Robinson, J.R., Estimating the Viscosity of Crude oil Systems, *Journal of Petroleum Technology*, 27(9), 1140–1149, 1975.
[33] Giunta, G., Dionigi, F., Bernasconi, G., Del Giudice, S., Rovetta, D., Vibroacoustic monitoring of pigging operations in subsea gas transportation pipelines, *ASNT Fall Conference*, Palm Springs, 2011.
[34] Giunta, G., Bernasconi, G., Del Giudice, S., Vibroacoustic Monitoring of Gas Filled Pipelines, *ASNT Fall Conference*, Las Vegas, 2013.
[35] Müller, G., The reflectivity method: a tutorial, *Journal of Geophysics* 58, 153-174, 1985.
[36] Demofonti G., Mannucci G., Lucci A., Spinelli C.M., Tap Project: External Damage Resistance of X100 Pipes for Long Distance High Pressure Pipelines, *PRCI/EPRG/APIA Conference*, Orlando, USA, 2005.
[37] AGA, AGA Report nr. 10. Speed of Sound in Natural Gas and

Other Related Hydrocarbon Gases, 2003.
[38] Di Nicola-Carena, E., Sacchi, M., Il metodo della trasmissività (in Italian), *Msc thesis*, Politecnico di Milano, 1994.
[39] Kennett, B., Reflections, rays and reverberations, *Bulletin of the Seismological Society of America* 64, 1685-1696, December 1974.

Submitted papers

1. Giunta, G., Bernasconi, G., Del Giudice, S., Advanced Pipeline Vibroacoustic Monitoring, *ASME Journal of Pressure Vessel Technology*.
2. Del Giudice, S., Bernasconi, G., Giunta, G., Attenuation of acoustic waves in a buried oil pipeline, *ASME Journal of Vibration and Acoustics*.

Eni internal documents

1. Bernasconi, G., Del Giudice, S., Rovetta, D., 2011, *Analisi teorica della fenomenologia acustico-vibratoria nelle tubazioni sommerse con fluido interagente sia all'interno che all'esterno e delle caratteristiche del fenomeno impattivo che può originare un danneggiamento della tubazione* (Fase C).
2. Bernasconi, G., Del Giudice, S., 2011, *Definizione delle specifiche tecniche e funzionali del sistema di misura/monitoraggio dei danneggiamenti delle linee sommerse* (Fase E).
3. Bernasconi, G., Del Giudice, S., Rovetta, D., 2011, *Vibroacoustic monitoring of interference and spilling actions on the Chivasso-Aosta oil pipeline. Data analysis*. (Fase F-bis, REP3)
4. Bernasconi, G., Del Giudice, S., 2011, *Vibroacoustic monitoring of interference and spilling actions on the Chivasso-Aosta oil pipeline. Data analysis*. (Fase F-bis, REP3-addendum)
5. Bernasconi, G., Del Giudice, S., 2012, *Vibroacoustic monitoring of spilling actions on the Chivasso-Aosta oil pipeline* (Fase F-bis, REP4).
6. Bernasconi, G., Del Giudice, S., 2012, *Raccolta di dati sperimentali su ex Oleodotto Passo Spluga, tratto Cassina De Pecchi – Lecco Belledo* (Fase F, REP1, REP2, REP3).
7. Panzetti, L., Signori, M., Di Fronzo, F., Bernasconi, G., Del Giudice, S., 2013, *e-vpms® installation on Kwale-Akri pipeline.*
8. ARESYS, *2013, Messina channel e-vpms installation and data analysis.*

Patents and Trademarks

- M. G. Dalmazzone, G. De Lorenzo Gianpietro, G. Giunta, "System and method for the continuous detection of impacts on pipelines for the transportation of fluids, particularly suitable for underwater pipelines", ENI S.p.A, Patent Application PCT/IB2010/002330; WO-2011/039589, US2012/0243376, EP-2483656A1, EA-201290159

- Giunta, G. Bernasconi, “Method and system for the remote detection of the position of a pig device inside a pressurized pipeline”, ENI S.p.A, Patent Application PCT/EP2013/076413
- Giunta, G. Bernasconi, “Method and system for continuous remote monitoring of the integrity of pressurized pipelines and properties of the fluids transported” ENI S.p.A, Patent Application PCT/EP2013/077116
- “e-vpms, eni vibroacoustic pipeline monitoring”, Trademark by ENI S.p.A., Europe, US&Canada n°85815700